THE IMPACT OF SURFACE FORCINGS ON THE ATLANTIC MULTIDECADAL VARIABILITY

by

Liang Yu
A Dissertation
Submitted to the
Graduate Faculty
of
George Mason University
In Partial fulfillment of
The Requirements for the Degree
of
Doctor of Philosophy
Climate Dynamics

Committee:

____________________ Dr. Bohua Huang, Dissertation Director

____________________ Dr. Barry A. Klinger, Committee Member

____________________ Dr. Jagadish Shukla, Committee Member

____________________ Dr. Timothy DelSole, Committee Member

____________________ Dr. James L. Kinter III, Department Chair

____________________ Dr. Donna M. Fox, Associate Dean, Office of Student Affairs & Special Programs, College of Science

____________________ Dr. Peggy Agouris, Dean College of Science

Date: ____________________ Spring Semester 2019
George Mason University
Fairfax, VA

The Impact of Surface Forcings on the Atlantic Multidecadal Variability

A dissertation submitted in partial fulfillment of the requirements for the degree of Doctor of Philosophy at George Mason University

By

Liang Yu
Master of Science
Institute of Oceanology, Chinese Academy of Sciences, 2013
Bachelor of Science
Nanjing University, 2010

Director: Dr. Bohua Huang, Professor
Department of Atmospheric, Oceanic, and Earth Sciences

Spring Semester 2019
George Mason University
Fairfax, VA

Dedication

For my grandmother

Acknowledgments

First, I owe my deepest gratitude to my advisor, Dr. Bohua Huang, for his tremendous help and support in my PhD study at Mason. I had a hard time during the last few years and made almost no progress for a long time. He never pushed or blamed me, but encouraged me, which helped me feel less stressed. He always respected my thoughts and never asked me to follow his idea, even when his idea was better. He helped me revise the thesis word by word, and go through the pre-defense and defense presentations slide by slide. This thesis and my defense would not have been possible without his help. I own my deepest appreciation to him for his patience, kindness and wisdom. I have also benefited and learned a lot from his peacefulness. Working with him has been the most valuable experience during my study, from which I learn, practice and try to excel.

I would like to thank the rest of my thesis committee: Dr. Barry Klinger, Dr. Timothy DelSole and Dr. Jagadish Shukla, for their insightful comments and encouragement. I still remember six years ago when I first came to Mason and met Barry. I called him Prof. Klinger and he said ”Call me Barry”. As a graduate coordinator and a member on my committee, Barry helped me throughout the past six years. He was always willing to spare time for me whenever I had a question. The discussions with him provided very useful and supportive information for my research. I am very grateful to him. Tim's insight was very impressive and I learned a lot from that. I would also like to thank Tim for going through all the slides after pre-defense. Shukla always encouraged me to talk to him for any questions I had, even if he was super busy. I am also grateful to Shukla for his suggestions of an early version of the pre-defense slides.

I would like to acknowledge the professors for their instructions in classes.

I am grateful to Jennifer Adams and Thomas Wakefield for their technical support.

I would also like to thank other staff for their support. When I was in my fifth year and worried whether I could graduate, Stephanie ONeill encouraged me ”Take your time. Everyone has their own path”. Her enthusiasm could always cheer me up.

I am very grateful to Ralph Getzandanner for proofreading and suggesting edits for this thesis.

In addition, I would like to thank all of the fellow students for their friendliness and help.

I would like to thank my roommates and landlord for their continuous help and support.

Last but not least, I would like to thank my parents for supporting my study overseas and their help in my life.

Table of Contents

List of Tables

List of Figures

LIST OF ABBREVIATIONS AND/OR SYMBOLS

AGCM .... Atmospheric general circulation model
AMO .... Atlantic Multi-decadal Oscillation
AMOC .... Atlantic meridional overturning circulation
AMV .... Atlantic multi-decadal variability
BSF .... Barotropic stream function
C_{adv} .... HC advection term
C_{diff_H} .... Horizontal diffusion in heat budget equation
C_{diff_V} .... Vertical diffusion in heat budget equation
C_{ek} .... HC advection term generated by Ekman current
C_{geo} .... HC advection term generated by geostrophic current
CCSM3 .... Community climate system model, version 3
CESM .... Community earth system model
CGCM .... Coupled general circulation model
CICE4 .... Community Ice CodE, version 4
CNTL .... Experiment CNTL, monthly SHF, SFWF& SMF
CPLD .... Experiment CPLD, A fully coupled CESM pre-industrial run
CORE2 .... Coordinated ocean-ice reference experiments, phase 2
DG00 .... Delworth and Greatbatch 2000
DN10 .... Air density at 10 meters
EOF .... Empirical orthogonal functions
EV .... Evaporation
GS .... Gulf Stream
HC .... Heat content
HCgulf .... Heat content averaged over GS extension region
HCnorth .... Heat content averaged over northeast Atlantic Ocean
HEAT .... Experiment HEAT, monthly SHF & SFWF, climatological SMF
H_t .... Heat content tendency
IE_CGCM .... Interactive ensemble coupling strategy general circulation model
KPP .... K-profile parameterization
LH .... Latent heat
LWDN .... Long wave downward
LWUP .... Long wave upward
NCAR .... National center for atmospheric research
NCEP .... National centers for environmental prediction
OGCM .... Ocean general circulation model
PC .... Principle component
POP2 .... Parallel Ocean Program, version 2
PREC .... Precipitation
Q10 .... Specific humidity at 10 meters above ocean surface

Q_{net} .... same as Surface heat flux
SFWF .... Surface fresh water flux
SHF .... Surface heat flux
SLP .... Sea level pressure
SH .... Sensible heat
SMF .... Surface momentum flux
SSS .... Sea surface salinity
SST .... Sea surface temperature
SSTA .... Sea surface temperature anomaly
SWDN .... Short wave downward
SWUP .... Short wave upward
TAU .... Experiment TAU, monthly SMF & SFWF, climatological SHF
TAUX .... Zonal surface wind stress
TAUY .... Meridional surface wind stress
T10 .... Air temperature at 10 meters
THC .... Thermohaline circulation
TZ .... Transition zone
U10 .... Zonal wind at 10 meters
UOHC .... Upper ocean heat content
V10 .... Meridional wind at 10 meters
W500 .... Top 500 meters mean vertical velocity
YD14 .... Yeager and Danabasoglu 2014

Abstract

THE IMPACT OF SURFACE FORCINGS ON THE ATLANTIC MULTIDECADAL VARIABILITY

Liang Yu, PhD

George Mason University, 2019

Dissertation Director: Dr. Bohua Huang

The North Atlantic sea surface temperature (SST) anomalies associated with the Atlantic multidecadal variability (AMV) have major impacts on the regional and global climate. Therefore, understanding the AMV mechanisms can help us understand and predict the long-term climate variability. In addition to the SST anomalies, AMV is also manifested as persistent upper ocean heat content (HC) anomalies in the North Atlantic and low-frequency fluctuations of the Atlantic meridional overturning circulation (AMOC). It is important to understand what physical processes generate these subsurface oceanic anomalies and how they connect with the deep overturning on multidecadal time scales. Some previous studies show that the surface heat flux (SHF) anomalies play a dominant role in driving the AMOC multidecadal variability while the surface momentum flux (SMF) anomalies are more important in its seasonal and interannual variability. In this study, we first reexamine the above conclusion with a longer forcing in a newer version model. Then we further examine whether the upper ocean HC anomalies are generated differently by the anomalous SHF and SMF forcings and how the potentially different HC anomalies affect the AMOC fluctuations on multidecadal time scales. To answer these questions, a series of 600-year simulations are conducted using an ocean general circulation model (OGCM)

forced by prescribed monthly atmospheric state variables from a community earth system model (CESM) pre-industrial run. Using these OGCM runs, we diagnose how the different surface forcings contribute to the coupled model-simulated multidecadal variability. The results of these experiments confirm the results from previous studies that the SHF anomalies are dominant in driving the AMOC multidecadal variability. However, it is demonstrated that SMF anomalies can also generate substantial AMOC multidecadal variability, although its amplitude is weaker than that generated by SHF. Moreover, it is shown that both SHF and SMF can generate basin-wide HC anomalies but with distinctive spatial distributions. The HC variability generated by SHF is border and occupies most of the northern North Atlantic. In the SMF run, intense HC variability is confined to the Gulf Stream extension region and weakened quickly further north. It is further demonstrated that these HC anomalies are then advected to form a characteristic dipole pattern, which modulates the North Atlantic Current and affects the upper branch of the AMOC. On multidecadal time scales, these HC anomalies get strengthened in the North Atlantic through advection while the local SHF anomalies play a damping role to the existing HC dipole pattern. This local damping effect is stronger in the SMF run than the SHF run. A further analysis shows that the time mean and perturbation flows play compensating roles in the heat advection and the geostrophic current is more dominant than the Ekman flow.

Chapter 1: Introduction

The Atlantic multidecadal variability (AMV, also known as Atlantic multidecadal Oscillation, AMO) is a basin-wide variability on multidecadal time scales in the North Atlantic Ocean with a period of 40-70 years (Kushnir 1994; Delworth and Mann 2000). It has been found in many climate observations (Kushnir 1994) and climate proxy data (Hibler and Johnsen 1979; Roemmich and Wunsch 1984; Ghil and Vautard 1991; Thornalley et al. 2018). AMV has major impacts on regional and global climate, such as the climate over Europe and North America (Sutton and Hodson 2005; Knight et al. 2006), Sahel summer rainfall (Knight et al. 2006; Zhang and Delworth 2006), Atlantic Hurricane activity (Knight et al. 2006; Zhang and Delworth 2006; Smith et al. 2010a) and India summer monsoon (Zhang and Delworth 2006; Feng and Hu 2008). Therefore, understanding its mechanisms can help us understand the long-term climate variations and climate change.

In some studies, AMV only represents the sea surface temperature (SST) multidecadal variability in the Atlantic Ocean. In fact, multidecadal variability in Atlantic exists in both the upper and deep oceans. In this study, the meaning of AMV is broader, i.e., we consider that the AMV is the basin-wide physical multidecadal variation involving atmospheric and oceanic variables in the North Atlantic basin. In particular, the oceanic variations are manifested in the surface and subsurface variables, such as SST, upper ocean heat content (HC), and the deep overturning circulation, such as Atlantic meridional overturning circulation (AMOC).

For the upper ocean, the AMV index (Trenberth and Shea 2006; Chen et al. 2016) is commonly used in the AMV study and defined as the averaged, usually filtered, annual SST anomalies in 0-60°N over the Northern Atlantic Ocean (Knight et al. 2005; Trenberth and Shea 2006; Chen et al. 2016), which measures the basin-wide fluctuations based on ocean surface condition. The AMV index shows substantial multidecadal variations in both the observations (Trenberth and Shea 2006) and model simulations (Drews and Greatbatch 2016). Although the ocean dynamics can influence the upper ocean, SST is strongly affected by the surface thermal dynamics. Therefore, HC is another commonly used variable to measure the upper ocean variability (Grist et al. 2010; Zhai and Sheldon 2012; Buckley et al. 2014). HC represents the upper ocean heat storage and is impacted by both the thermal and dynamical processes.

In the deep ocean, AMOC is proved to be one potential ocean process that can affect the upper ocean multidecadal variability (Wang and Zhang 2013). AMOC is a large-scale oceanic circulation in the Atlantic Ocean. In this process, water goes northward in the upper layers of the ocean and sinks down to the depth around 3000 meters in the northern North Atlantic around 50°N, and then propagates southward, resulting a large among of heat and salt transport during this process. (In the literature, AMOC and thermohaline circulation (THC) are used interchangeably but the meaning is different. The name AMOC does not give us any information about the mechanism, while THC emphasizes the circulation is driven by heat and fresh water fluxes.) The pattern of AMOC is shown by the zonally-integrated Atlantic meridional overturning stream function (Zhang and Zhang 2015; Buckley and Marshall 2016). To measure the strength of this circulation, the AMOC index is defined as the maximum of the stream function. Although proxy reconstruction data of AMOC can track back to 1500 years ago (Thornalley et al. 2018), direct observations are not available until 2004 (Smeed et al. 2016, 2018). According to the recent direct observation, the strength of AMOC has been in a reduced state since 2008, compared to 2004-2008 (Smeed et al. 2018).

Numerical models are widely used in the AMV studies. On one hand, model studies can fill the gap due to limited length of time series of direct observations and large uncertainty of the proxy data. On the other hand, numerical experiments can isolate different types of surface forcings to help us understand the dynamics. In model studies, the AMV has been found not only in coupled models (Delworth et al. 1993), but also in many ocean-only models (Weaver and Sarachik 1991a,b; Weaver et al. 1993; Greatbatch and Zhang 1995; Chen and Ghil 1995; Delworth and Greatbatch 2000; Yeager and Danabasoglu 2014). The ocean models are forced by three types of surface forcings, i.e. surface heat flux (SHF), surface momentum flux (SMF), and surface fresh water flux (SFWF). In the following part of this chapter, we introduce the impacts of SHF, SMF and SFWF on the AMV, respectively. Some other theories are also introduced briefly. The last section provides the motivation of our research.

1.1 Impact of surface heat flux

The surface heat flux is proved to be an essential element for AMV (Delworth and Greatbatch 2000; Dong and Sutton 2001; Biastoch et al. 2008; Yeager and Danabasoglu 2014). Delworth and Greatbatch (2000) (hereafter DG00) perform a set of numerical experiments in an ocean-only model forced by different types of surface forcing which comes from a long coupled model simulation. When the ocean is forced by interannual heat flux and monthly climatology momentum and fresh water fluxes (Experiment HEAT), the THC index (the maximum value of the annual mean streamfunction in the North Atlantic) they have used to measure the AMOC is very similar to that of the coupled run. They also find that the low frequency portion of the heat flux is essential for the multidecadal variability of THC. Similar to DG00, Yeager and Danabasoglu (2014) (hereafter YD14) use another model, i.e. the ocean-sea ice components of the Community Earth System Model, version 1 (CESM1), and prescribe the atmospheric state near the sea surface by observations for the period of 1948-2007. They also find that, when the model is forced by the interannual heat and fresh water fluxes, i.e. buoyancy forcing, and monthly climatological momentum flux, most of the low-frequency signals of AMOC simulated by their "control" run can be very well captured.

On the contrary, some studies show that SHF may play opposite roles in local regions. Instead of generating temperature anomalies locally, Buckley et al. (2014) indicate that, in the Gulf Stream region, the role of heat flux is damping the low-frequency HC anomalies while the geostrophic convergences is the driving term. Similar result is also found by Dong et al. (2007). Also, the role of SHF may be different on different time scales. Some other studies argue that heat flux plays a minor role in interannual variation of HC in the subpolar and subtropical region (Grist et al. 2010).

1.2 Impact of surface momentum flux

Most studies show that the role of momentum flux is a stronger forcing to the shorter term (such as seasonal or interannual time scales) than multidecadal Atlantic Ocean variability (Sato and Rossby 2000; Delworth and Greatbatch 2000; Dong and Sutton 2001; Yeager and Danabasoglu 2014; Xu et al. 2014). DG00 find that when the ocean model is forced only by interannually changing momentum flux, the model cannot reproduce the multidecadal THC variability in the coupled run. Similarly, using an ocean-sea ice model forced by interannual momentum flux and monthly climatology heat and fresh water fluxes, YD14 find that the interannual variability of AMOC can be very well reproduced, while this run cannot reproduce the longer term variation. This result proves that the wind stress accounts for the high frequency variability of AMOC.

However, there are some studies indicating that wind stress may play a more important role for the AMV. Using a global coupled atmosphere-ocean-sea-ice model, Timmermann and Goosse (2004) find that when the wind stress is turned off (surface wind stress is set to zero everywere), it leads to a complete shutdown of the meridional overturning circulation. They conclude that wind stress is essential for sustaining the AMOC. Frankignoul et al. (1997) use a simple linear model forced by the wind stress with a white frequency spectrum, and find that the stochastic wind forcing may explain part of the decadal variability of the ocean gyre. Some model studies show that wind stress over the Southern Ocean is essential for the bottom ocean flow formation and local upper welling (Toggweiler and Samuels 1995; Saenko and Weaver 2004; Kuhlbrodt et al. 2007; Klinger and Cruz 2009; Lee et al. 2011). Toggweiler and Samuels (1995) find that westerly wind stress in the Southern Ocean can generate a northward Ekman transport thus remove the upwelled water out of the circumpolar zone. As a result of more upwelled deep-water removal, more new deep water forms in the Northern Atlantic Ocean. Therefore, the multidecadal variability of wind stress over the Southern Ocean may affect AMOC (Klinger and Cruz 2009). By analyzing the heat budget, Zhai and Sheldon (2012) find that the heat content warming in the Gulf Stream region between 1955-70 and 1980-95 is largely driven by large scale wind stress, but not surface heat flux.

1.3 Impact of surface fresh water flux

The fresh water flux has direct impacts on the upper ocean buoyancy and thus affecting the deep ocean circulation. Both observations (Bryden et al. 2009) and model studies (Buckley et al. 2012) have shown that the oceanic buoyancy anomalies in the northwest Atlantic Ocean play an essential role in the AMOC variability, thus impacting the SST and HC (Zhang et al. 2016). Therefore, the SFWF may be related to AMV through influencing the buoyancy anomalies. Salinity is found to be important for sustaining the AMOC (Delworth et al. 1993). Tziperman (2000) indicates that positive SFWF input may weaken or even collapse THC. Deshayes et al. (2014) investigate the relationship between the salinity and the time scale of the AMOC variability and find that salinity seems to play an essential role in the long-term AMOC variability, i.e. water is saltier when the AMOC is more intense at longer period. On the other hand, some studies show that the SFWF does affect AMV but may not play an essential role. Using an idealized model, Te Raa and Dijkstra (2003) investigate the stability of an interdecadal mode and find that the fresh water flux can affect the growth rate of that mode, but cannot influence the mechanism. Another study (DG00) shows when the ocean model is only forced by interannually changing fresh water flux, the multidecadal variability of THC is gone. Therefore, the impact of SFWF on the AMV remains unclear, same as SHF and SMF.

1.4 Other theories about AMV mechanism

In the previous sections, we have reviewed some studies about the dominant surface fluxes of the Atlantic multidecadal variability. In this section, some of the dynamics generating the oscillation are reviewed briefly.

Te Raa and Dijkstra (2002) argue that the AMOC oscillation is generated by the westward propagation of temperature anomalies in the North Atlantic Ocean. Superimposed on a mean meridional temperature gradient, these propagating temperature anomalies of the basin-wide scale modulate the upper branch of the AMOC by changing the east-west temperature difference. (According to the thermal wind theory, zonal temperature gradient can generate meridional velocity.) Furthermore, since the dominating zonal (meridional) anomalous temperature gradient at a given phase of the temperature propagation generates the meridional (zonal) overturning perturbation, which strengthens or weakens the AMOC. The corresponding vertical velocity anomalies of the strengthened or weakened AMOC thus cause temperature anomalies in the central basin (east/west boundaries). The generated temperature anomalies prompt apparent westward propagation of the existing ones and affect the temperature gradients accordingly for further propagation. The time scale of the AMOC oscillation is thus determined by the cross-basin time of the self-propelled westward propagation of the temperature anomaly. Some studies argue that the time scale is determined by the westward propagation speed of Rossby wave (Marshall et al. 2001; Frankcombe and Dijkstra 2009; Buckley et al. 2012).

Another mechanism (Dima and Lohmann 2007) is associated with three climate components: sea ice, ocean and atmosphere. Start with an enhanced THC, which generates a positive SSTA over the Atlantic Ocean. Then this positive SSTA generates a low sea level pressure (SLP) in the Atlantic Ocean and high SLP in Pacific Ocean through teleconnections. SLP anomaly over the Pacific Ocean will be imposed through the positive ocean-atmosphere feedback. Therefore, the pressure gradient between Atlantic and Pacific Oceans increases, and then generates stronger southward wind over the Greenland region.

Thus the southward wind blows more sea ice (fresh water) into Atlantic Ocean through Fram Strait, leading to the enhanced THC gets weakened. This generates a delayed negative feedback that forms an oscillation.

Besides the mechanisms mentioned above, some studies argue that AMV may be just the ocean response to stochastic atmospheric forcings (Delworth and Greatbatch 2000; Schneider and Fan 2007; Liu 2012; Tulloch and Marshall 2012; Kwon and Frankignoul 2012; Chen et al. 2016). Using a stochastically forced four-box ocean-only model, Griffies and Tziperman (1995) find a damped oscillatory THC mode. By comparing the results in the ocean-only model with a coupled general circulation model (CGCM), their results support the conclusion that THC variability in coupled model can be interpreted as the results of a linear damped oscillatory THC mode excited by atmospheric forcing. Besides revealing the importance of the heat flux to the AMV variability, in the same paper DG00 also find that THC can also show interdecadal variability when the ocean model is forced by random heat, fresh water and momentum fluxes, although this variability is different from the THC oscillation in their control run. Chen et al. (2016) use six atmospheric general circulation models (AGCM) to couple with an ocean model, a sea-ice model and a land model through the ensemble-averaged surface fluxes of the former. This type of coupled model is denoted as interactive ensemble coupling strategy general circulation model (IE_CGCM, detailed in Kirtman and Shukla 2002; Kirtman et al. 2009, 2011), which can help them separate the signal (ensemble mean of six AGCMs) and the noise of the surface fluxes. They find that the local noise heat flux and the local noise wind stress play a critical role in the SST variability in the Atlantic Ocean.

1.5 Motivation

Although many studies and progresses have been made, the impacts of the surface forcings on the AMV still remain unclear. In this study, we are particularly interested in the mechanism proposed by DG00 and YD14. YD14 conclude that the buoyancy flux accounts for most of the Atlantic multidecadal variability, whereas the momentum flux only accounts for the Atlantic interannual variability. However, some aspects are still questionable. For example, in YD14, due to limitation of the observational data, the length of the forcing is only 60 years in length (repeated for 5 times). Is the 60-year observational forcing long enough to distinguish the multidecadal effects of the momentum and heat fluxes? In order to find out how the physical processes generated by the different surface fluxes impact the AMV, resolving more cycles is necessary. Another issue associated with the observation-based flux forcing is to distinguish the natural variability and the climate trend signals. In YD14, the long-term variability in the Hovmoller diagram of AMOC at 1km is hard to tell it is a long-term warming trend or an oscillation.

Therefore, using model output data as surface forcing is a better choice. On one hand, it is long enough to resolve more AMV cycles (ten or more). On the other hand, the pre-industrial model simulation does not have the global warming trend in it. In DG00, they did use a model output as the forcing, but the model used is an old version model and the low resolution (4.5° by 7.5° for the atmosphere model and 4.5° by 3.7° for the ocean model) cannot resolve some ocean processes. Besides, the heat and water fluxes at the air-sea interface are adjusted in order to avoid the climate drift in this system, which may impact the real flux value thus affect the results. Can a new generation coupled model with higher resolution overcome those limitations and provide more insight than the DG00s original model?

Our first research goal is to reexamine the DG00's conclusion with a more state-of-the-art model. The question we want to address is what are the roles of different surface forcing components (SHF and SMF) in driving the multidecadal variability of AMOC? We know that the surface forcings always impact the upper ocean first, then they impact the deep ocean through the upper ocean. Our second research goal is to further examine whether the upper ocean HC anomalies are generated differently by the anomalous SHF and SMF forcings. The third goal in this study is to find out the connection between the upper ocean and the deep ocean. The question is how do the potentially different HC anomalies affect the AMOC fluctuations on multidecadal time scales?

In this study, we design our experiments similar to DG00 and YD14 in many aspects. We repeat some of those experiments about how ocean is forced by surface forcings, but with a more sophisticated and state-of-the-art numerical model with a much higher resolution (about 1° by 1° in the ocean model) than DG00 (about 4.5° by 3.7° for the ocean model). Our prescribed forcings come from a fully coupled CESM pre-industrial run with 600 years in length, which is much longer than YD14 and a reasonable length for multidecadal study. With such a 600-year forcing, we can not only resolve more AMV cycles to help us understand the mechanism, but also avoid the climate trend in the observational forcing. To simplify the question, only an ocean general circulation model (OGCM) is used in our study, instead of an atmosphere-ocean coupled model. Similar to Buckley et al. (2014), the heat budget analysis is used to find out how HC responds to surface forcings on a multidecadal time scales. The details about the forcing and model and experiments design are introduced in Chapter 2. After that, the model output from different experiments is evaluated. We then discuss the impacts of the SHF and SMF through heat budget analysis in Chapter 4 and 5, respectively. At the end, we conclude with a summary and discussion.

Chapter 2: Model and experiments design

2.1 Model

We use the Community Earth System Model, version 1.1.1 (CESM1.1.1) in this study. The CESM is a fully coupled climate model, including one coupler and five components for atmosphere, ocean, land, sea ice and land ice, respectively. Since our study aims at investigating how ocean responds to different surface forcings, we use only the ocean general circulation model (OGCM), including the ocean and sea ice components of CESM. Land and land ice models are not activated. The atmosphere component has a 0.9° by 1.25° horizontal resolution and is a data model mode, which only provides the prescribed surface variables that are required to force the OGCM.

The ocean component of the OGCM is the Parallel Ocean Program, version 2 (POP2, Smith et al. 2010b). The sea-ice component is the Community Ice CodE, version 4 (CICE4, Hunke et al. 2008), sometimes also referred to as Los Alamos Sea Ice Model, version 4. The ocean and sea ice models have the same horizontal resolution (approximately at 1° by 1°) and are configured on a Greenland displaced grid, with the North Pole displaced over Greenland to avoid singularity problems in the ocean and ice models. POP2 is a primitive equation model and uses the hydrostatic and Boussinesq approximations.

Compared with an earlier version used in Community Climate System Model version 3 (CCSM3), the current version has been improved significantly in many aspects, such as 60 levels in the vertical, which is 20 more levels than the previous version, overflow parameterization (Danabasoglu et al. 2010), a near-surface eddy flux parameterization (Danabasoglu et al. 2008), a better equatorial current structure, and better sea surface temperature (SST) and salinity simulations in the north Atlantic Ocean. More details about the CESM, POP2 and CICE4 can be found in Gent et al. (2011), Danabasoglu et al. (2012) and Holland et al. (2012), respectively.

2.1.1 Experiments design

The goal of our research is to understand how the oceanic processes respond to the atmospheric forcing in generating the multidecadal variability in the fully coupled CESM simulation. First, we introduce the fully coupled simulation. The fully coupled simulation is a pre-industrial simulation (no global warming trend) and conducted by NCAR for 2200 years and the monthly mean output for Year 400-2200 are available from the NCAR online datasets (case name: b.e11.B1850C5CN.f09_g16.005, http://www.cesm.ucar.edu/experiments/cesm1.1/LE/). The monthly output for Year 1201-1800 is used in this study, as there is no trend for the AMOC index (the maximum of the stream function in the northern Atlantic Ocean) index during this period and 600 years are a reasonable length for our study. On one hand, 600 years can resolve about ten AMV cycles which should be enough for the study. On the other hand, too long in length (such as 800 years) may not be necessary as it costs more computational sources and time to run the numerical experiments. This 600-year data (both atmosphere and ocean) of the fully coupled pre-industrial run is named as CPLD experiment.

There are three types of surface forcings, i.e. SHF SMF and SFWF, in which SMF is prescribed, SHF and SFWF are calculated based on the prescribed atmospheric state variables and the model-produced ocean status. For example, the bulk formula (Large and Pond 1981, 1982) is used to calculate the sensible heat (SH) and latent heat (LH) components of SHF, and the evaporation (EV) component of SFWF, i.e. $SH \sim U(T_a - T_o)$, $LH = 2.5 \times 10^6 EV \sim U(q_a - q_o)$, where U is surface wind speed, T_a/T_o is air/ocean temperature and q_a/q_o is air/ocean specific humidity. In the bulk formulae, only U, T_a and q_a are proscribed by the data atmosphere component, but the oceanic states (T_o and q_o) are different between different runs and thus different fluxes between those runs as well. We need to clarify that the bulk formulae mentioned above is just for conceptional discussion, not the one actually used by POP2. For example in POP2, U is actually substituted by $max(U_{min}, \sqrt{(U_a - U_o)^2 + (V_a - V_o)^2})$, where $U_{min} = 0.5m/s$ is the minimum wind speed set by the model to calculate the bulk formulae. There are ten atmospheric state variables prescribed directly by the data atmosphere, i.e. precipitation, downward long wave radiation, downward short wave radiation, upward short wave radiation, air density at 10m, specific humidity at 10 m, sea level pressure, air temperature at 10 m, zonal and meridional wind at 10m. Besides these ten variables, we also prescribe wind stress (TAUX and TAUY). These data are from the monthly output of CPLD experiment.

We use the same OGCM for our numerical experiments. To find out the roles of different surface forcings in the ocean variability, we run the OGCM with different forcing setups. There are several experiments, i.e. CNTL, HEAT and TAU. Except for CNTL, the names of the experiments are designed to represent the source of the surface fluxes used to force the ocean model. All of the experiments are integrated for 600 model years and use the same initial condition, which is the ocean and sea ice status in January Year 1201 of the pre-industrial run. Since the initial condition and forcings are from the pre-industrial run, we choose the same model version (CESM1.1.1) as the pre-industrial run, instead of the latest version.

For the CNTL run, all of the three surface forcings are monthly data. Positive/Negative surface flux means that flux goes into/out the ocean. Experiment HEAT is the same as CNTL, except that SMF will use monthly climatological data. Monthly climatology means that a mean value for each month over the entire 600 years, which provides a fixed annual cycle for this variable. By taking the monthly climatology for the SMF, we can eliminate the effects of the interannual variability of the momentum flux, which allows us to isolate the roles played by the anomalies of the heat and fresh water fluxes (i.e. the departure from their monthly climatology) in generating the oceanic variations. Experiment TAU is also the same as CNTL, except that the SHF will be calculated with the prescribed monthly climatological atmospheric state variables, so we eliminate the effect of SHF.

Besides CNTL, HEAT and TAU, we have also performed some other experiments, which will not be analyzed in details. Experiment CLMT uses climatology data for all three surface fluxes. Note that in the TAU case, both momentum flux and precipitation have interannual variability. In HEAT, both heat and fresh water fluxes have interannual variability. To find out the impact of SFWF, we perform two more experiments, TAUonly, and FWonly. Experiment FWonly is only forced by prescribed interannually varying SFWF, including the surface evaporation, precipitation and ice melt, whereas the latent heat flux, as all other heat flux components and momentum flux, is held as monthly climatology. Experiment TAUonly is only forced by the interannually changing SMF. The results of AMOC multidecadal variability show that FWonly is very similar to CLMT, and TAUonly is very similar to TAU. This result demonstrates that the effect of fresh water flux does not play an essential role in this model.

2.2 Summary

The goal of our research is to understand how the oceanic processes and HC respond to the atmospheric forcing in generating the multidecadal variability with 600-year forcings in the coupled CESM simulation. We use POP2 and CICE4 in CESM for our OGCM. Different atmospheric state variables are prescribed by either monthly or climatological monthly data. Based on different surface forcing setups, we have different experiments, CPLD, CNTL, HEAT and TAU and so on. Each experiment has the same initial conditions and 600 model years, long enough for the multidecadal studies. All the experiments and forcings are summarized in Tables 2.1 and 2.2, respectively.

Table 2.1: List of experiments.

Experiment	characteristics
CPLD	Output from the fully coupled CESM pre-industrial run, including atmosphere, ocean, land, sea ice, and land ice five climate components. Model year 1201-1800 of this fully coupled CESM pre-industrial run is taken in our study. This 600 years data is called Experiment CPLD.
CNTL	Output from ocean-sea ice coupled model forced by interannually changing heat, momentum and fresh water fluxes, which are from the atmospheric component of CPLD. The initial condition of the ocean-sea ice coupled model is also the same as that of Experiment CPLD, i.e. January 1201 of the pre-industrial run. There are 600 years in length for CNTL run.
HEAT	Same as CNTL except that SMF uses monthly climatology
TAU	Same as CNTL except that SHF uses monthly climatology
CLMT	Same as CNTL except that all three fluxes use monthly climatology
TAUonly	Same as CNTL except that only uses interannually changing momentum flux
FWonly	Same as CNTL except that only uses interannually changing fresh water flux

Table 2.2: List of experiments and the data types of prescribed atmospheric state variables, i.e. precipitation (PREC), downward long-wave radiation (LWDN), downward short-wave radiation (SWDN), upward short-wave radiation (SWUP), air density at 10m (DN10), specific humidity at 10 m (Q10), sea level pressure (SLP), air temperature at 10 m (T10), zonal and meridional wind at 10m (U10 and V10). "cpld" means the data is not prescribed but from atmosphere-ocean coupling processes. "mon" means the data is prescribed by the monthly data. "clmt" means the data is prescribed by monthly climatology data.

Experiment	PREC	LWDN	SWDN	SWUP	DN10	Q10	SLP	T10	U10	V10	TAUX	TAUY
CPLD	cpld	cpld	cpld	cpld	cpld	cpld	cpld	cpld	cpld	cpld	cpld	cpld
CNTL	mon	mon	mon	mon	mon	mon	mon	mon	mon	mon	mon	mon
HEAT	mon	mon	mon	mon	mon	mon	mon	mon	mon	mon	clmt	clmt
TAU	mon	clmt	clmt	clmt	clmt	clmt	clmt	clmt	clmt	clmt	mon	mon
CLMT	clmt	clmt	clmt	clmt	clmt	clmt	clmt	clmt	clmt	clmt	clmt	clmt
TAUonly	clmt	clmt	clmt	clmt	clmt	clmt	clmt	clmt	clmt	clmt	mon	mon
FWonly	mon	clmt	clmt	clmt	clmt	clmt	clmt	clmt	clmt	clmt	clmt	clmt

Chapter 3: Model evaluation

Before any sensitivity experiments, we need to answer one fundamental question: How well can the uncoupled model (CNTL) reproduce those variables in the coupled model (CPLD)? If the uncoupled model cannot reproduce the coupled model, these experiments cannot be used to answer our research questions.

In this section, we demonstrate how well the OGCM can reproduce the basic pattern and variation of different variables. To verify our experiments, the climatology status of different experiments is examined. During the first 50, especially the first 20, years there is a strong trend. This is the spin-up period when the model oceanic state adjusts to the new prescribed surface forcing. In the following analysis, we will cut off the first 100 years. For time series, 5-year running mean is taken.

3.1 Climatology

The ultimate goal of our research is always to explain the real world. Before comparing our OGCM with CPLD, we examine how well CPLD can simulate the observed SST first. Fig. 3.1a and b show the climatological SST from the observation and CPLD, respectively. Generally speaking, the SST decreases meridionally. The coldest SST appears in the Labrador Sea region along the Canadian coast. The SST gradient has the maximum value at 45°N near the eastern coast of America. In general, CPLD is very similar to the observations. However, in some areas the bias does exist. From Fig. 3.1c we find that the observational SST is overestimated by the model along the western boundary and transition zone (TZ, marked by a black box in Fig. 3.1c) and underestimated in the Gulf Stream (GS) extension region and the subtropical region with the bias around 2-3°C. The biases do exist in the model simulation. We will view the fully coupled run as our "true" value for the sensitivity experiments.

The SST pattern in CNTL is very similar to that in CPLD, except along the Gulf Stream region. Fig. 3.2 shows the climatological SST (shaded contour) of the four experiments. The uncoupled run (CNTL) has a pattern similar to the CPLD, except that the shape of the SST in the center of the ocean is different. To show this difference, we subtract the CPLD from CNTL, as shown in Fig. 3.1d. Along Gulf Stream, the SST is overestimated in CNTL by 2°C or so and underestimated in the subtropical region. The surface current difference between CNTL and CPLD (not shown) indicates that stronger current brings more warm water which warms up the GS region in CNTL. Also, the warm SST may be the reason for the overestimated current in turn. For HEAT and TAU (Fig. 3.2c-d), generally speaking, the SST in these two runs look similar to CNTL.

Since our SHF is not prescribed but calculated, the comparison of SHF between coupled (CPLD) and uncoupled experiments (CNTL) is performed to examine whether the prescribing-atmospheric-state-variable method is reasonable and the OGCM is forced by similar SHF. The climatological SHF is shown as contours in Fig. 3.2. The pattern of SHF is qualitatively similar from case to case, especially in the subtropical region. In the subpolar gyre, SHF is negative, except a small positive region near Newfoundland Canada. The maximum negative region is along the GS. SHF in the coupled model (CPLD) is overestimated by the uncoupled model (CNTL) along the Gulf Stream (GS) region and underestimated in the GS extension region, as shown by the contours in Fig. 3.1d. We confirm that prescribing the atmospheric state variables can get similar SHF as prescribing the SHF directly. Plus we have more advantages by prescribing atmospheric variables. For example, the flux is the result of the interaction between atmospheric variables and the ocean variables. In the future studies, we can further prescribe either wind speed or surface air temperature, so we can further investigate the surface heat flux is from the fluctuation of wind or air-sea temperature difference.

Next, we investigate the wind stress climatology, shown by wind at 10 m in Fig. 3.2d. As the climatological wind in all cases is the same for all runs, it is only shown for TAU.

The pattern of the surface wind stress is anticyclonic in the subtropical gyre region, which is the result of geostrophic balance with subtropical high.

In our numerical experiments design, the bulk formula surface heat flux parameterization determents the SST in a great way. The SST climatology similarity may not be a good indicator for a successful simulation. Therefore, the climatological HC, averaged sea water temperature over the upper 500 meters, is plotted in Fig. 3.3 to further evaluate the model simulation. The pattern of HC climatology is very similar to SST climatology, i.e. minimum value in the northwest of the basin and maximum value in the southwest region. Along GS, there is a large meridional HC gradient. Although we can find that the area of the maximum HC climatology for TAU is slightly larger than CNTL and HEAT, other than that all the four runs look similar to each other. Another advantage of HC is that HC field can also represent the gyre pattern.

The reconstruction of climatology is not only good at the upper levels, but also good in the deep ocean. Fig. 3.4 shows the barotropic streamfunction (BSF) climatology for different runs. Positive BSF represents an anticyclonic gyre in the subtropical region (subtropical gyre), and negative BSF represents a cyclonic gyre in the north (subpolar gyre). Here we use a 5-Sv contour line representing the trajectory of Gulf Stream and its extension. This line is also the boundary between the subtropical gyre and subpolar gyre. For all four runs (Fig. 3.4a-d), the BSF patterns look very similar to each other, which means that the climatology of the large-scale horizontal gyre circulation is very well reproduced by different CNTL, HEAT and TAU.

As indicated by Wang and Zhang (2013), AMOC may be an important ocean circulation that impact the upper ocean. Fig. 3.5a shows the climatology and variance of the AMOC stream function for the CPLD simulation. The AMOC stream function can present the meridional transportation in the Atlantic Ocean. The position of the maximum AMOC stream function is located in the latitude around 35°N and 1 km in depth. It indicates the water northward transportation occurs in the upper ocean above 1 km, sinks down between 40°N-60°N, and goes back to the south below 1 km. The maximum AMOC transportation for CPLD is about 24 Sv, which is higher than the observations (13-20 Sv, Buckley and Marshall 2016). Comparing Fig. 3.5a and b, we can find that the pattern and strength of the AMOC stream function for CNTL is very similar to CPLD. If we take the difference between these two experiments, as shown in Fig. 3.6, we can find that our OGCM underestimates AMOC about 1-2 Sv in the depth 1.4 km to the surface and 3.4 km to the bottom, and overestimates AMOC between 1.4 km to 3.4 km in vertical and the beyond latitude 40°N in the north. The similarity between Fig. 3.5a and Fig. 3.5b can demonstrate that our OGCM can simulate the AMOC climatological pattern well. Fig. 3.5c and d show that the maximum AMOC location for HEAT and TAU is around 35°N and 1 km in depth with the value around 22-24. The location, value and shape of AMOC for HEAT and TAU are similar to CNTL.

The climatology of AMOC stream function, SST, HC, SHF and wind stress have been examined. There are many similarities between CPLD and CNTL, HEAT and TAU, which demonstrate that, when it is uncoupled, the model can successfully simulate the basic climatological features of the ocean.

3.2 Multidecadal variability

After comparing the stationary state (the climatology) of different variables in different runs, in this section we examine how those variables vary. We need to clarify some details about how the data is processed. The annual mean is calculated from the monthly output data, climatological mean is removed and 5 year running mean is applied. The first 100-year spin-up period is cut off and only the last 500 years data is used.

3.2.1 Comparison of AMOC variance

The AMOC variance is mainly driven by SHF. The maximum of the AMOC stream function variance (black contour in Fig. 3.5) occurs in the close position as the maximum of the stream function (Fig. 3.5a-d). However, the magnitude of the variance varies from case to case. CNTL has a larger AMOC variance than CPLD in both the maximum variance

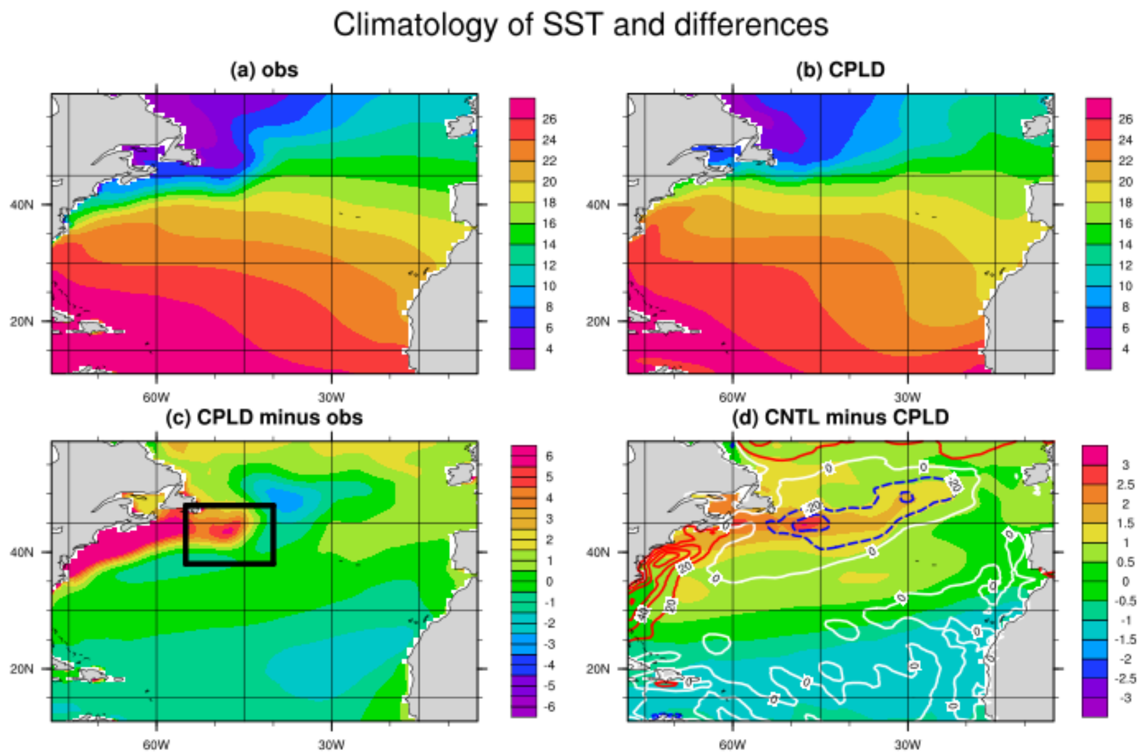

Figure 3.1: Climatology SST of (a) the Hadley centre observational data over year 1870-1998 and (b) fully coupled CESM over year 101-600. Unit is °C. The climatological SST differences between (c) observation and CPLD, and (d) CNTL and CPLD are also shown. The climatological surface heat flux (W/m^2) difference between CNTL and CPLD is shown in panel (d) by contours. The black box (38°-48°N, 305°-320°W) in panel (c) indicates the transition zone (TZ).

and the area. The maximum variance of the CNTL, i.e. 2.20, is substantially larger than that of CPLD, which is 1.53. Variance of HEAT is very similar to that of CNTL, whereas variance of TAU is much smaller than both HEAT and CNTL. It seems that the AMOC

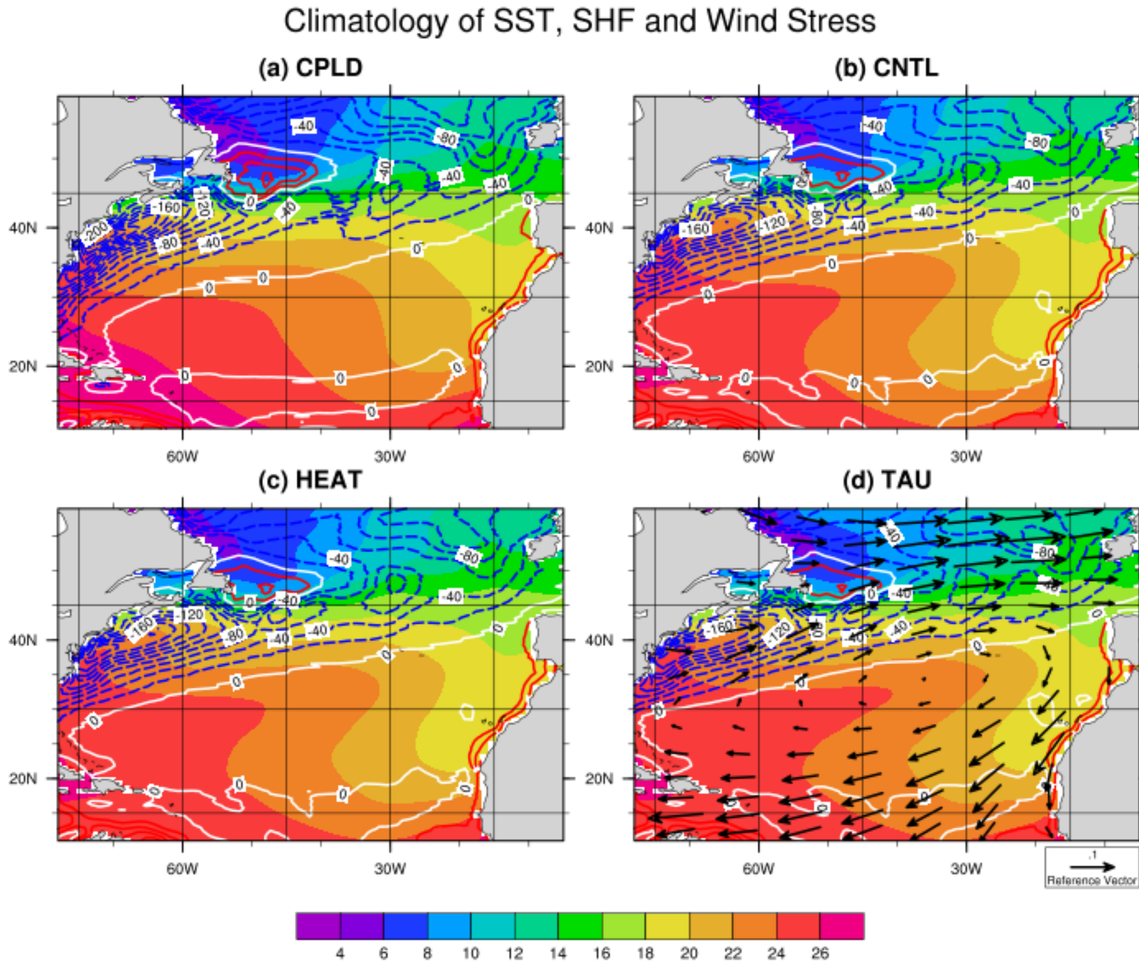

Figure 3.2: SST, SHF and wind stress climatology for four experiments over year 101-600, with the unit °C, W/m^2 and N/m^2, respectively. Color bar stands for SST climatology. Contour lines stand for SHF climatology, where white is zero line, red is positive SHF and dashed blue is negative SHF. Positive/Negative surface flux means that flux goes into/out the ocean. The climatology of the surface wind stress is only shown as black arrows in (d) TAU, because wind stress climatology is the same for all four experiments.

variance is mainly driven by the variance of the surface heat flux, not the momentum flux. This conclusion is consistent with some other studies (DG00, YD14).

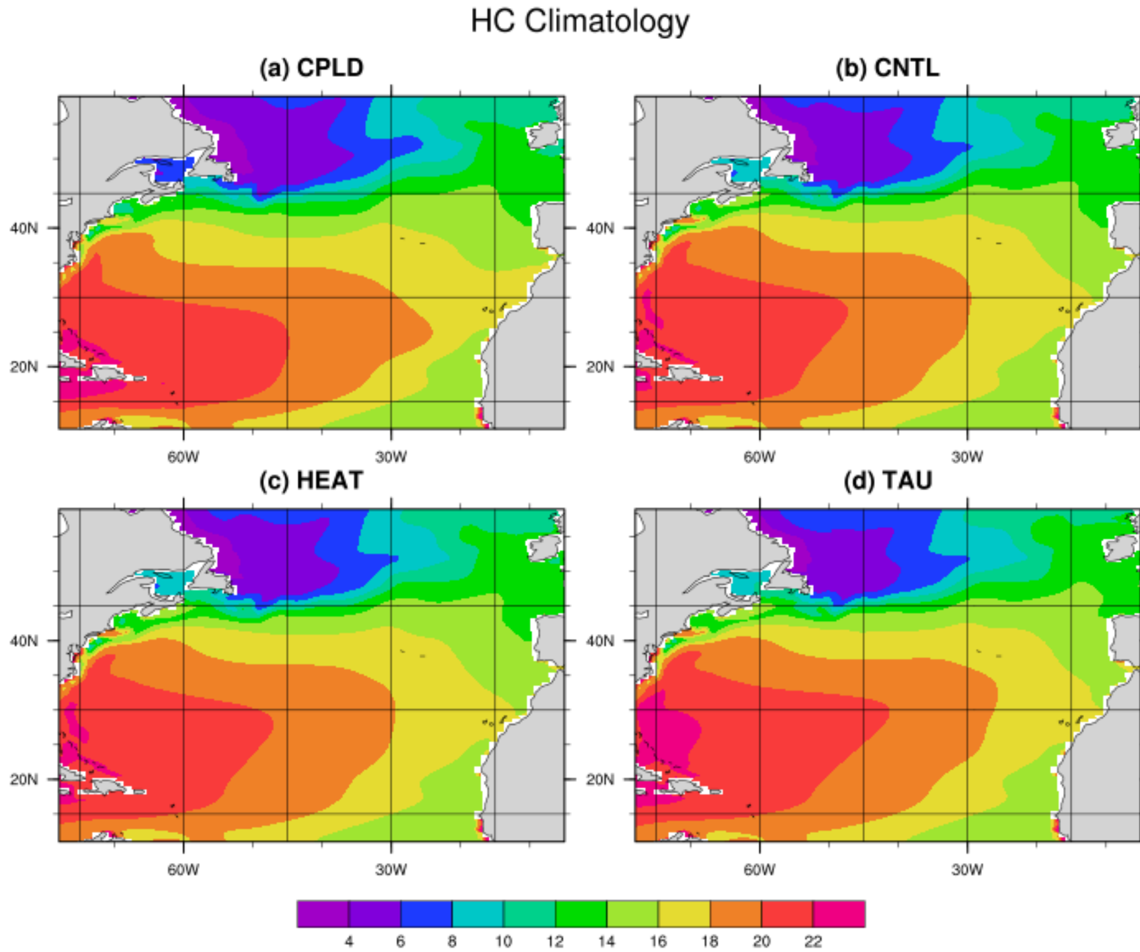

Figure 3.3: Climatological HC over year 101-600 for different experiments. Unit is °C.

3.2.2 Comparison of indices

In this section, we compare the AMOC variations among different experiments by examining the time evolution of AMOC Index (Fig. 3.7), defined as the maximum value of the meridional stream function in the North Atlantic. This index is calculated in monthly data then the annual is taken and then five-year running mean is applied, as we focus on the decadal to multidecadal time scales in this study. The uncoupled model (CNTL) can

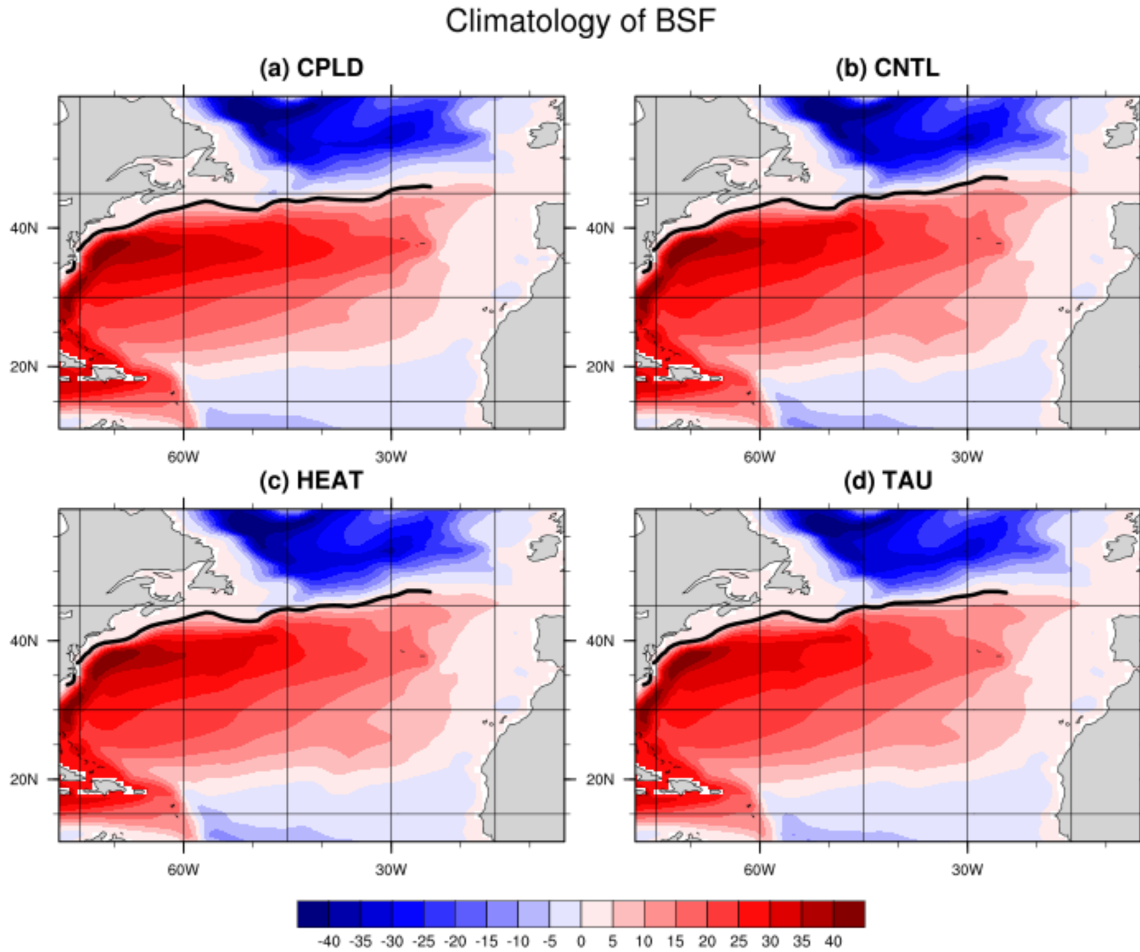

Figure 3.4: Climatological BSF over year 101-600 for different experiments. Unit is Sv. The black line is the 5 Sv contour line, representing the Gulf Stream trajectory and its extension.

successfully reproduce the multidecadal AMOC variability in the coupled model (CPLD), as shown in Fig. 3.7a the AMOC index of CNTL is very close to CPLD. The correlation between them is 0.73, as shown on top of panel Fig. 3.7a. HEAT is also similar to CNTL when it comes to AMOC index with a correlation coefficient of 0.82 between these two runs, shown in Fig. 3.7b. SHF plays an essential role in driving AMOC variability, which

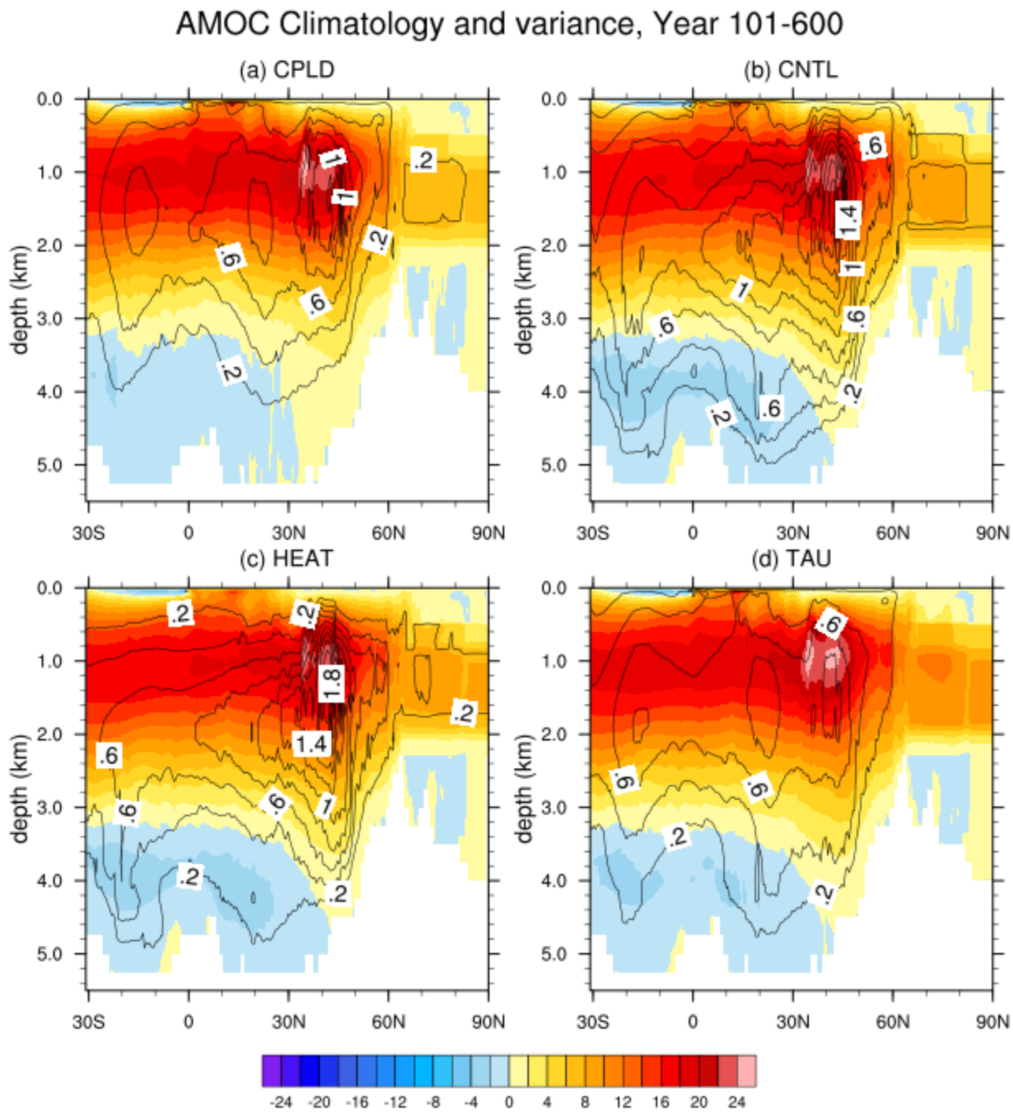

Figure 3.5: AMOC climatology (shaded contour) and variance (black contour) of the stream function over year 101-600 for (a) CPLD, (b) CNTL, (c) HEAT and (d) TAU. The maximum variance is 1.53, 2.20, 2.15, 0.92, respectively. AMOC unit is Sv.

is similar to what DG00 found. Some previous studies show that the momentum flux only counts for the short-term high frequency AMOC variability, whereas the heat flux drives the low frequency AMOC variability (DG00, YD14). However, in our TAU case, in which the ocean is mainly forced by the SMF, the model can still simulate some of the AMOC interdecadal variability. Although the correlation between CNTL and TAU is not very high

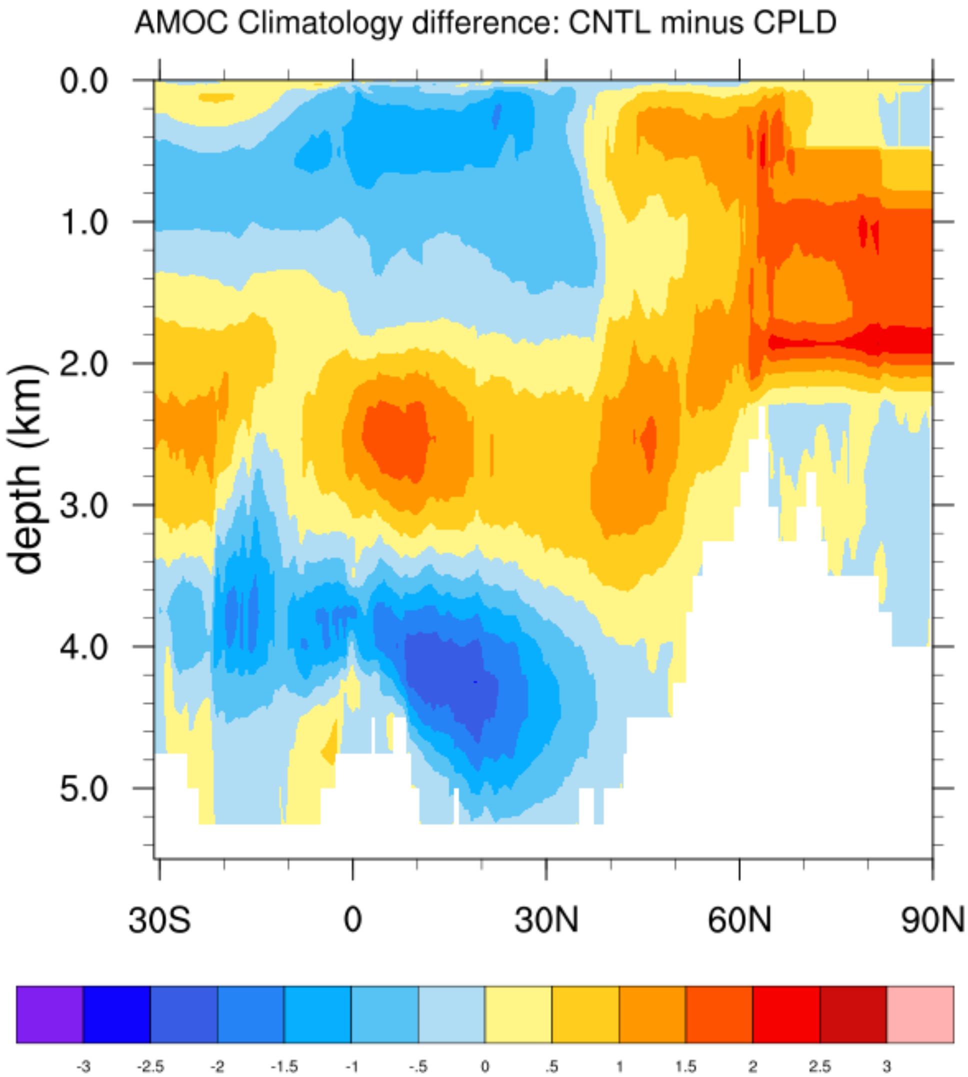

Figure 3.6: AMOC climatology difference between CNTL and CPLD. Unit is Sv.

(0.27), it is higher than the 95% significant level (0.087). The amplitude of TAU, quantitatively described by the standard deviation 0.53, is smaller than that of HEAT (0.90) and CNTL (0.85), consistent with the variance results shown in Fig. 3.5.

In fact, in the TAU run, the precipitation is also prescribed by the monthly mean data. It is a little hard to tell the multidecadal variability in TAU is driven by interannual SMF variability or by SFWF. To answer this question, we perform another experiment named as TAUonly, in which we eliminate the impact of SFWF in TAU run and only keep the interannual variability of SMF. To save some computational core hour, we only run the TAUonly experiment for 100 years. We find that the AMOC variability in TAU and TAUonly is very similar, as shown in Fig. 3.8. The correlation between these two runs is as high as 0.97. We conclude that in the TAU run, the AMOC variability is driven by SMF.

To investigate this multidecadal variability in the Atlantic is an ocean internal damped mode or a mode due to ocean internal instability, experiment CLMT is performed, as shown in Fig. 3.9. In CLMT run, all atmospheric surface state variables are prescribed by the monthly climatological data. If the multidecadal variability is due the ocean internal instability, this variability should be seen in CLMT. However, we find that if we turn off the variability of the atmospheric surface variables, the AMOC multidecadal variability is gone (see Fig. 3.9). This result indicates that at least in this model the multidecadal variability is a damped mode. The ocean variation will be damped if there is no surface forcing variation.

Besides AMOC index, AMV index is also very important and commonly used in the Atlantic Ocean variation studies. Fig. 3.10 shows the AMV index, which is defined as the mean SST between 10°N to 60°N in Atlantic Ocean. First of all, we can see that the AMV indices in CNTL and CPLD are very similar to each other with a correlation of 0.93 (Fig. 3.10a). Moreover, the AMV indices in HEAT and CNTL are almost exactly the same (Fig. 3.10b) with a correlation as high as 0.99. On the other hand, AMV in TAU has an very small magnitude and less correlated with CNTL (0.42).

The different characteristics in the AMV indices between CNTL (as well as HEAT) and TAU experiments can be explained partly by their different surface heat flux formulations. In general, the SST anomalies can be generated by the SHF anomalies. Since the interannualy changing surface air temperature and wind speed are prescribed in both CNTL and HEAT, they may nudge the model SST toward the prescribed surface air temperature in the same way and produce similar SST anomalies. On the other hand, since the climatological surface wind and air temperature are prescribed in TAU, the resulting surface heat flux nudges the model SST toward the prescribed air temperature climatology. Therefore, the surface heat flux not only does not generate SST anomalies but also damps the SST anomalies produced by other ocean processes. As a result, the fluctuation of the AMV index is generally small in TAU.

As we mentioned before, HC is less strongly impacted by the surface heat flux as SST. Similar to the definition of AMV index, HC index is defined as the mean HC over the entire northern Atlantic Ocean between 10°N to 60°N. By examining the HC index, we can avoid the dominant direct local impact from the SHF on SST. The comparison of HC index among CNTL HEAT and TAU (Fig. 3.11) is similar to that of the AMV index (Fig. 3.10b). Although the HC index in TAU is not quite similar to CNTL (correlation coefficient is only 0.29, as shown on top of Fig. 3.11), the amplitude of TAU is close to CNTL and HEAT.

In our experiment, HC is actually very similar to SST, which gives us another good reason to study HC. Fig. 3.12 shows the comparison between AMV index and HC index for each case, respectively. The first impression from this figure is the high coherence between HC and AMV for every run (except for TAU) as quantified by their high correlations all above 0.8 in CPLD, CNTL and HEAT runs. Even for TAU, the simultaneous correlation is above 0.5 and statistically significant. The similarity between the HC and AMV can also be found in the lead-lag correlation in Fig. 3.13a. In Fig. 3.13a, the symmetry between the correlation with respect to the zero lag for CPLD, CNTL and HEAT suggests that the SST and HC are interactive with each other or SST forcing the HC. On the other hand, the lead-lag correlation for the TAU run is less symmetric with respect to y-axis, showing a more clear pattern for the HC forcing SST. The second impression is the small magnitude for TAU (Fig. 3.12d), which is consistent with Fig. 3.10b. Another feature of HC in Fig. 3.12 is that HC fluctuation is smoother and with less variability than in AMV. This means that a part of SHF generates higher frequency SST fluctuations but is smoothed out in HC. In Fig. 3.13a, the lead-lag correlation between HC and AMV shows that there is no lag between them. This may suggest that the SHF heats up the surface, and then this heat goes into the deep ocean quickly. If we look carefully, however, HC leads AMV one year for TAU, which demonstrates that SST in TAU is dominated by HC from below, not the heat flux from the top. Some studies demonstrate that AMOC and HC might be correlated (Trenary and DelSole 2016). We do see an asymmetry of the lead-lag correlation between AMOC and HC in Fig. 3.13b, suggesting that the AMOC leads HC for some of these runs.

3.2.3 HC spacial variation

In the previous section, we investigated the HC index variation. Note that the HC index only represents the mean HC of the Atlantic ocean in the northern hemisphere. However, the entire basin doesn't change synchronously. Fig. 3.14 shows the regression of the each point of the HC field on the HC index for four runs. For CPLD, CNTL and HEAT (Fig. 3.14a-c), the northern Atlantic Ocean between 40-60°N is more in phase with the entire basin mean (the HC index). Some regions are opposite to the HC index, such as the western part in the subtropical region for CPLD and CNTL and the Gulf Stream region for TAU.

To find out the HC variability in different regions, HC variance for each grid point is plotted. Fig. 3.15 shows the HC variance spacial distribution by plotting the HC variance for each grid point. HC has the maximum variance for all four cases in the GS region. Comparing Fig. 3.15a and b, one can see that CNTL has a larger variance than CPLD, although their patterns are very similar. The HC variance of CNTL larger than CPLD is also consistent with the AMOC variance of CNTL larger than CPLD as shown in Fig. 3.5. The pattern in HEAT (Fig. 3.15c) is also close to CNTL and CPLD. However, in TAU, the HC variance is very significant in GS region, but small in the northeast basin, as shown in Fig. 3.15d. The maximum of SHF variance is co-located with the maximum of HC variance for all four runs. However, at this moment we cannot tell the SHF variance is the cause or the result, i.e. forcing or damping, of HC variance. In the later section, the heat budget analysis will provide more insight about this issue. For Fig. 3.15d, SHF variance must be the result (damping) of HC variance, because the atmospheric state is prescribed by climatological data in our model setup for TAU.

To get more details on the spatial distribution of the HC correlations between different cases, maps of point-to-point HC correlations are plotted in Fig. 3.16. The point-to-point correlation between CNTL and CPLD is very high for most areas in Fig. 3.16a, except along GS and eastern Atlantic Ocean, although the correlation is still above 0.5 in those areas. The correlation between CNTL and HEAT is also high for the entire Atlantic basin except in the southeast (Fig. 3.16b). In Fig. 3.16c, the HC correlation map between CNTL and TAU shows that three banded areas have higher correlations, the GS area, the southwest area and the tropical area. It seems that SMF has a strong impact on the GS area. Not only HC in TAU case has its maximum variance in this region, but also HC correlation between CNTL and TAU is very high here. Interestingly, the high correlation areas in Fig. 3.16c is the low correlation areas in Fig. 3.16b. It seems that heat flux and momentum flux are dominant in different areas of the total variability and they are complementary to each other. The TAU and HEAT runs are positively correlated in the northern Atlantic Ocean (marked as a red rectangle in Fig. 3.16d) and some areas in the subtropical region.

3.2.4 EOF analysis of HC

To further analyze the HC spacial variation, the Empirical Orthogonal Functions (EOF) analysis is performed in this section. To account for the area effect of the latitude, at each grid point the raw data is multiplied by a weight ($weight = \sqrt{cos(lat(x,y))}$). Fig. 3.17 and Fig. 3.18 show the first two EOF leading modes of the HC anomalies for the four experiments, respectively. The essential portion of EOF1 pattern is located in the GS region. There is a negative anomaly in the subpolar region for CPLD, CNTL and HEAT (Fig. 3.17a-c), but not as strong as the positive pattern in the GS region. The EOF2 pattern is mainly in the Northern Atlantic Ocean between 40-60°N.

Comparing Fig. 3.17 and Fig. 3.18 with Fig. 3.15, we can find that the EOF patterns are in good agreement with the variance pattern. The EOF1 represents the GS part of the HC variance, whereas EOF2 represents the northern part of the HC variance that shows a monopole pattern around 20°-40°W and to the north of 45°N. For the TAU simulation, the northern portion of the variance (in the subpolar gyre region) are relatively weak compared with the GS part (Fig. 3.15d), and its northern part of EOF1 (Fig. 3.17d) and EOF2 (Fig. 3.18d) are weak. The TAU EOF1 explains about 40% of the total variance and EOF2 in TAU explains 18% variance. This is in agreement with the TAU HC variance along the GS extension region is much larger than the northeast region. Therefore, the EOF patterns are consistent with the variance pattern. Moreover, EOF1 plus EOF2 can explain more than half of the variation (the variation explained by each mode is shown on the top each panel in Figs. 3.17 and 3.18).

The first principle component (PC1) and second principal component (PC2) are plotted at the bottom of their EOF patterns in Fig. 3.17e and Fig. 3.18e, respectively. The PCs represent the changes of the corresponding EOF patterns with time. The PC1 correlation between CPLD and CNTL is 0.67, shown on the top of Fig. 3.17e. The correlation between CNTL and HEAT is not as high as those for AMOC and AMV between the two runs, but still very significant (0.75). The high PC1 correlation between those cases demonstrates that CPLD, CNTL and HEAT have not only a similar EOF1 pattern in space, but also a similar variation of that pattern. Although CNTL and TAU are less correlated than CNTL and HEAT, the value 0.42 is still significant at the 5% significant level (0.20). Also we can find TAU captures most of the interdecadal variability of CNTL. We also find that the PC1 in the TAU experiment is more significantly correlated with CPLD (correlation is 0.60) than the HEAT run (correlation between CPLD and HEAT is 0.16, not significant for the 5% significant level 0.20). In the GS region, the wind stress seems more important than the SHF. Moreover, the PC1 correlation between HEAT and TAU is only -0.16 and not significant, which means that the impacts of SMF and SHF on the GS region are independent to each other. PC2 has a similar conclusion to PC1. The PC2 correlation between CPLD and CNTL is the same as that between CNTL and HEAT, i.e. 0.68. Although the correlation between CNTL and TAU (0.45) is smaller than 0.68, it is still significant compared with the 5% significant level. The TAU run captures more PC2 variation in the CPLD than the HEAT run, as the PC2 correlation between CPLD and TAU (0.64) is higher than CPLD and HEAT (0.12). The HEAT and TAU runs only have a 0.07 correlation coefficient for

PC2 and again this coefficient is not significant.

The lead-lag correlation between PC1 and PC2 is calculated and plotted in Fig. 3.19a. By definition, PC1 and PC2 are orthogonal. Therefore, their correlation is zero at lag 0 for all four experiments. We also find that PC1 leads PC2 for about 5 years in CPLD, CNTL and HEAT runs. It seems that EOF1 and EOF2 represent different phases of the HC propagation along the subpolar gyre. To further demonstrate the HC anomalies propagate along GS and subpolar gyre, 19 points are selected based on the track of subpolar gyre and EOFs regions (Fig. 3.20). We take the HC time series from grid 1 to grid 19 and plot the hovmoller diagram, shown in Fig. 3.21. To show the propagation clearly, only a 100-year segment is chosen. Also the HC anomalies propagation during the chosen period (Year 500-600) is particular clear compared with other periods. As time passes by, we can see the HC anomalies propagate along small grid number to big grid number, which mean that this propagation is along the subpolar gyre. For TAU in Fig. 3.21d, the propagation is limited in the GS region.

3.2.5 HCgulf and HCnorth

As we mentioned above, EOF1 pattern overlaps the GS part of the HC variance and EOF2 overlaps the HC variance in the subpolar gyre region. These two regions seem significant for the HC variance. Therefore, two new indices are defined, i.e. HCgulf and HCnorth. HCgulf is defined as the mean HC over GS region (the blue rectangle region in Fig. 3.17a), and HCnorth is defined as the mean HC over the Northern Atlantic Ocean (the red rectangle region in Fig. 3.18a).

Comparison of the two newly defined indices between different experiments shows that SMF can reproduce the multidecadal HC variability in some local regions, such as GS extension region and northeast of the Atlantic Ocean. The time series of HCgulf and HCnorth is shown in Fig. 3.22a and b, respectively. The HCgulf correlation between CNTL and HEAT is 0.75, whereas it is 0.56 between CNTL and TAU. During some periods, such as year 400-600, HCgulf in TAU captures most of the decadal variability of the same index

Table 3.1: Summary of correlation between PC1 and HCgulf, and PC2 and HCnorth for each experiment.

correlation between	CPLD	CNTL	HEAT	TAU
PC1 & HCgulf	0.89	0.90	0.90	0.92
PC2 & HCnorth	0.91	0.77	0.92	0.87

in CNTL. The similarity of this index between TAU and CNTL proves that SMF can reproduce the HC variance along the GS extension region. The amplitude of HCgulf is between -1.6 to 1.6°C (Fig. 3.22a), which is larger than HC index (Fig. 3.11) and HCnorth index (Fig. 3.22b). This is what we should expect, because this region has the maximum HC variance (Fig. 3.15). Although the HC index for TAU is small compared with CNTL and HEAT runs, HCgulf for TAU has the same magnitude as the other experiments. This is also consistent with the result that the TAU variance is significant in GS region. The HCnorth correlation between CNTL and HEAT is 0.88, whereas it is 0.56 between CNTL and TAU. For the TAU run, although HC variance in the subpolar gyre region is relatively small (Fig. 3.15d), HCnorth still captures most of the decadal to multidecadal variation of CNTL run and have a correlation of 0.56 with CNTL (Fig. 3.22b), although with a smaller amplitude.

Furthermore, the comparisons between PC1 and HCgulf, and PC2 and HCnorth are also performed. We find that PC1 and PC2 are highly correlated with HCgulf and HCnorth, respectively. The correlation between PCs and local HC average is summarized in Table 3.1. Most correlations in Table 3.1 is around 0.90. This result further demonstrates that HC variance can be decomposed into two modes, the GS mode, i.e. EOF1, and the subpolar mode, i.e. EOF2.

So far both the AMOC and HC have been discussed. In the last part, let's investigate the relationship between the deep ocean circulation and the HC. Although AMOC and HC are not significantly correlated (Fig. 3.13b), the lead-lag correlation between AMOC and HCnorth has a peak when AMOC leads for 4 years (Fig. 3.19b). One possible reason why AMOC leads HCnorth is when AMOC gets its maximum, more heat will be transported to the north and accumulate there. Four years later, the accumulated HC gets its maximum in the subpolar gyre, so HCnorth gets its peak. The lead-lag correlation between AMOC and HCgulf is negative near lag 0 and the negative peak year varies among runs. Is the horizontal HC gradient positively correlated with the AMOC index, based on the thermal wind theory? To answer this question, a new index HCgrad, defined as HCnorth minus HCgulf, is used to represent the zonal temperature gradient. The lead-lag correlation between AMOC index and HCgrad (Fig. 3.19d) is very similar to HCnorth (Fig. 3.19b). It seems that the variation of HCgrad is dominated by HCnorth, not HCgulf, although the amplitude of HCgulf is larger. Even if AMOC and HCgulf are negatively correlated around year 0, AMOC and HCgrad doesn't have a larger lag correlation peak than AMOC and HCnorth. After all these comparisons, we conclude that AMOC is not correlated with the entire upper ocean variation (HC index), but it is correlated with the HC in the northeast region (HCnorth) with a lead of four years. This may be an evidence how the ocean dynamics can impact the upper ocean variability.

3.3 Summary

In this chapter, we evaluate our model simulation. For all the numerical experiments, an important question is how well the model can simulate the real world. At first, we compare the SST climatology difference between the pre-industrial CESM run (Experiment CPLD) and the observation. Although there are some differences along Gulf Stream (GS) and its extension region, in general the model can simulate the observational SST climatology. The comparisons of the climatology of AMOC, SST, HC, barotropic stream function (BSF) and surface heat flux (SHF) among CPLD, CNTL HEAT and TAU experiments show that our OGCM (CNTL run) can reproduce CPLD very well. HEAT run is similar to CNTL in a great degree. The climatology patterns of those variables in TAU have some bias to CNTL, but are still very close. These results indicate that the uncoupled model (CNTL run) can reproduce the climatology of ocean variables in coupled model (CPLD) and both SHF and surface momentum flux (SMF) have minor impacts on the climatological patterns.

After the climatology comparison, we examine the multidecadal variability of AMOC index, AMV index and HC index among different experiments. When the model is changed from a fully coupled model (CPLD) to an uncoupled model (CNTL), the uncoupled model can reproduce most of the variability in the coupled model, as the indices between CPLD and CNTL are very similar. Similar to DG00 and YD14, SHF plays a key role in driving the multidecadal variability. The AMOC index, AMV index and HC index in HEAT capture most of the variability of those indices in CNTL. Different from DG00 and YD14, who indicate that SMF dominates the interannual variability of AMOC, we find that SMF (TAU run) can also capture some of the multidecadal variation in Atlantic Ocean. The AMOC index correlation between TAU and CNTL is 0.27, higher than the 95% significant level. Although, both of SFWF and SMF variation exit in TAU, the impact of SFWF is very small. The AMOC multidecadal variability is an ocean internal damped mode, because no AMOC variability is found in CLMT run.

In each experiment, HC index variation is similar to AMV index. The correlation between HC index and AMV index is above 0.85 in CPLD, CNTL and HEAT, and 0.51 in TAU. For CPLD, CNTL and HEAT, HC index has a smaller amplitude and is smoother than AMV index, as SHF fluctuation can only affect a thin layer of the surface ocean. In TAU, HC has the same amplitude as AMV, sometimes even larger, because the SST in TAU should be affected more by the ocean dynamics than by the SHF.

The HC variance also demonstrates that uncoupled model (CNLT) captures the HC variance in the coupled model (CPLD) in the northern ocean, and SHF is essential for the HC variability. SMF only generates the HC variance along the GS extension region. The HC correlation between CNTL and TAU is also higher in GS extension region than other regions. The point-to-point HC field correlation further demonstrates that CNTL is in good agreement with CPLD everywhere. HEAT is very similar to CNTL almost everywhere. The HC in the HEAT and TAU runs are not significant correlated, which may imply that the impacts of SMF and SHF on AMV are independent to each other. The HC has its maximum variance in the GS region for all the experiments. For CPLD, CNTL and HEAT, HC variance in the subpolar gyre region is also high, but not for TAU.

EOF analysis diagnoses that the HC variance pattern can be decomposed into two modes, i.e. the GS mode (EOF1) and the northeast mode (EOF2) for all four experiments. The sum of these two modes explains more than a half of the total HC variance. Not only the EOF1 pattern located in the GS region, but also the PC1 is highly correlated with the HCgulf index (the regional mean HC in GS region). Similarly, the PC2 is significantly correlated with the HCnorth (the regional mean HC in the Northern Atlantic Ocean). We also find that PC1 leads PC2 for about 5 years, which implies that EOF1 and EOF2 present different phases along the HC anomalies propagation trajectory. The PC1 correlation between HEAT and TAU is not significant, either is PC2. This may indicate that SHF and SMF have independent impacts on HC variability.

Further analysis of the two local indices, i.e., HCgulf and HCnorth, shows that SMF drives the regional HC variance, such as the GS region. Although the HC index is small in the TAU run, TAU's HCgulf has a similar amplitude as CNTL and HEAT. Wind stress can also reproduce the HC multidecadal variability in the sub-polar gyre region, as the HCnorth index correlation coefficient between TAU and CNTL is 0.56, although with a smaller magnitude in TAU.

The relationship between the upper ocean HC and the deep ocean circulation is also investigated by calculating the lead-lag correlation between AMOC index and local HC index. Although AMOC is not significantly correlated with the entire basin HC variability (HC index), AMOC is correlated with some local HC variability. AMOC index leads HCnorth for 4 years, as the HC accumulation in the northern region takes time. HCgulf is negatively correlated with AMOC index around lag 0. The specific lagged year varies in different runs.

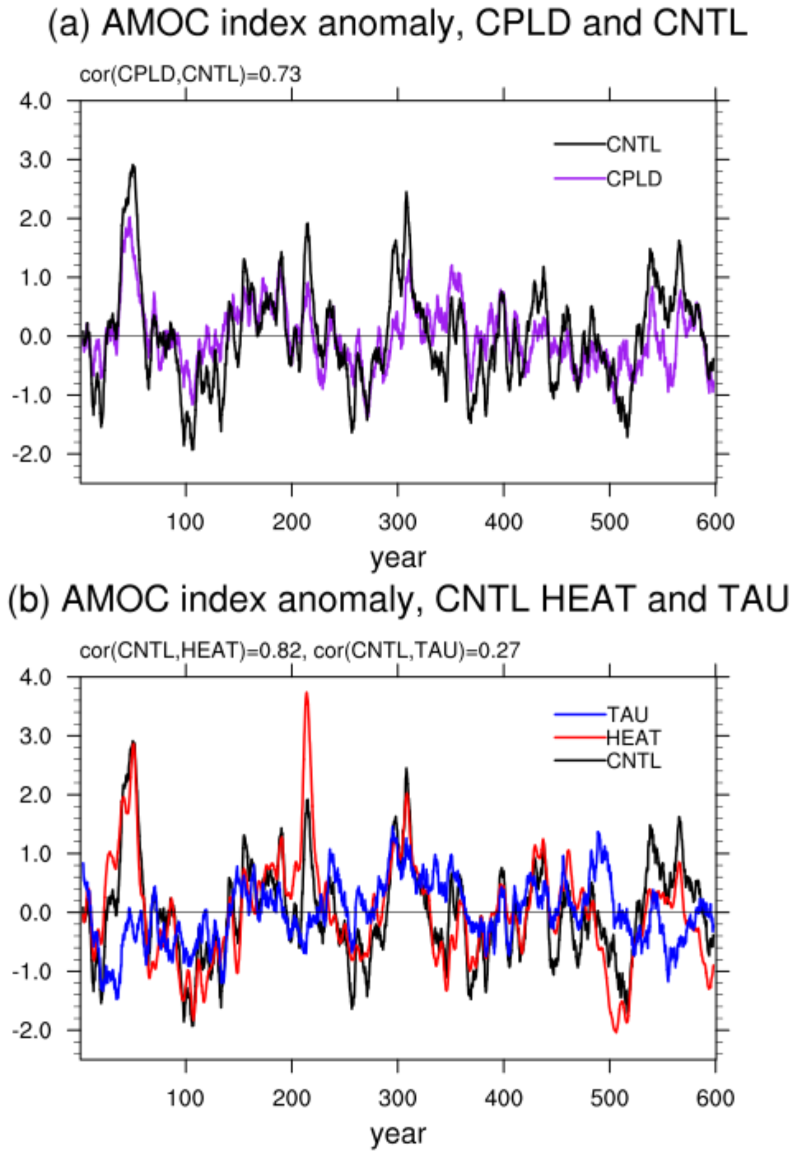

Figure 3.7: Five-year running mean AMOC index. Comparison between (a) CNTL and CPLD, (b) CNTL, HEAT and TAU. Unit is Sv. The correlation between different cases is shown under the title for each panel. The standard deviation for CPLD, CNTL, HEAT and TAU is 0.54, 0.85, 0.90 and 0.53, respectively.

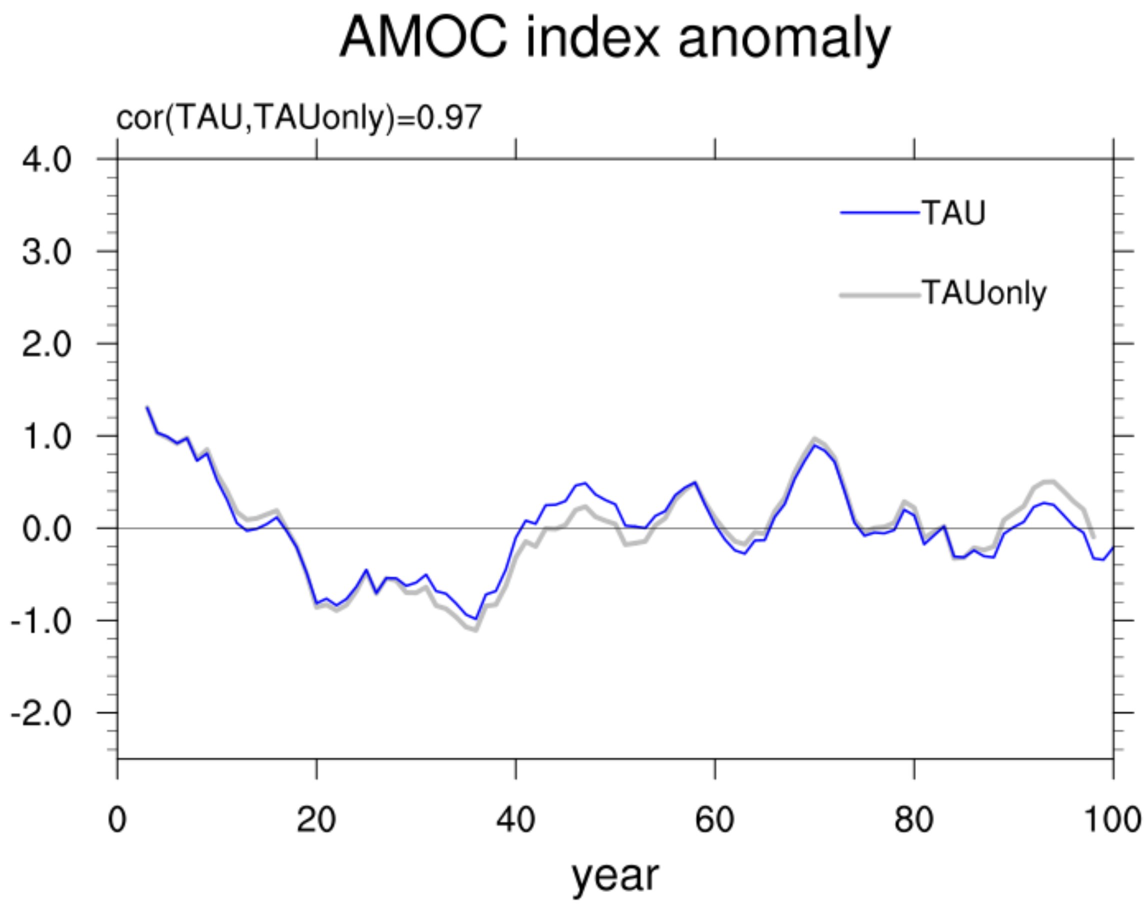

Figure 3.8: AMOC 5-year running mean index over 100 years. Comparison between TAU and TAUonly. Unit is Sv. The correlation between TAU and TAUonly is 0.97 (top-left corner).

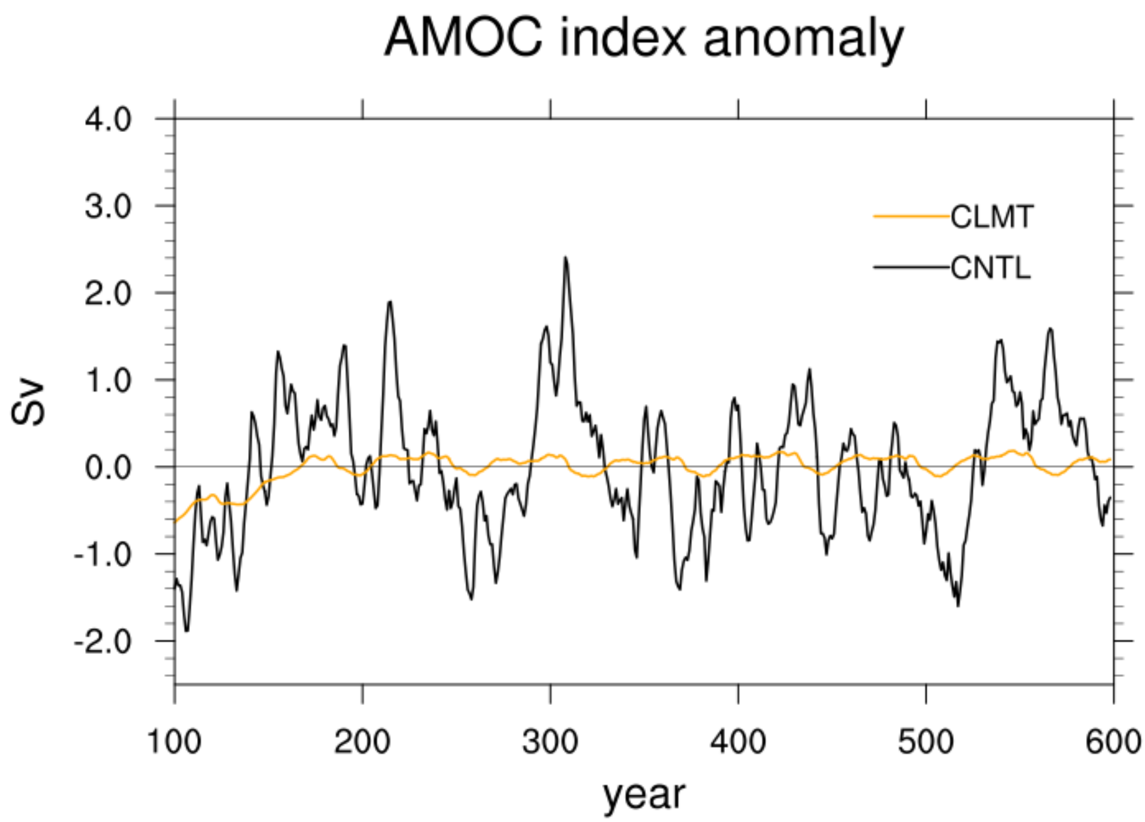

Figure 3.9: AMOC 5-year running mean index over 600 years. Comparison between CNTL and CLMT. Unit is Sv.

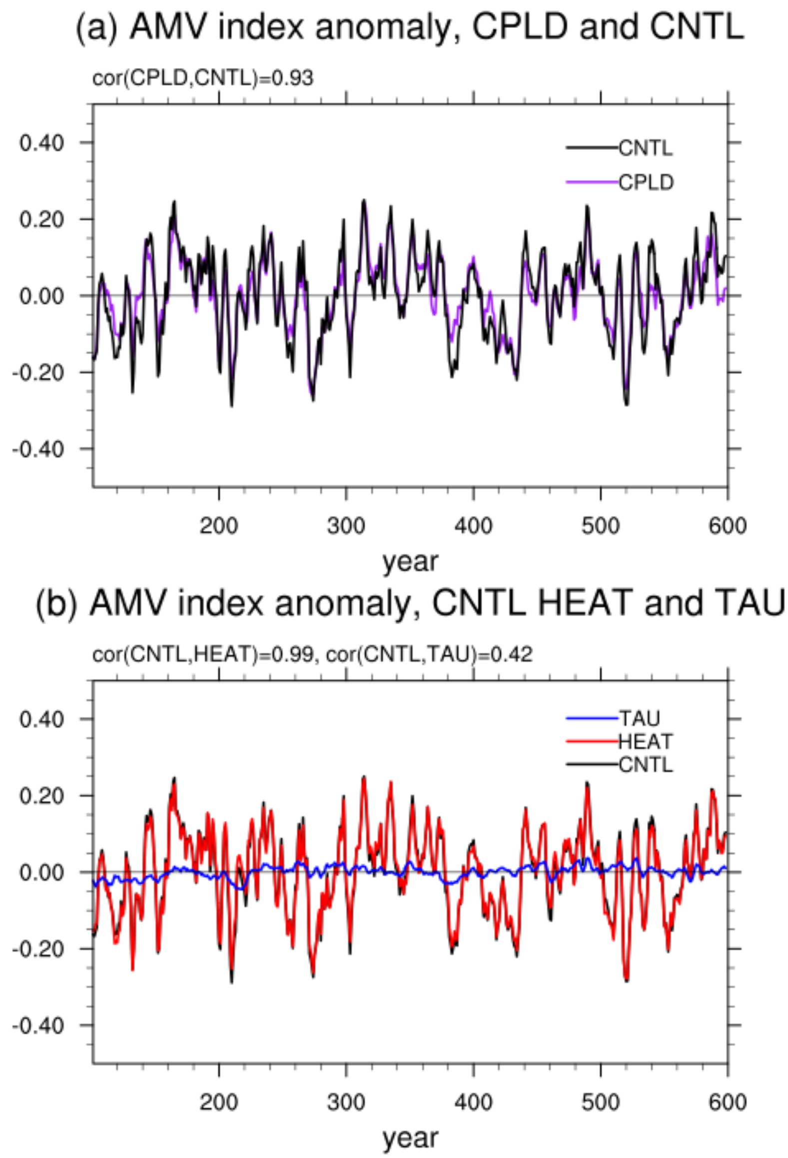

Figure 3.10: Same as Fig. 3.7, but for AMV index anomaly. AMV index is defined as mean SST between 10°N to 60°N in the Atlantic Ocean. Unit is °C. The correlations between different experiments are shown on the top of each panel.

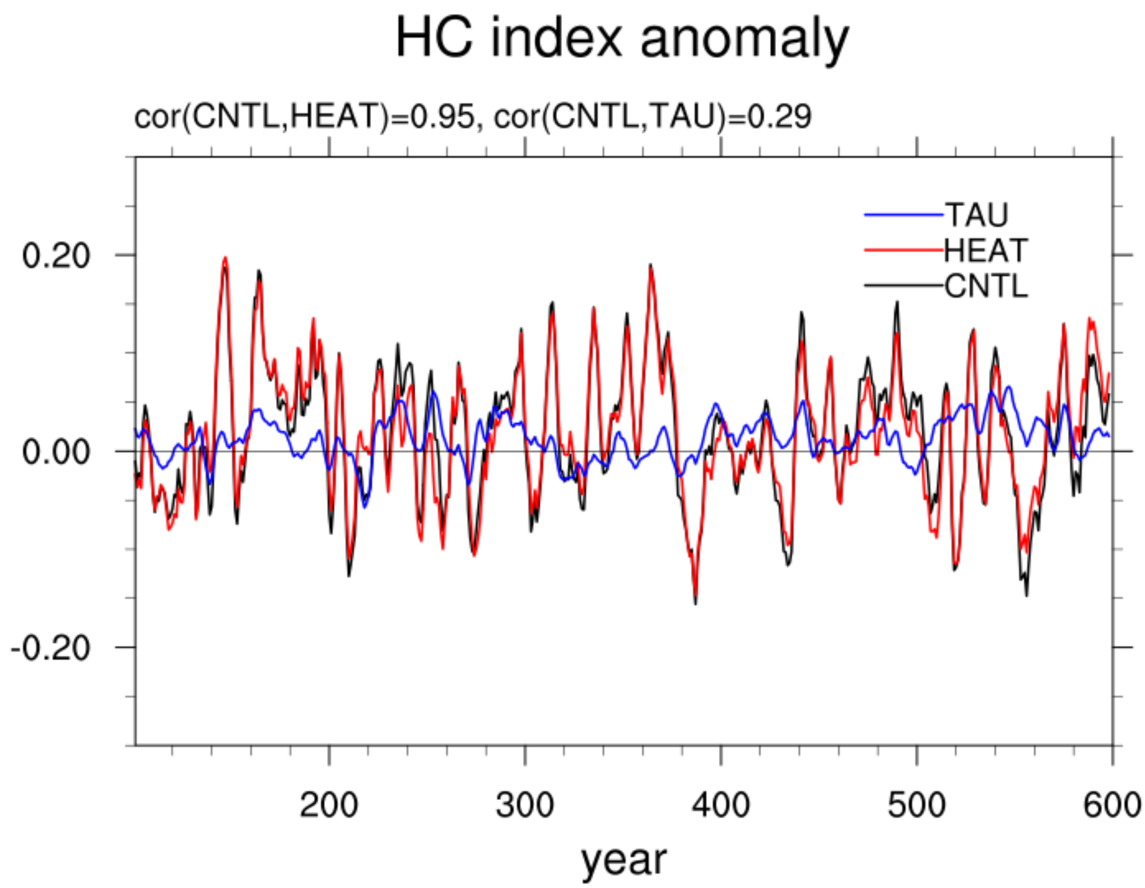

Figure 3.11: Same as Fig. 3.10b, but for HC index anomaly of CNTL (black line), HEAT (red line) and TAU (blue line). HC index is defined as mean HC between 10°N to 60°N in the Atlantic Ocean. Unit is °C. The correlations between different experiments are shown on the top of each panel.

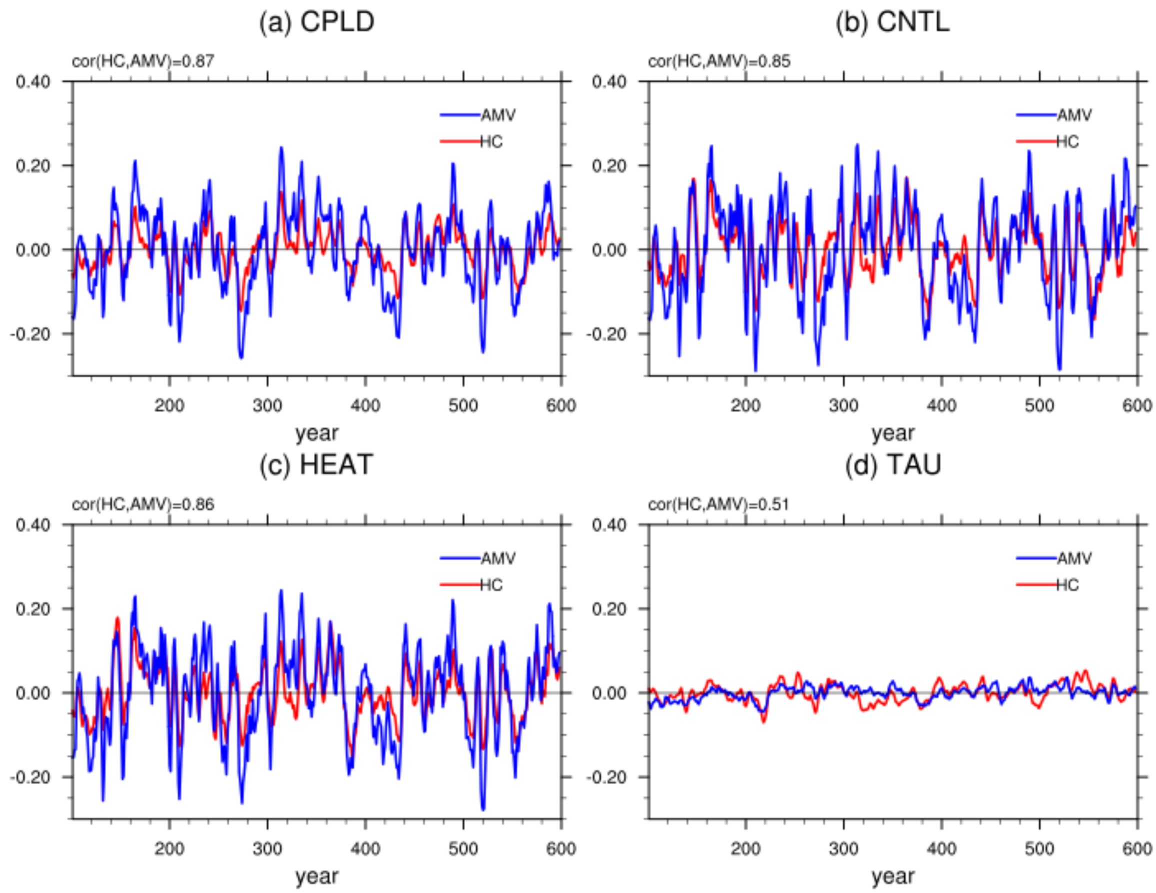

Figure 3.12: Comparison between HC and AMV index over year 101-600 for different experiments. The definition of HC index is the mean HC over the entire northern Atlantic Ocean between 10°N to 60°N. Unit is °C. The correlation between HC and AMV is at the top left corner of each panel.

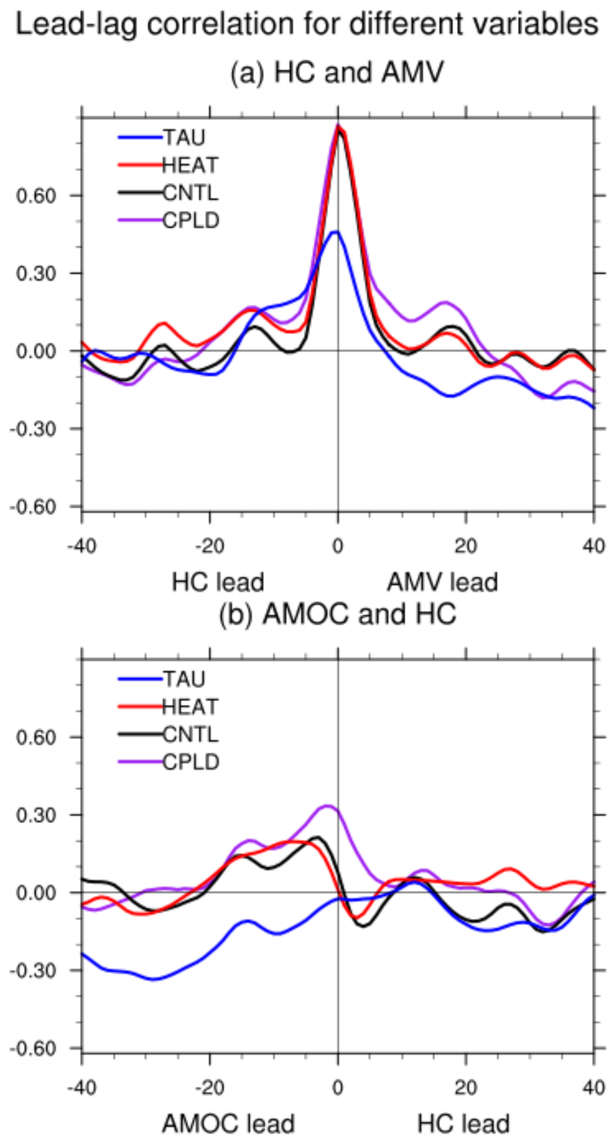

Figure 3.13: Compare the lead-lag correlation between (a) HC and AMV indices, (b) AMOC and HC indices among the four experiments CPLD (purple line) CNTL (black line) HEAT (red line) and TAU (blue line).

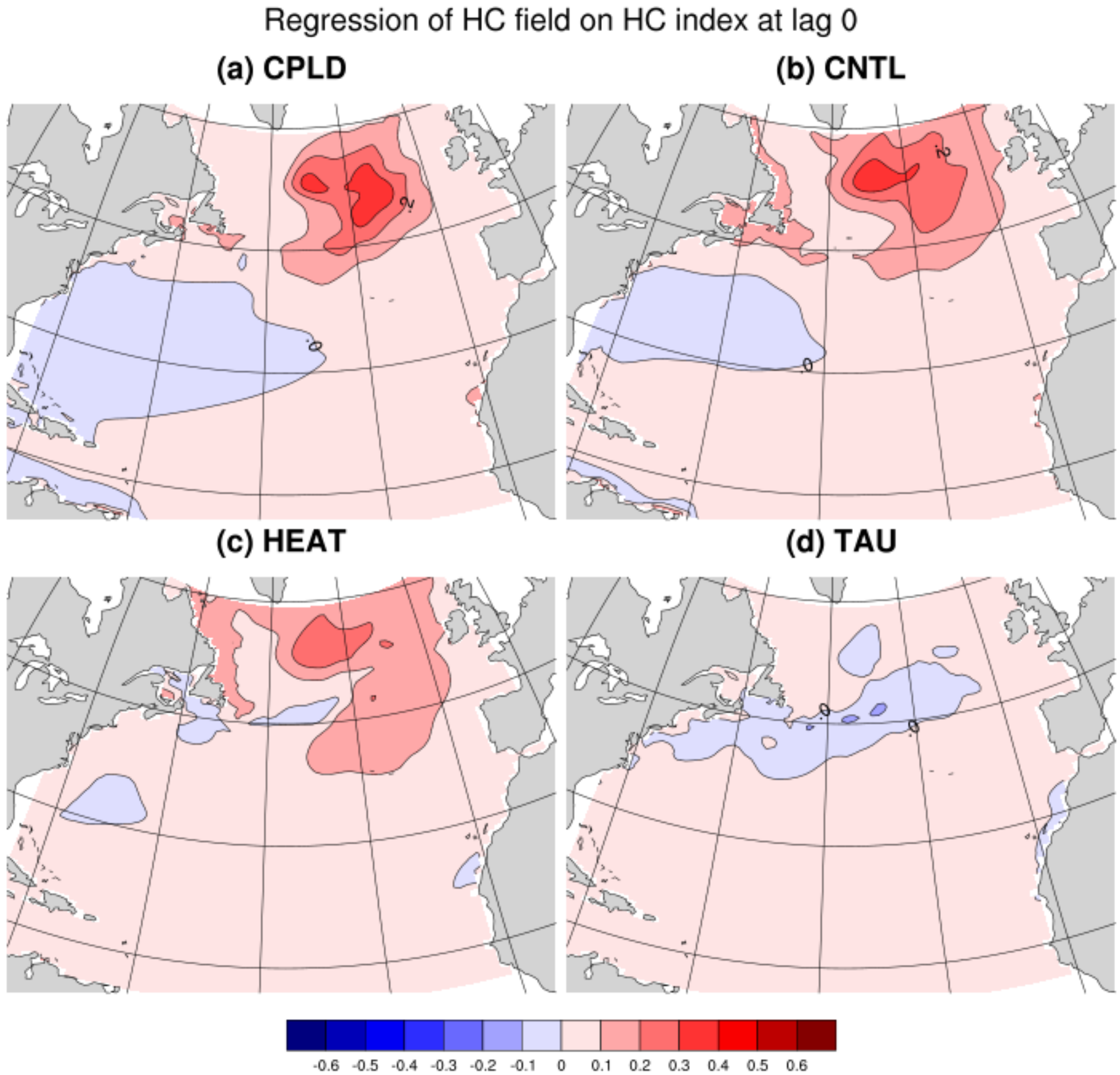

Figure 3.14: The regression of the HC field on the HC index for the four experiments without lags. Unit is °C. Five-year running mean has been applied before taking regression, not only in this figure, but also for all the regression in this paper.

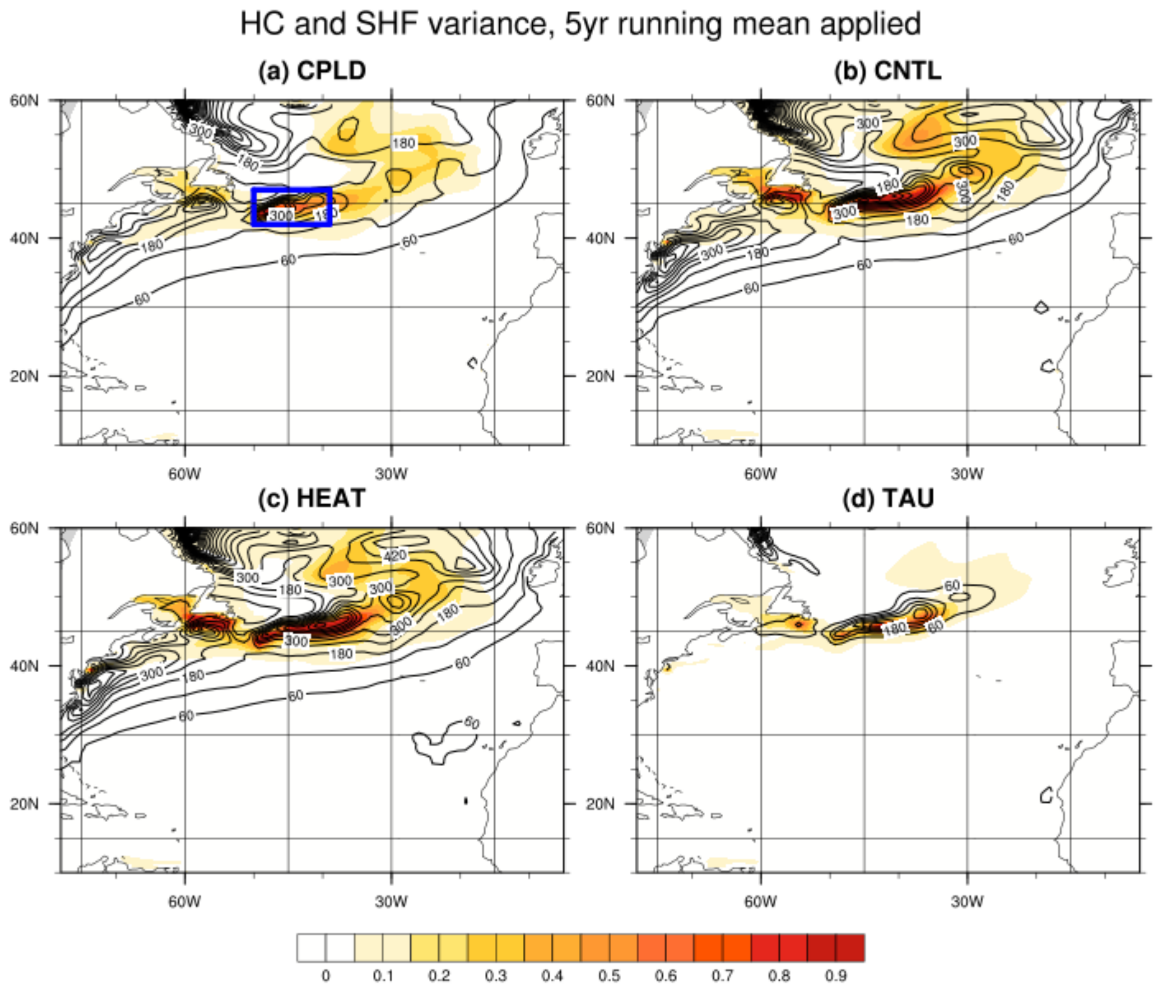

Figure 3.15: Variances of HC (shaded contour, unit is $(^{\circ}\mathrm{C})^2$) and SHF (contour, unit is $\mathrm{W}^2/\mathrm{m}^4$) over year 101-600. Five-year running mean is applied before computing the variance. The blue rectangle in panel (a) shows HCgulf index region (50°W-39°W, 42°N-47°N).

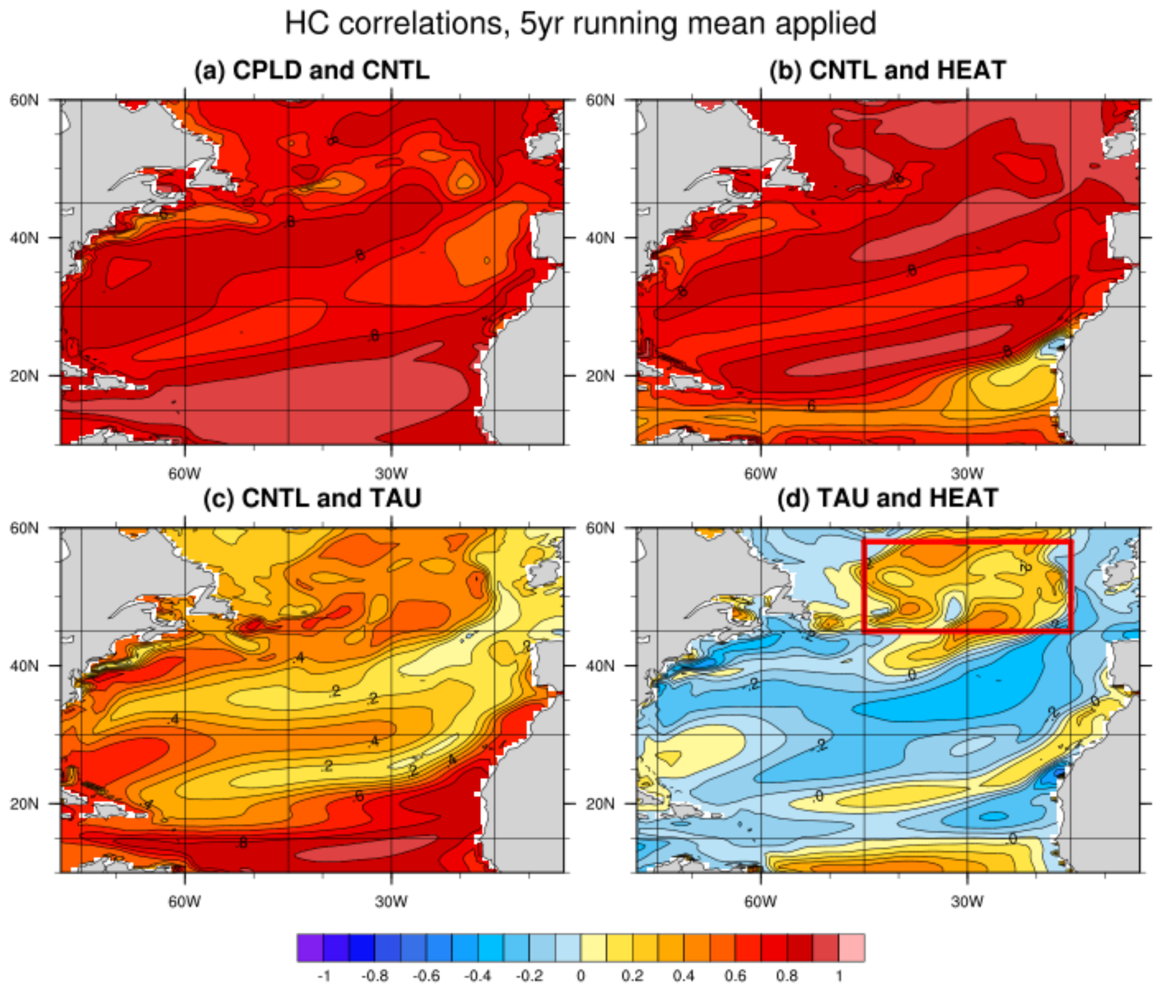

Figure 3.16: HC correlations over year 101-600 between different cases (a) CPLD and CNTL, (b) CNTL and HEAT, (c) CNTL and TAU, and (d) TAU and HEAT. Red rectangle (45°W-15°W, 45°N-58°N) in (d) shows the region for HCnorth index.

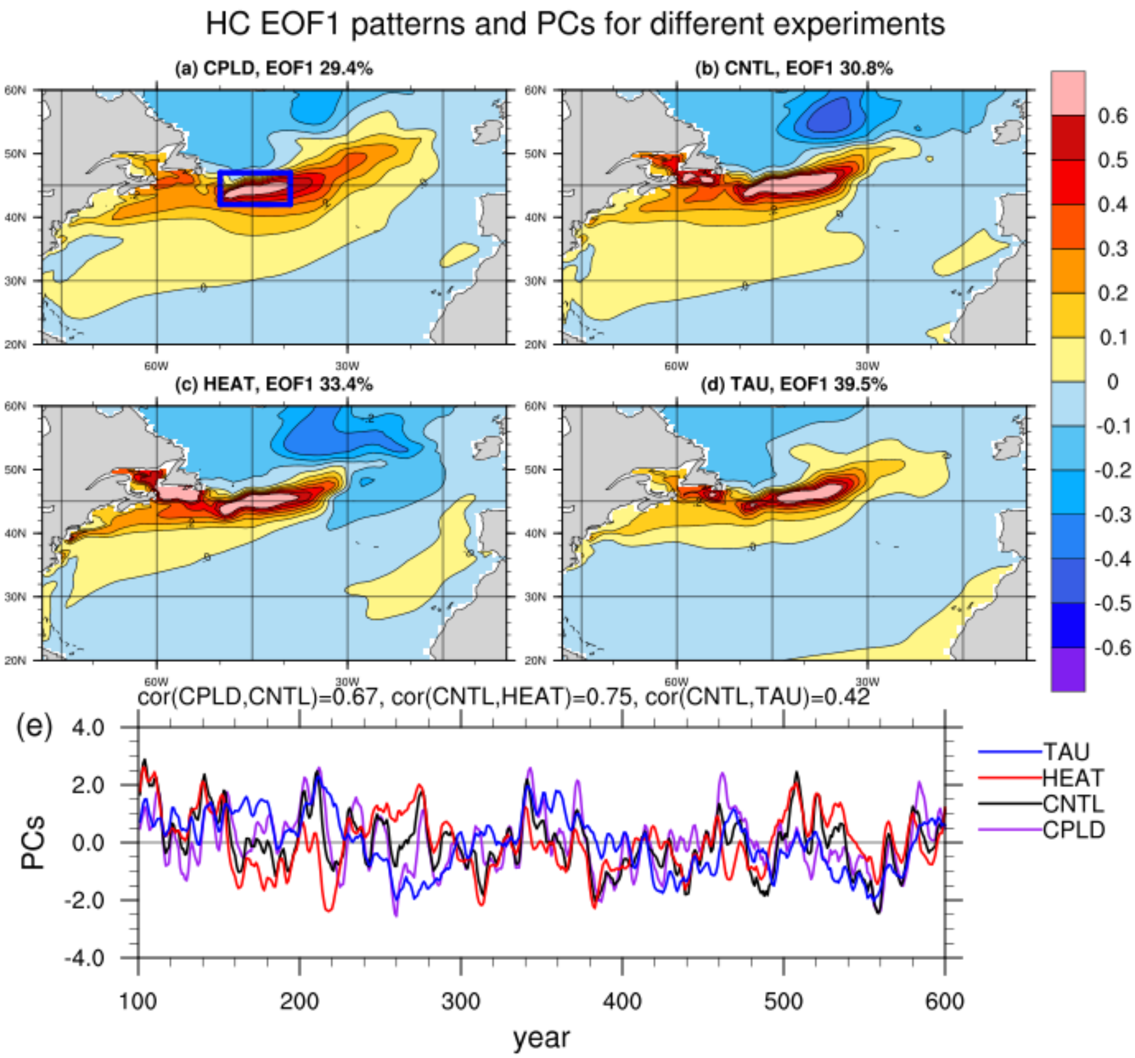

Figure 3.17: (a-d) HC EOF1 patterns and (e) PC1 time series for different experiments over year 101-600 and the correlation between different cases. The correlation between other runs are cor(CPLD,HEAT)=0.16, cor(CPLD,TAU)=0.60, cor(HEAT,TAU)=-0.16. The blue rectangle shows the region for HCgulf (50°W-39°W, 42°N-47°N). Five year running mean applied to the annual HC data before taking EOF.

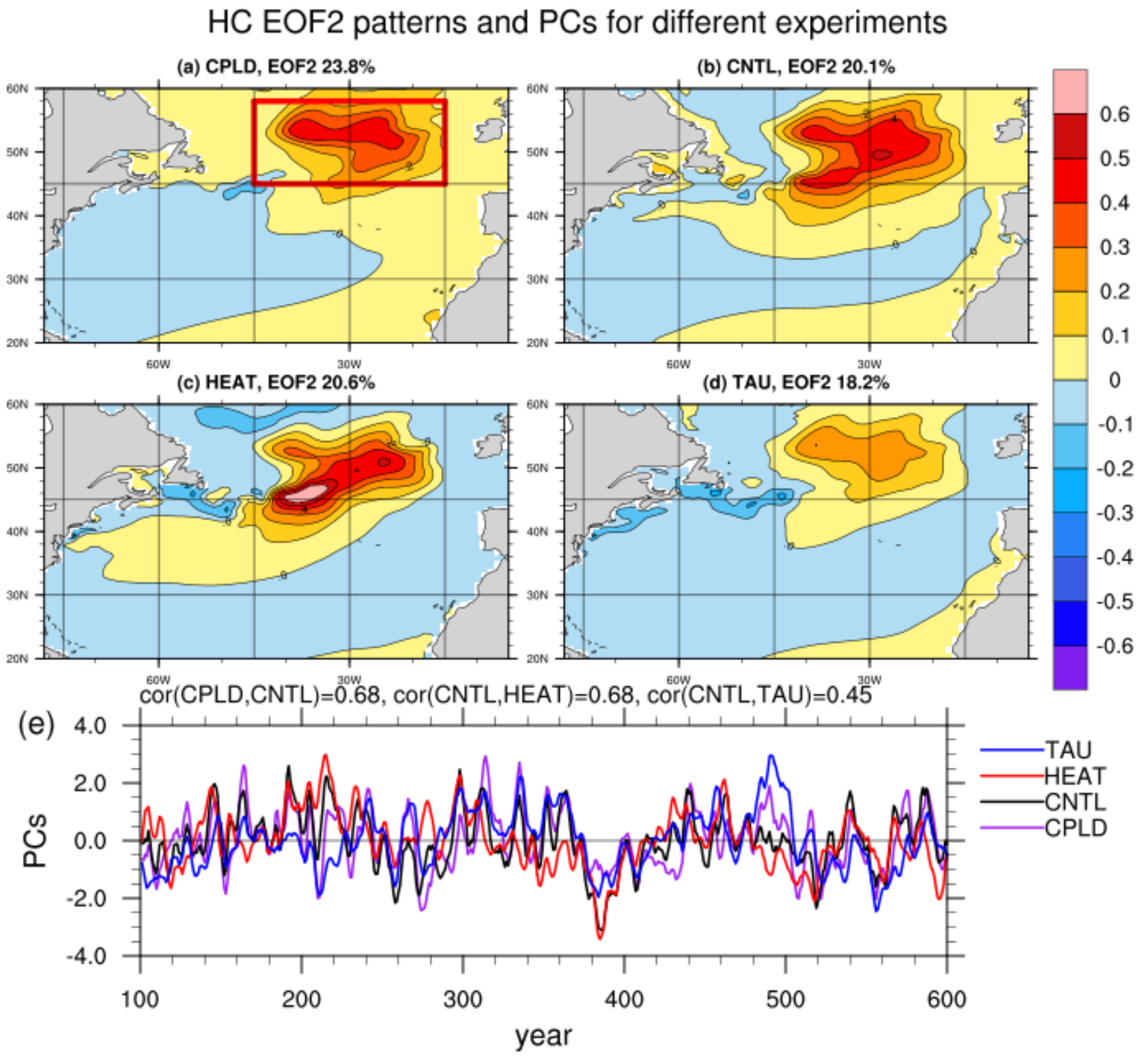

Figure 3.18: Same as Fig. 3.17, but for EOF2. Some of the PC2 correlations are listed on the top of panel (e). The correlation of PC2 for others are cor(CPLD,HEAT)=0.12, cor(CPLD,TAU)=0.64 and cor(HEAT,TAU)=0.07.

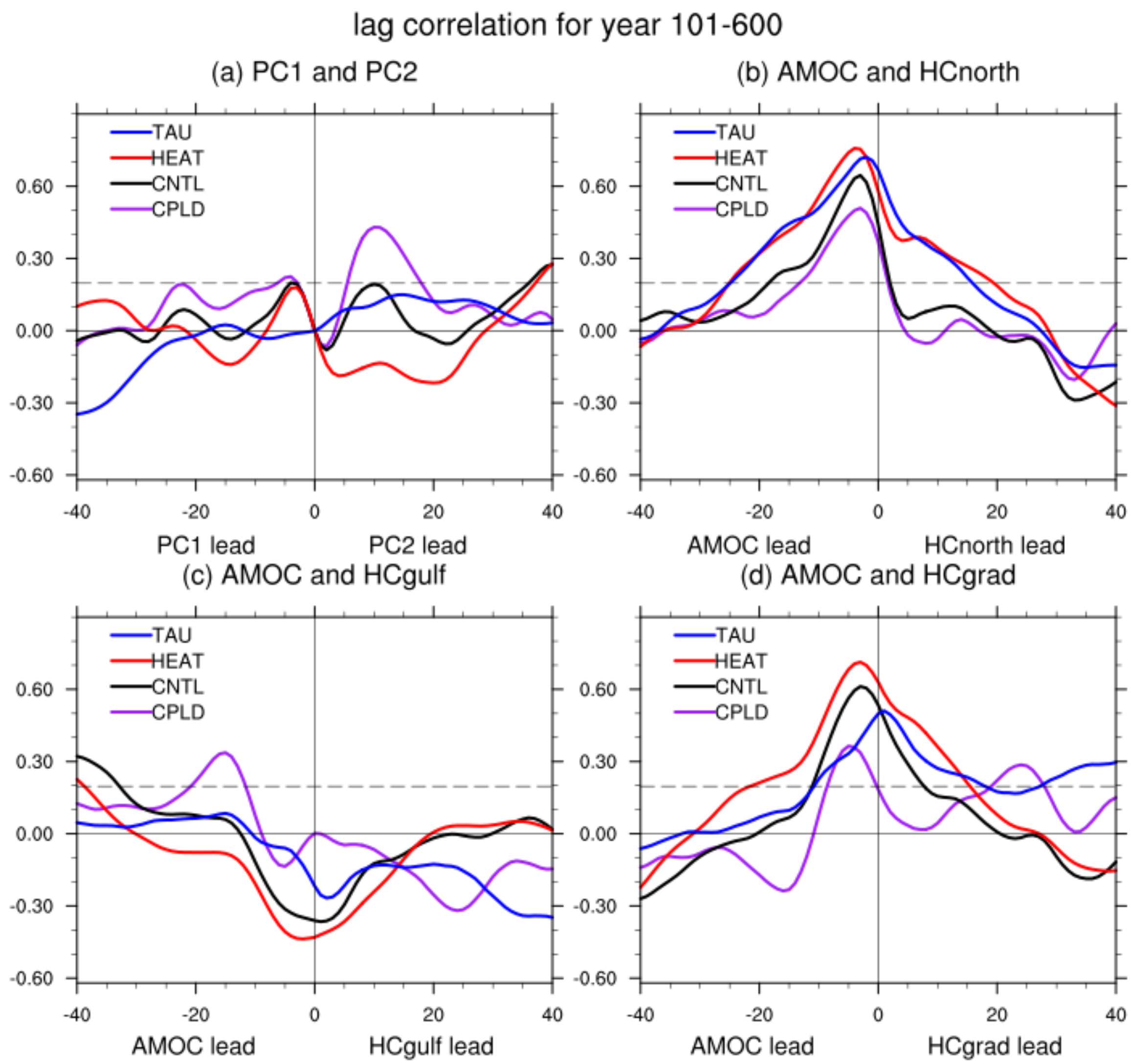

Figure 3.19: Compare the lead-lag correlation between different variables.

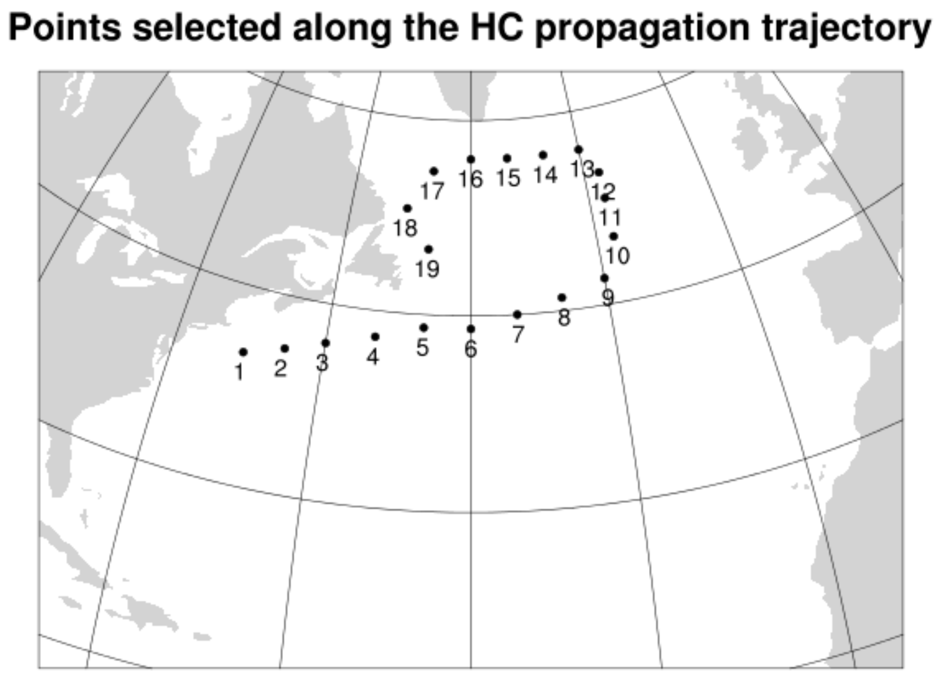

Figure 3.20: Trajectory along subpolar gyre. There are 19 grids selected in total.

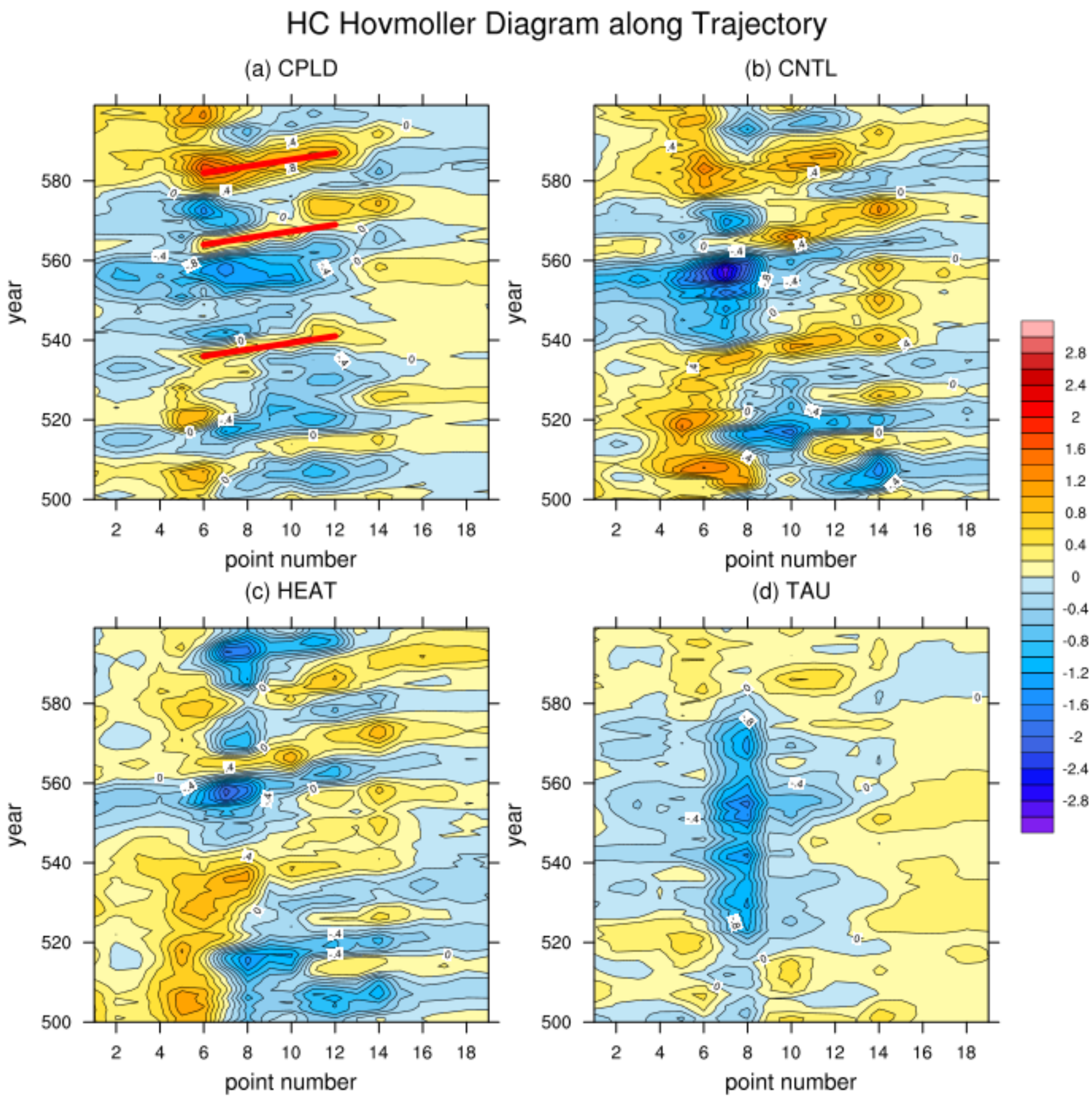

Figure 3.21: Compare the HC propagation along the trajectory during year 500-600. X axis is in the point order marked in Fig. 3.20 from 1 to 19. Y axis is year. Red lines represent propagation direction. HC value is marked by color bar on the right side.

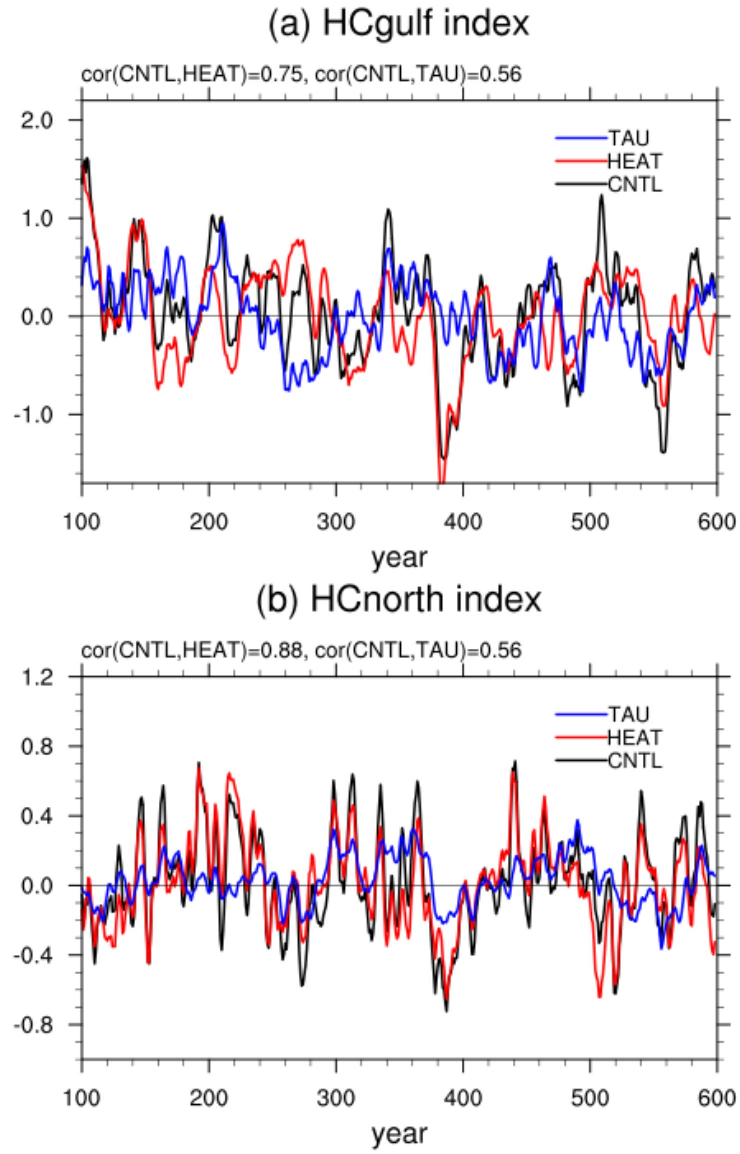

Figure 3.22: Regional mean HC index for TAU, HEAT and CNTL over (a) Gulf Stream region (50°W-39°W, 42°N-47°N), and (b) northern Atlantic Ocean (45°W-15°W, 45°N-58°N). The correlation between different runs is shown on the top of each panel. Note that the range of y axis is different for every panel. Unit is °C for all the indices.

Chapter 4: The impact of surface heat flux anomalies

Many studies have shown that surface heat flux has a significant impact on AMV (DG00, YD14). However, the physical processes of how SHF drives the ocean is unclear. Does heat flux drive HC variations directly by putting heat into/out of ocean, or indirectly by changing currents? Therefore, in this chapter the impacts of surface heat flux anomalies are investigated.

4.1 The lead-lag regression of the HC field on AMOC index

Since we want to investigate the impact of the surface heat flux anomalies, sea water temperature is a valuable variable to look at. However, SST is impacted significantly by the prescribed surface air temperature, whereas HC, the upper ocean heat storage, is not only influenced by the SHF, but also by the oceanic processes, such as advection. In this section, the lead-lag correlation is used to analyze how HC changes with respect to a given pattern or mode of variability, as described in the previous chapter, which can give us a better understanding of the characteristics of the specific HC variation.

The lead-lag regression of the HC field on the AMOC index is calculated and shown in Fig. 4.1 for every 7-year time interval. At lag of -28 years (i.e., the HC anomalies lead the AMOC index for 28 years), there is a weak positive signal in the subpolar gyre region. From lags -21 to 0, that positive signal gets stronger and stronger. In the meanwhile, a negative signal along the GS region shows up and also gets stronger. A dipole mode appears in the Northern Atlantic Ocean. The negative pole is in the GS region and looks similar to the EOF1 pattern. The positive anomaly is located in the subpolar gyre region, expanding all the way to the subtropical region. The northern part of the positive signal looks similar to the EOF2 pattern. The dipole mode gets its maximum at lag 0. According to thermal wind theory, zonal temperature gradient can generate meridional velocity, as shown in Eq. 4.1 (since velocity at the bottom is too small, it is crossed out). Therefore, this HC dipole pattern is in agreement with the maximum northward transportation (or the maximum AMOC). After lag 0, this mode becomes weaker and the positive signal in the subpolar gyre region propagates westward to the western boundary and then goes southward cutting off the negative signal. Similar to Fig. 4.1, the regression of HC field on the AMOC index for CNTL run is also calculated and plotted in Fig. 4.2. Comparing Figs. 4.1 and 4.2, we can find that in general the variation of the HC field with respect to the AMOC index in HEAT is similar to that in CNTL, especially the dipole pattern at lag 0. After so many comparisons between HEAT and CNTL, the HEAT run can reproduce the CNTL run in many respects.

$$V_1 - \cancel{V_2} \sim \frac{\partial T}{\partial x} \tag{4.1}$$

4.2 The heat budget analysis

The above analysis tells us how HC changes. The next question is what causes those changes? What is the role of the SHF? In this section, we will try to answer those questions by using heat budge analysis.

4.2.1 The heat budget equation

Similar to Buckley et al. (2014), to investigate what affects the HC, the heat budget analysis method is used. At first, let us introduce the heat budget equation, which is integrated from depth -D to surface on both sides as follows

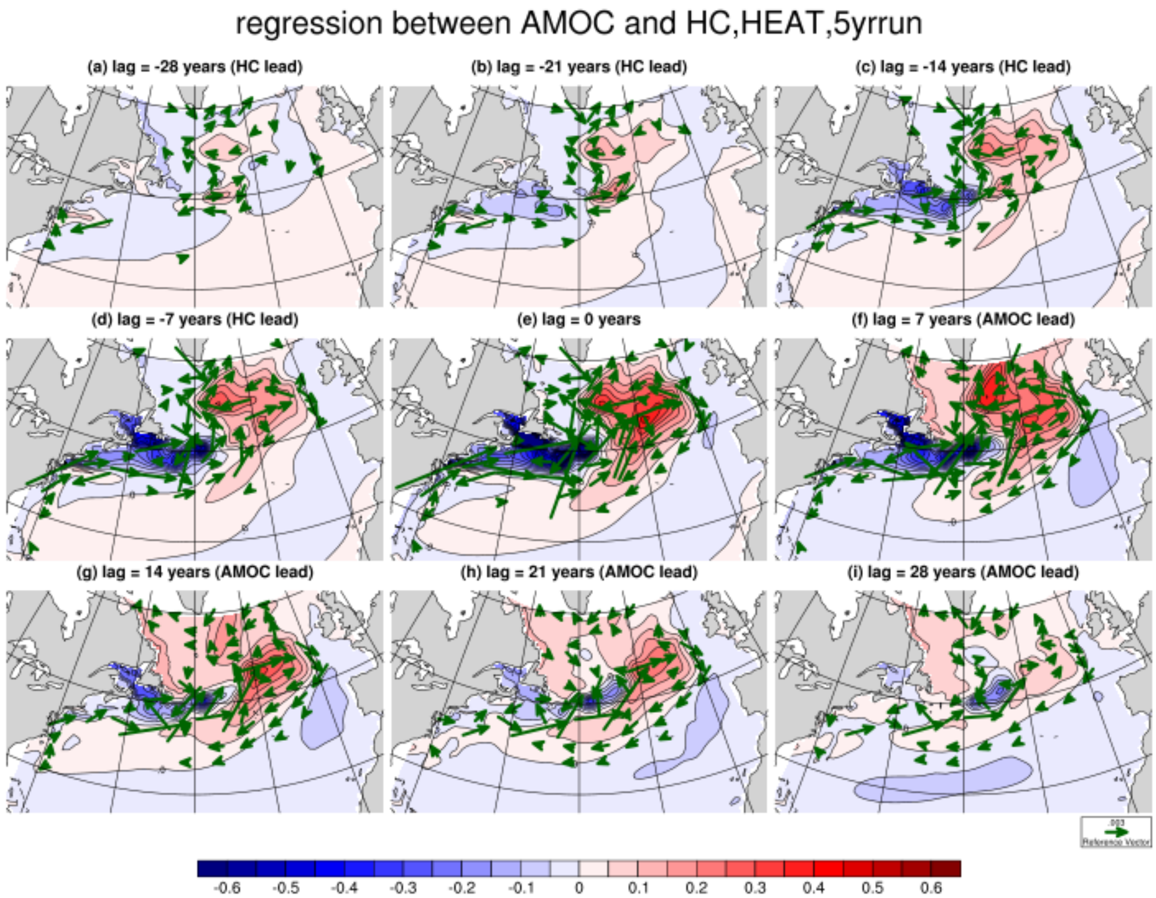

Figure 4.1: Lead-lag regression of HC on AMOC index for HEAT for a seven-year interval. The negative year means HC fields leads AMOC index, and the positive year means AMOC index leads HC field. The unit is °C. The green arrows represent the upper 500 m mean current regression on AMOC index. Unit is m/s. Value less than 0.01 m/s is not shown. For most of the regressions from lag of -28 to 28 years in the following figures, year +/-28, +/-21 are not significant under the 95% significant level.

$$\underbrace{\rho_0 C_p \int_{-D}^{0} \frac{\partial T}{\partial t} dz}_{H_t} = \underbrace{-\rho_0 C_p \int_{-D}^{0} \nabla \cdot (\vec{u}T) dz}_{C_{adv}} \underbrace{-\rho_0 C_p \int_{-D}^{0} \nabla_h \cdot \boldsymbol{K} dz}_{C_{diff\_H}} \underbrace{-\rho_0 C_p \kappa \frac{\partial T}{\partial z}\Big|_{z=-D}}_{C_{diff\_V}} + Q_{net} \qquad (4.2)$$

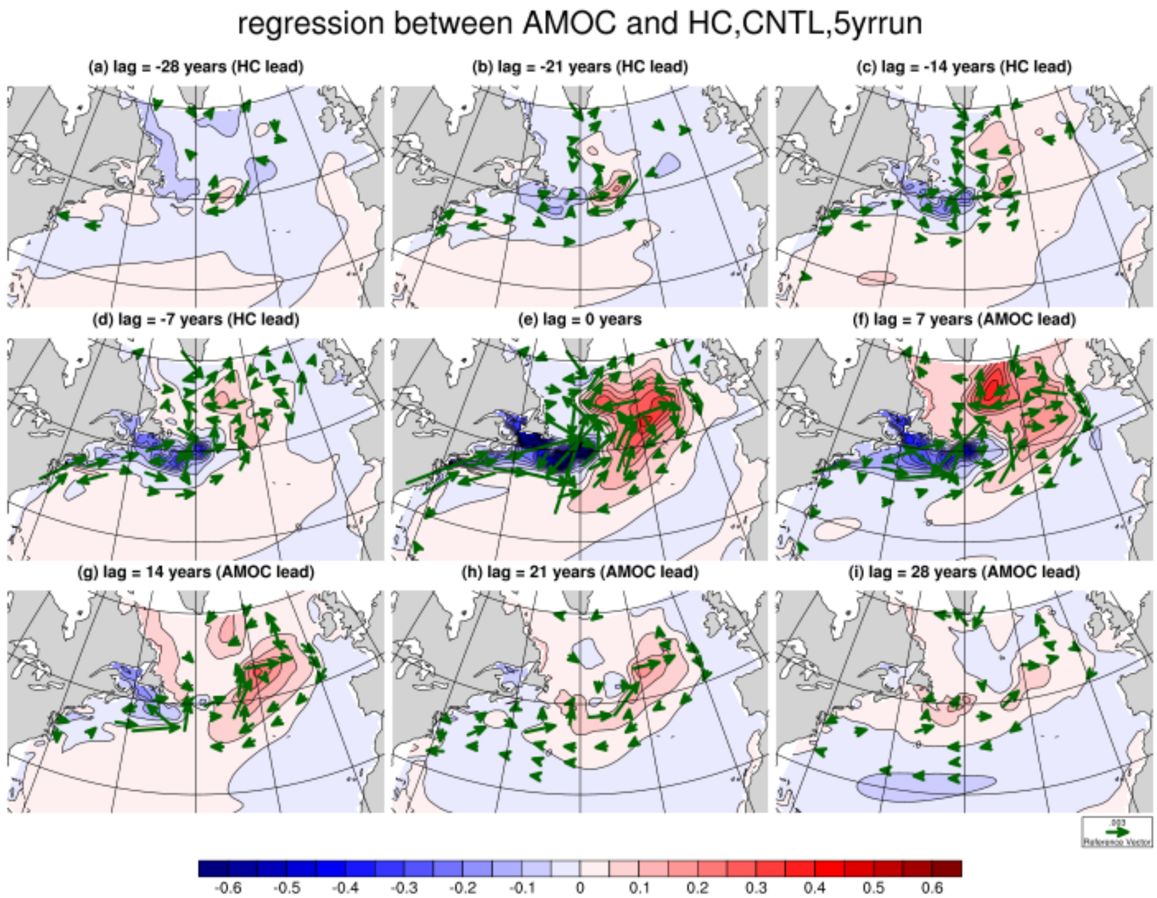

Figure 4.2: Same as Fig. 4.1, but for CNTL run.

where ρ_0 is mean sea water density, C_p is heat capacity, T is temperature, $D = 500$m is the depth (Different from Buckley et al. (2014) using the maximum climatological mixed layer depth (MLD) as D, we fix D at 500 meters), $\vec{u}$ is the three-dimensional velocity, $\boldsymbol{K}$ is the diffusive temperature parameterized by the Gent and Mcwilliams (1990) scheme, which includes along-isopycnal diffusion and advection caused by an additional eddy-induced transport velocity, κ is the vertical diffusivity, and Q_{net} is the net SHF. In POP2, there are three different parameterization schemes for computing the vertical diffusivity κ. In our research, the K-profile parameterization (KPP) is used. More details about KPP can be found in Large et al. (1994).

The term on left-hand side of Eq. 4.2 is the HC tendency (H_t), which is equal to the sum of advection (C_{adv}), horizontal diffusion (C_{diff_H}), vertical diffusion from the bottom at depth -D (C_{diff_V}) and SHF (Q_{net}). Eq. 4.2 can be rewritten in a simple way as

$$H_t = C_{adv} + C_{diff\_H} + C_{diff\_V} + Q_{net} \tag{4.3}$$

The output of each term in the heat budget equation is balanced. Fig. 4.3 shows the results of every term in Eq. 4.3 in a randomly-chosen month. H_t is significant along GS and subpolor region. C_{adv} and C_{diff_H} are significant terms. However, C_{diff_H} has opposite sign to C_{adv}, which means that diffusion term always tries to reduce the H_t caused by C_{adv} and make the temperature distributed evenly. Comparing to C_{diff_H}, C_{diff_V} is very small and negligible. Q_{net} is not as important as C_{diff_H} along the GS, but plays an important role in other regions. The small residual term demonstrates that the equation is balanced. Among the four terms on the right-hand side of the heat budget equation, C_{adv} and Q_{net} are the only two terms generating H_t, whereas the diffusion terms can only reduce tendency and balance C_{adv} and Q_{net}. Therefore, in the following sections, we will focus on C_{adv} and Q_{net}.

4.2.2 The impact of advection

Before examining the advection term, let's see the lead-lag regression of H_t on AMOC index, as shown in Fig. 4.4. This lead-lag regression gives us a clue about the relationship between H_t and AMOC index. At lag of year -28, positive H_t anomalies exist in the North Atlantic Ocean. From lags -21 to 0 (Fig. 4.4b-e), negative anomalies appear in the GS region and grow until lag 0. In the meanwhile, the positive anomalies decrease a little and then reach its maximum at lag 0. After lag 0, the positive anomalies in the northern part

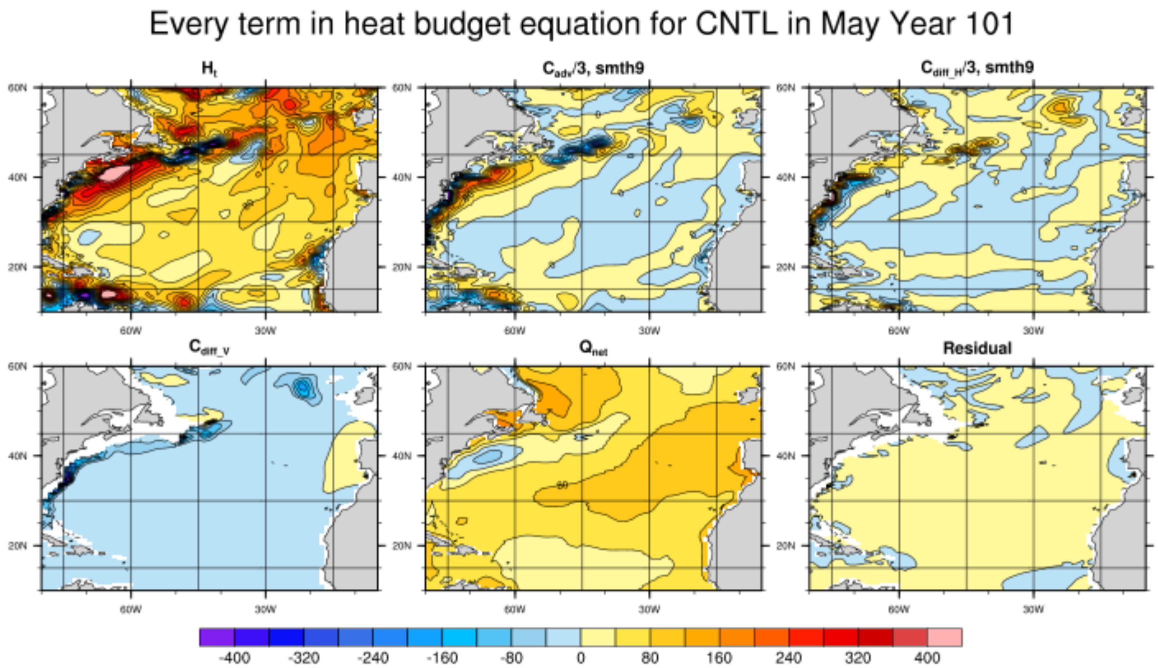

Figure 4.3: Every term in the heat budget equation in model year 101 May, along with the residual term, which is equal to $H_t - (C_{adv} + C_{diff\_H} + C_{diff\_V} + Q_{net})$. Unit for each term is W/m^2. Note that for C_{adv} and C_{diff_H} a scale 3 is divided, as these two terms are way larger than other terms. Nine-point smooth is applied once for these two terms.

of the ocean turn to negative and the negative anomalies in the GS region turn to positive. From lags 14 to 28, the sign roughly remains the same, but the tendency strength becomes weaker. The positive HC tendency in the subpolar gyre means HC will increase in this region (Fig. 4.4a-e), which is consistent with what we have found in Fig. 4.1 during the same period. After lag 0, a north-south dipole mode of tendency (Fig. 4.4f-i) is shown in the North Atlantic Ocean with an opposite sign to the HC anomaly (Fig. 4.1f-i), indicating that the HC dipole mode will decrease. In general, this HC tendency is in line with the HC variation that we have found in the previous section.

Next, let's investigate advection term on the right-hand side of Eq. 4.3. The 3rd-order upwind scheme is used (Leonard 1979) for this calculation. Comparing the third order upwind scheme with the model output in Fig. 4.5, we can find that our own calculation is very close to the model result in almost everywhere except little errors along the western boundary. Also, we can find that there are many smaller scale features in Fig. 4.5. Therefore, in the following analysis, the nine-point local smoothing is performed for four times to smooth out those smaller scale features. Fig. 4.6 shows the regression of C_{adv} on AMOC index. Comparing Figs. 4.4a-e and 4.6a-e, we can find that C_{adv} has the same sign as H_t, which means that C_{adv} dominants H_t during the increasing period of the AMOC, in both the GS region and subpolar gyre region. It can be argued that the HC tendency in the GS region is generated by advection, as current is very strong in that region. However, when it comes to the subpolar region, the current is not as strong, but it can still impact H_t. During the decreasing period (Fig. 4.6f-i), C_{adv} has an opposite sign to H_t, indicating that at this time advection is relatively weak compared with other terms and tendency is determined by other terms.

Previous studies indicate that the advection dominates the HC in the GS region on the interannual (Dong and Kelly 2004; Dong et al. 2007; Buckley et al. 2014, 2015) to decadal time scales (Zhai and Sheldon 2012). Through the model study with a longer time period, we have confirmed the importance of advection term in GS region on the decadal time scales. Moreover, we also found that the advection plays an essential role in the subpolar gyre region on the HC multidecadal variation.

Both the velocity fluctuation and the temperature fluctuation can impact the advection variation. To find out which is the dominant factor, we further decompose the advection term into two terms

$$C'_{adv}(\vec{u}, T) \approx C_{adv}(\overline{\vec{u}}, T') + C_{adv}(\vec{u}', \overline{T}) \tag{4.4}$$

where $C_{adv}(\overline{\vec{u}}, T')$ represents the impact of the temperature fluctuation on the advection, and $C_{adv}(\vec{u}', \overline{T})$ represents the advection generated by the velocity fluctuation. We regress these two terms on the AMOC index and plot in Figs. 4.7 and 4.8, respectively. Term $C_{adv}(\vec{u}', \overline{T})$ (Fig. 4.8) is opposite to $C_{adv}(\overline{\vec{u}}, T')$. Comparing $C_{adv}(\vec{u}, T)$, $C_{adv}(\overline{\vec{u}}, T')$ and $C_{adv}(\vec{u}', \overline{T})$ (Figs. 4.6, 4.7 and 4.8), we conclude that the advection generated by the velocity perturbation is more similar to the total advection in the GS region, and $C_{adv}(\overline{\vec{u}}, T')$ determines the total advection in the northeastern region (around 50°N 20°W).

4.2.3 The impact of surface heat flux

The regression of SHF on the AMOC index in the HEAT run is plotted in Fig. 4.9. At lag of -28 years, the net SHF in the northwest Atlantic Ocean goes into the ocean and leads to positive HC tendency. From lag -21 to 0, HC starts to build up. The role of SHF is damping the HC anomaly. However, the advection still generates positive tendency in the subpolar gyre and negative tendency along the GS. The damping effect of SHF is weaker than the forcing effect of advection. The net effect leads to the growth of the HC anomalies. As a result of larger ocean temperature anomaly, the damping effect of SHF also gets stronger in the HEAT experiment. After lag 0, the SHF is strong enough to determine the net HC tendency. Therefore, we can find that HC tendency has the same sign as the SHF after lag 0. Due to the strong damping effect, HC anomaly gets weaker and weaker.

The combined EOFs of H_t, C_{adv} and SHF further demonstrate that in HEAT run SHF has opposite effect to HC tendency (bottom row in Figs. 4.10 and 4.11). The sign of HC tendency is determined by advection. We also find that experiment CNTL (top row in Figs. 4.10 and 4.11) is very similar to HEAT. For TAU, the weak tendency term is consistent with the small HC index variation in Fig. 3.12d and small HC variance in Fig. 3.15d.

In TAU, as the surface air temperature is prescribed by the monthly climatology, it

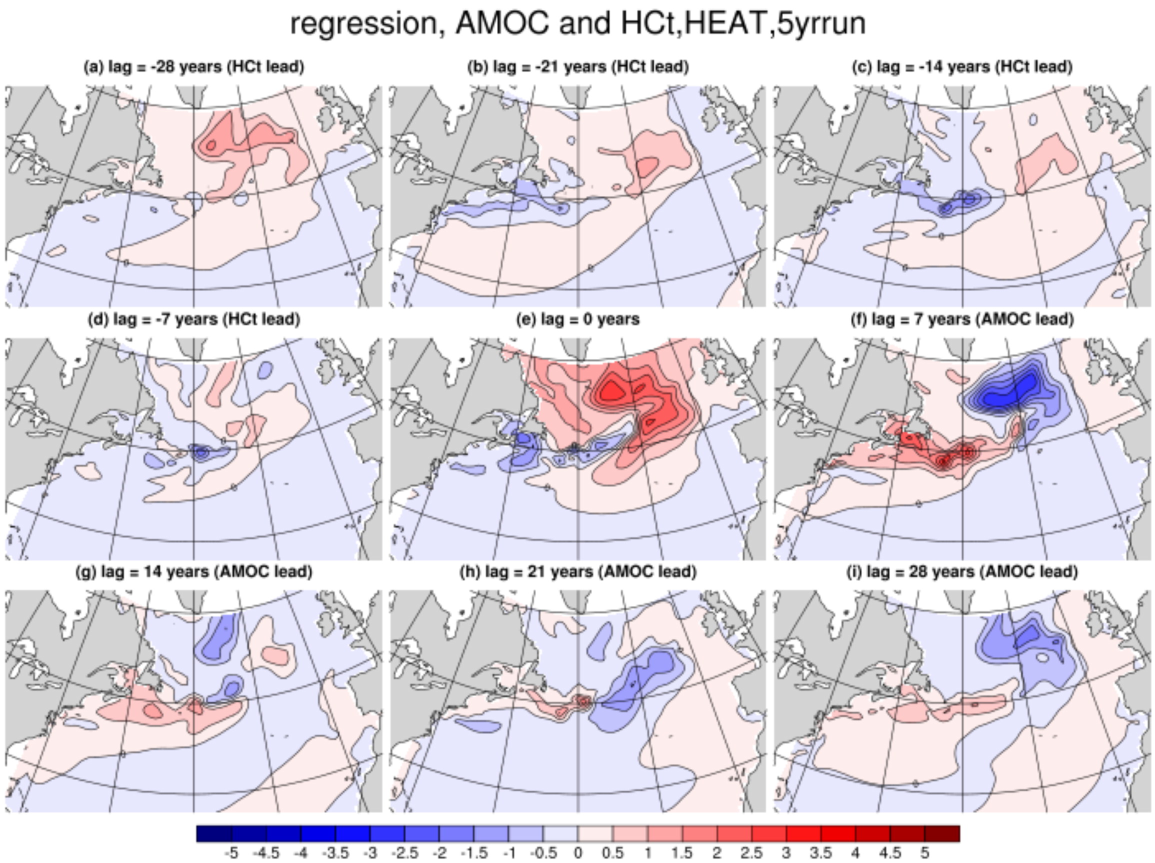

Figure 4.4: Lead-lag regression of H_t on AMOC index for HEAT.

restores the SST towards the climatological state of the boundary condition. The SST will tend to get close to the air temperature. This is consistent with the scenario that the SHF generally damps the ocean temperature anomaly in TAU. However, for HEAT, it is interesting that the role of SHF is still damping when the surface air temperature changes, though at a lesser rate. To find out the relationship between SHF and HC, the damping rate is calculated and plotted in Fig. 4.12. The damping rate is the slope when HC is

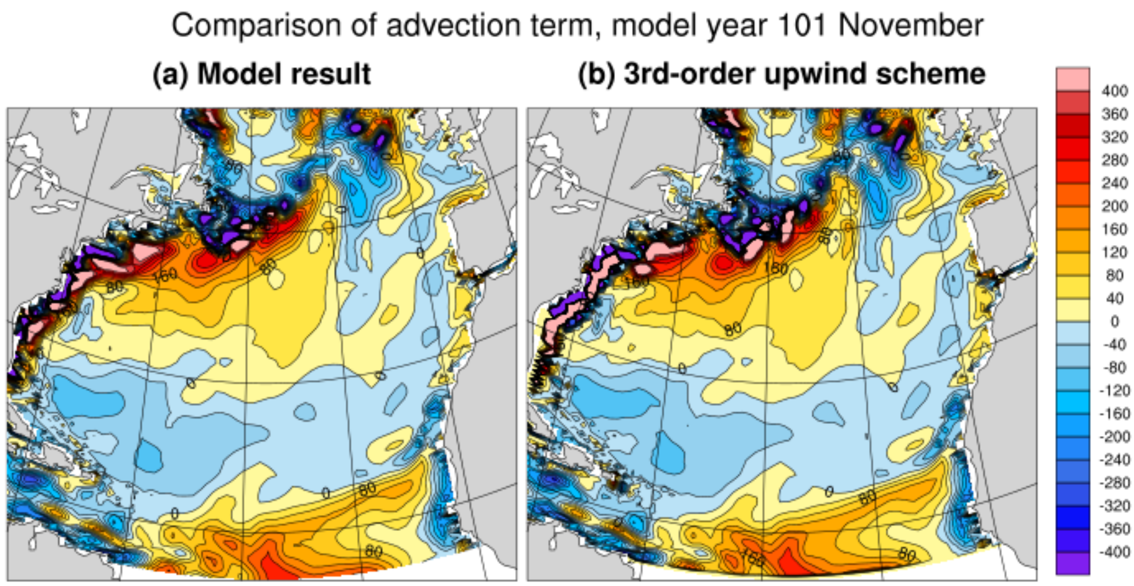

Figure 4.5: Comparison of the monthly mean advection term between (a) the model output and (b) the calculation based on the 3rd-order upwind scheme in a randomly chosen month. Unit is W/m^2.

regressed on SHF, shown as a in the following equation

$$Q_{net}(t) = aHC(t) + b \tag{4.5}$$

where $Q_{net}(t)$ is the time series of SHF, $HC(t)$ is the time series of HC, a is the regression

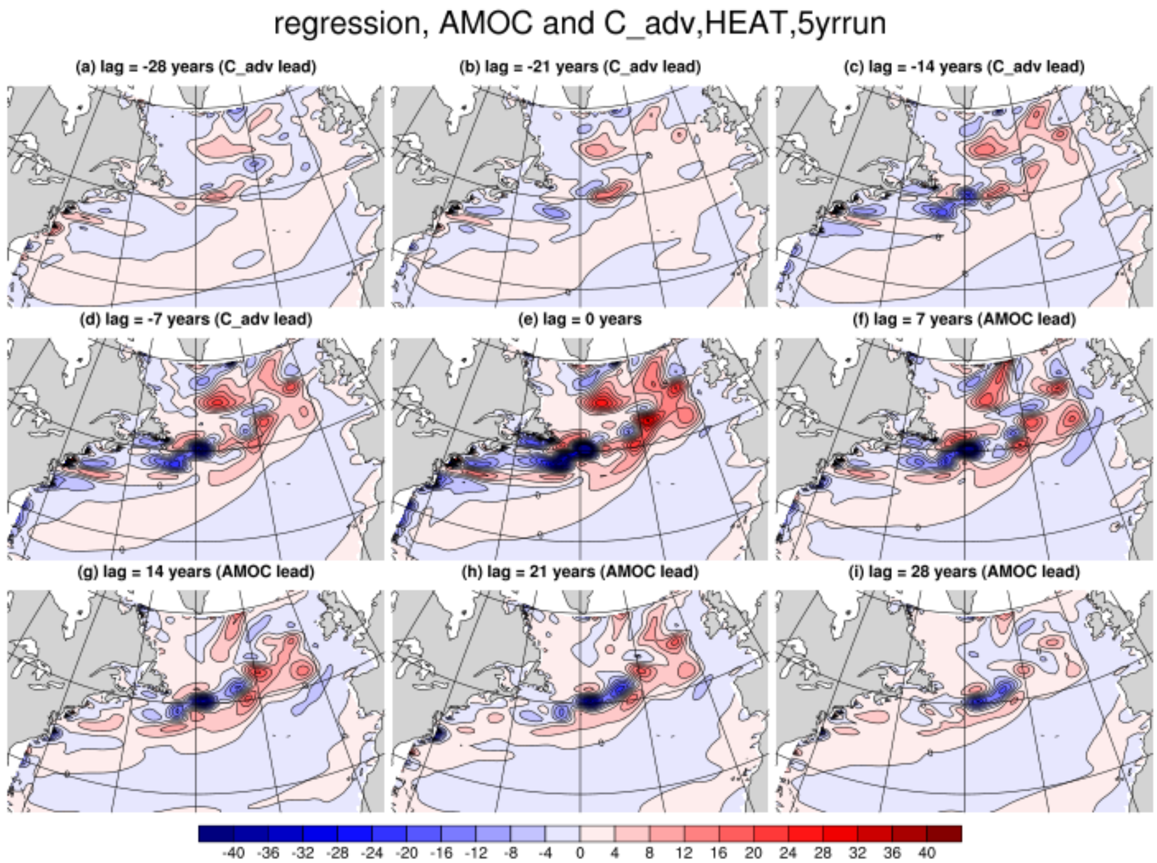

Figure 4.6: Lead-lag regression of C_{adv} (W/m^2) on AMOC index for HEAT. The nine-point local smoothing has been applied for 4 times.

coefficient and b is the residual term and is zero in our case. Using least-square method, the value of a can be determined as the regression coefficient. HC represents the upper ocean temperature storage and the changes of HC can effect SST, which is damped by SHF. The coefficient a can represent the damping rate in some way.

From Fig. 4.12, we find that SHF damps HC in the northern part of the ocean for all

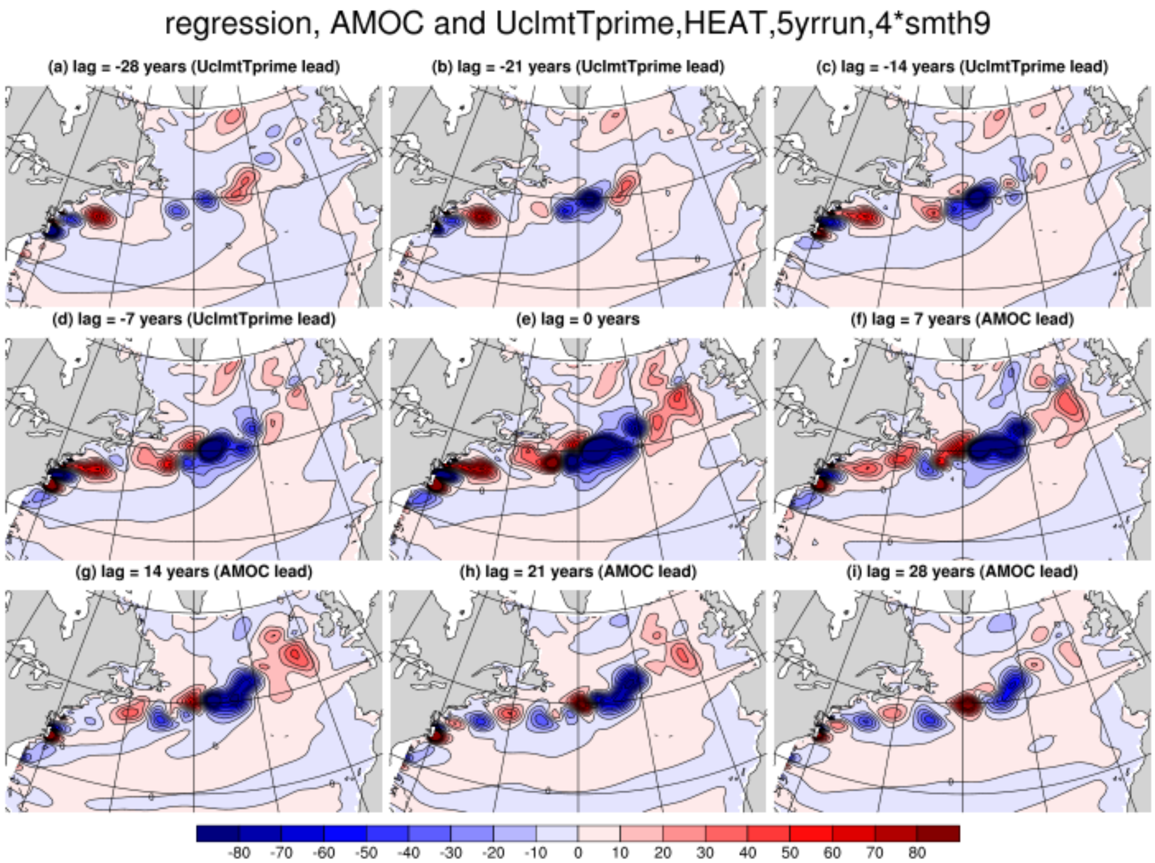

Figure 4.7: Lead-lag regression of $C_{adv}(\overline{\vec{u}}, T')$ on the AMOC index in the HEAT run. The nine-point local smoothing has been done for 4 times. Unit is W/m^2.

four experiments, which is consistent with the combined EOF results. The damping effect of SHF along GS region subpolar gyre region is also in good agreement with previous studies (Dong and Kelly 2004; Dong et al. 2007; Buckley et al. 2014, 2015; Buckley and Marshall 2016). However, the damping effect of SHF in TAU is stronger than other runs. It means that in TAU when HC leaves GS region and moves further north, it will be damped faster.

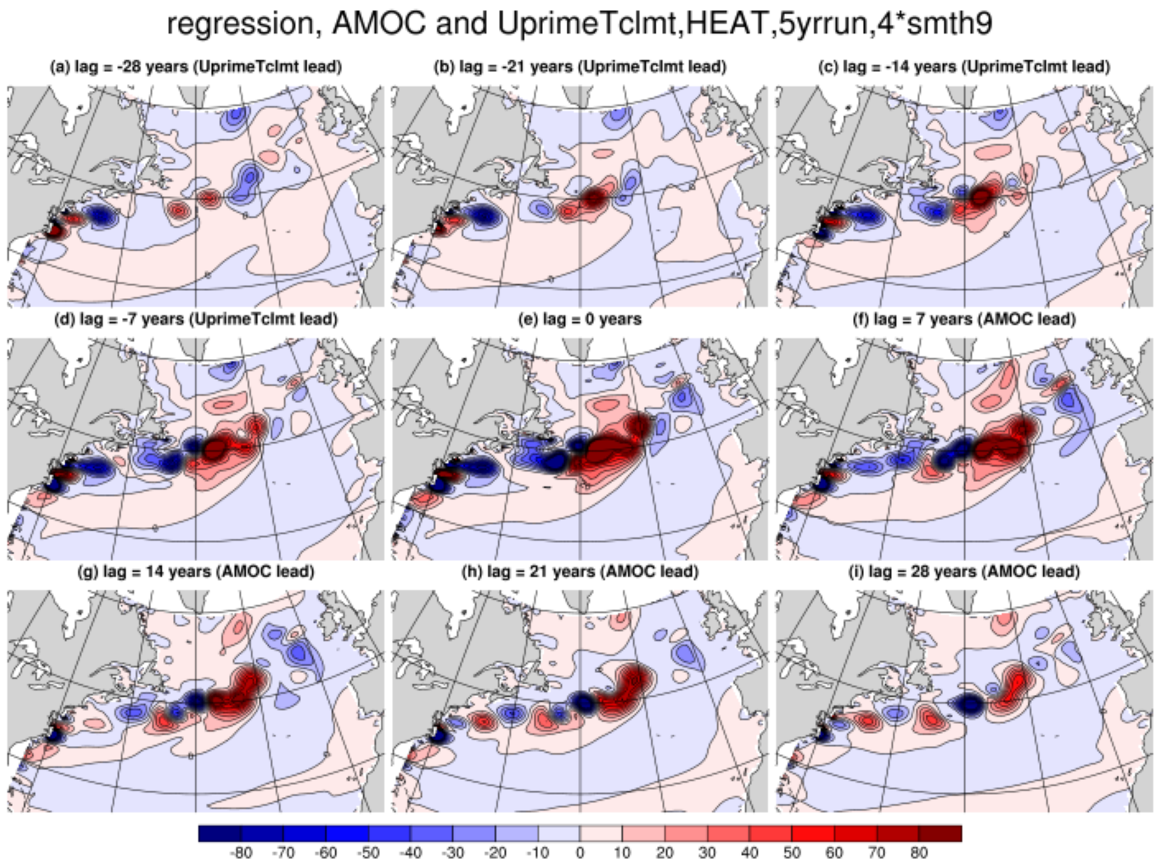

Figure 4.8: Lead-lag regression of $C_{adv}(\vec{u}', \overline{T})$ on the AMOC index in the HEAT run. The nine-point local smoothing has been done for 4 times. Unit is W/m^2.

This explains why in the TAU run the HC variance and the EOF loading in the subpolar gyre region is so weak compared with the others, because the HC is damped out by SHF. In the TAU run, besides the north, SHF also acts as a damping factor in the subtropical region. This is the result of restoring boundary condition of TAU. For CPLD, CNTL and especially for HEAT, there is a strong heat flux input in the western subtropical gyre along the coast. We are not clear about how this heat flux input can affect the HC variation in the subpolar gyre. One thought is that, when the positive net surface heat flux anomalies increase, the water gets warmed up here and the warm anomalies propagate along the GS and subpolar gyre into the north. However, no significant signals in this region have been found in the regression maps and the EOF analysis. Maybe the SHF input is significant, but the variance is too small compared to the northern part. Therefore, it is not visible in the variance, regression and EOF analysis.

We also need to point out that the damping effect of SHF only occurs in the long-term variability. For the short-term fluctuations with period less than 5 years, shown in Figs. 4.13 and 4.14, the same sign of tendency and SHF over the northern Atlantic Ocean demonstrates that SHF is a forcing factor of the heat content tendency for the CNTL and HEAT runs. The SHF has the same magnitude as C_{adv} and significant impact on H_t over the subpolar gyre region. As for TAU, Q_{net} is a weak damping factor and advection is the dominant term. For all three runs, the advection still has strong influence for tendency along GS for the short-term variability.

4.3 Summary

We examine the evolution of heat content (HC) over multidecadal time scales by regressing the HC field on the AMOC index. The lead-lag regression shows a clear development process. A dipole of warm anomaly in the subpolar gyre and cold anomaly in the Gulf Stream region (GS) strengthens from lag -28 years to lag 0 and then weakens (Fig. 4.1). The dipole is consistent with the sum of EOF1 and EOF2 patterns. The positive anomaly propagates to the western boundary and then goes southward cutting of the negative anomaly.

A heat budget equation diagnoses the dynamics of the HC variation. The heat budget equation equates heat content tendency (H_t) to the sum of advection (C_{adv}), diffusion (C_{diff_H}, C_{diff_V}) and surface heat flux (Q_{net}). The H_t regression on AMOC index is consistent with the increase and decrease in the HC dipole. Examining the regressions for

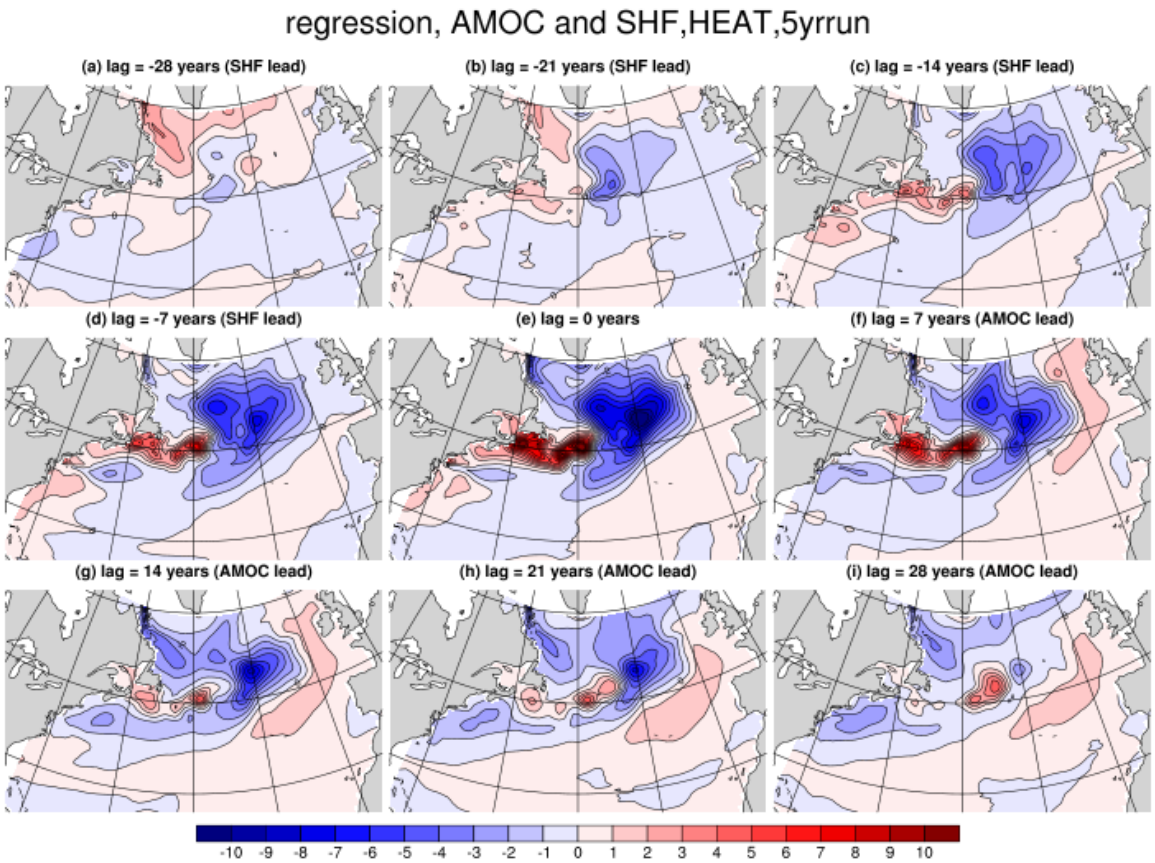

Figure 4.9: Lead-lag regression of SHF (W/m^2) on AMOC index for HEAT. Positive SHF anomaly means heat flux goes into the ocean. Negative SHF anomaly means losing heat flux.

individual terms, we find that advection determines the tendency during the HC strengthening, whereas SHF dominants the tendency during weakening. We also find that the advection generated by the velocity perturbation is dominant to the total advection in the GS region, and the mean velocity field transporting the temperature anomalies determines the total advection in the northeastern region. The combined EOF of H_t, C_{adv} and Q_{net} also

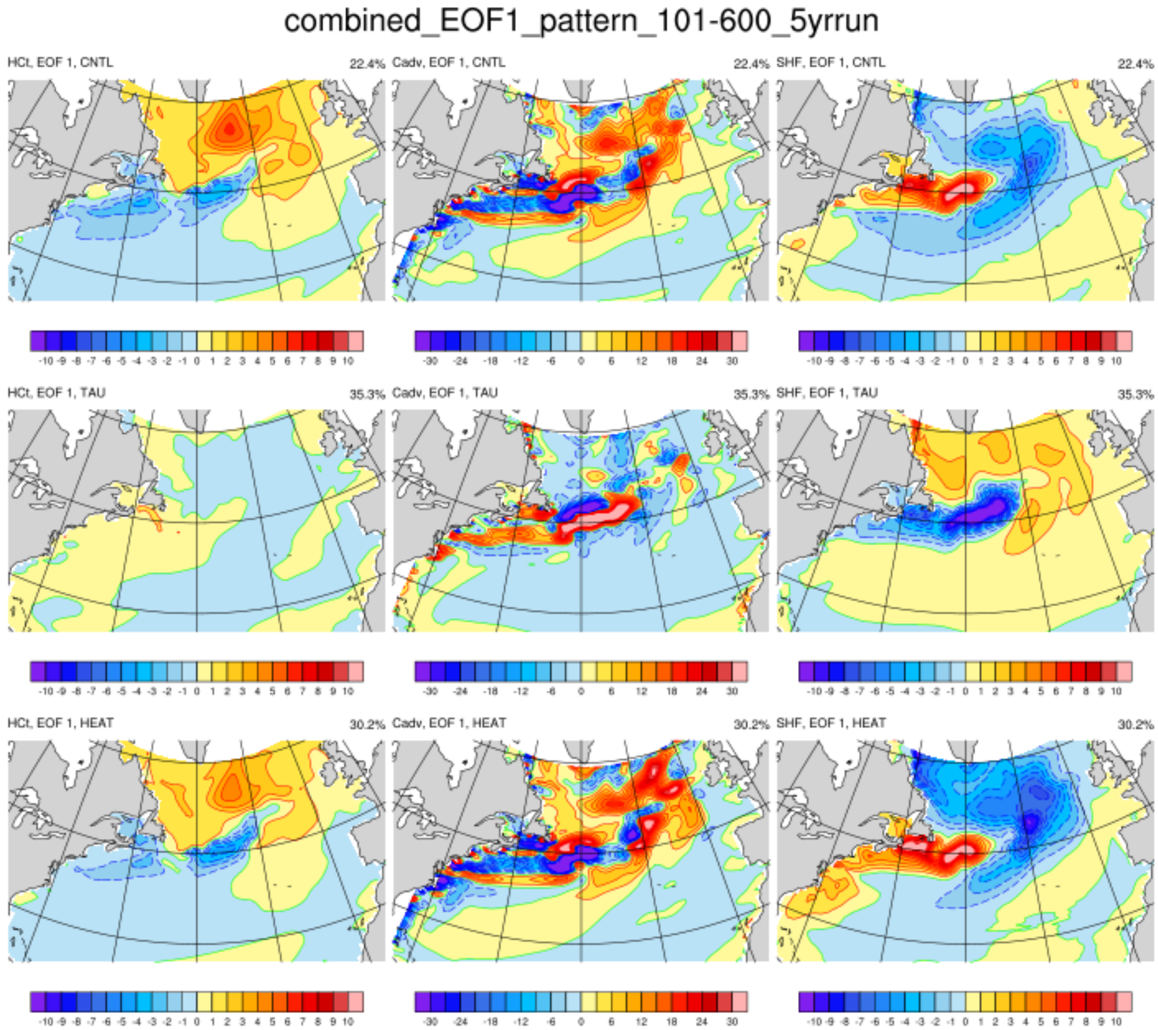

Figure 4.10: Combined EOF1 of H_t, C_{adv} and SHF for CNTL, TAU and HEAT, respectively. Variable name and case name are shown on the top left corner of each panel. Variance explained is shown on the top right corner. Five-year running means has been performed before taking EOF. Nine-point smoothing has been applied for EOF pattern of advection twice.

demonstrates a similar conclusion, with local SHF playing a damping role for the existing temperature anomalies in the Northern Atlantic Ocean on multidecadal time scales.

We find that in the subpolar gyre region the damping effect of SHF in TAU is stronger than all the other runs. This explains why in TAU run the HC variation in the subpolar

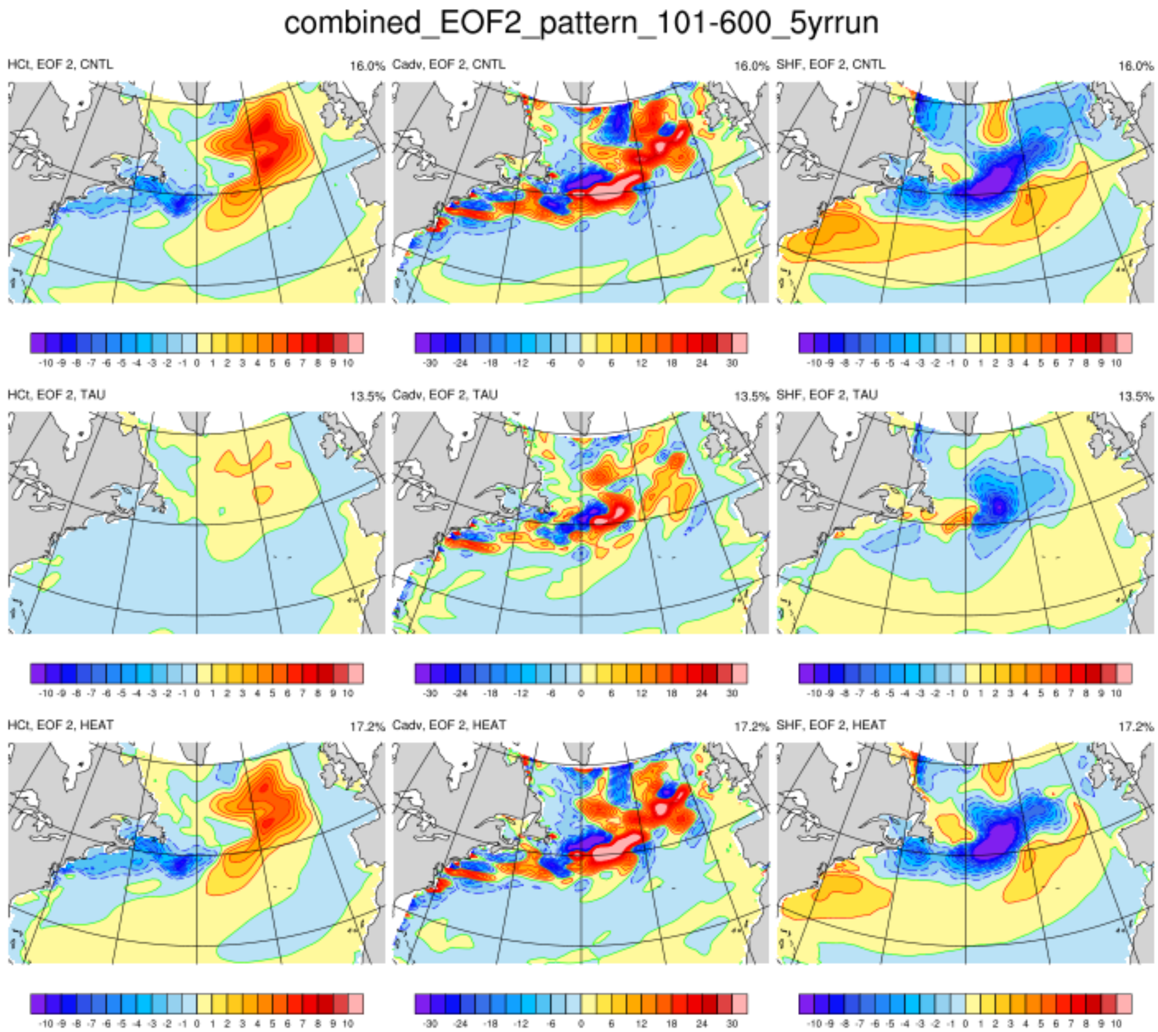

Figure 4.11: Same as Fig. 4.10, but for EOF2

region is very small. Also note that the local SHF plays a damping role only for the long-term variation and it only damps the existing temperature anomalies generated by advection. When it comes to short-term fluctuations with periods less than 5 years, SHF is a forcing factor same as the advection.

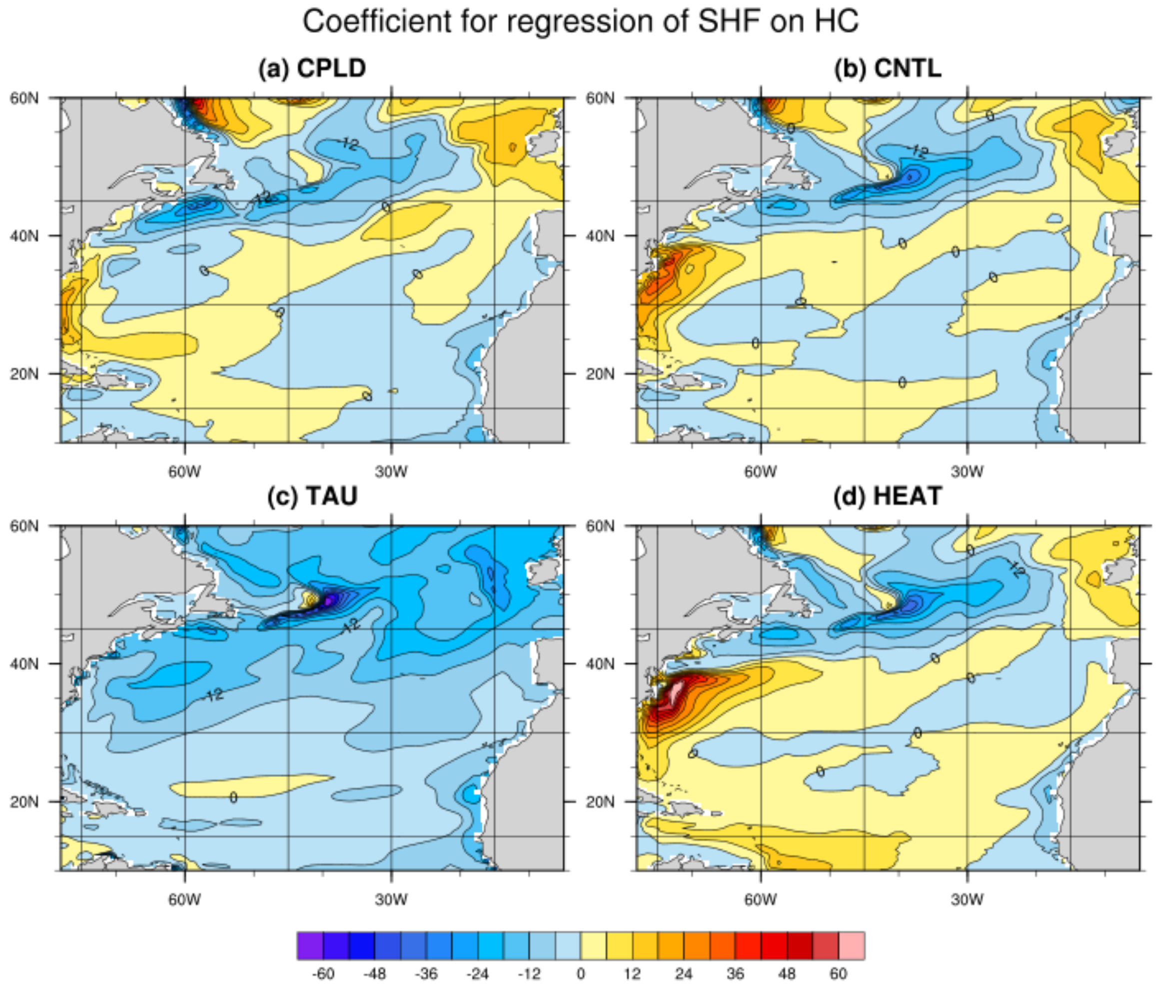

Figure 4.12: Regression coefficient (W/(m^2·°C)) between SHF and HC for different experiments.

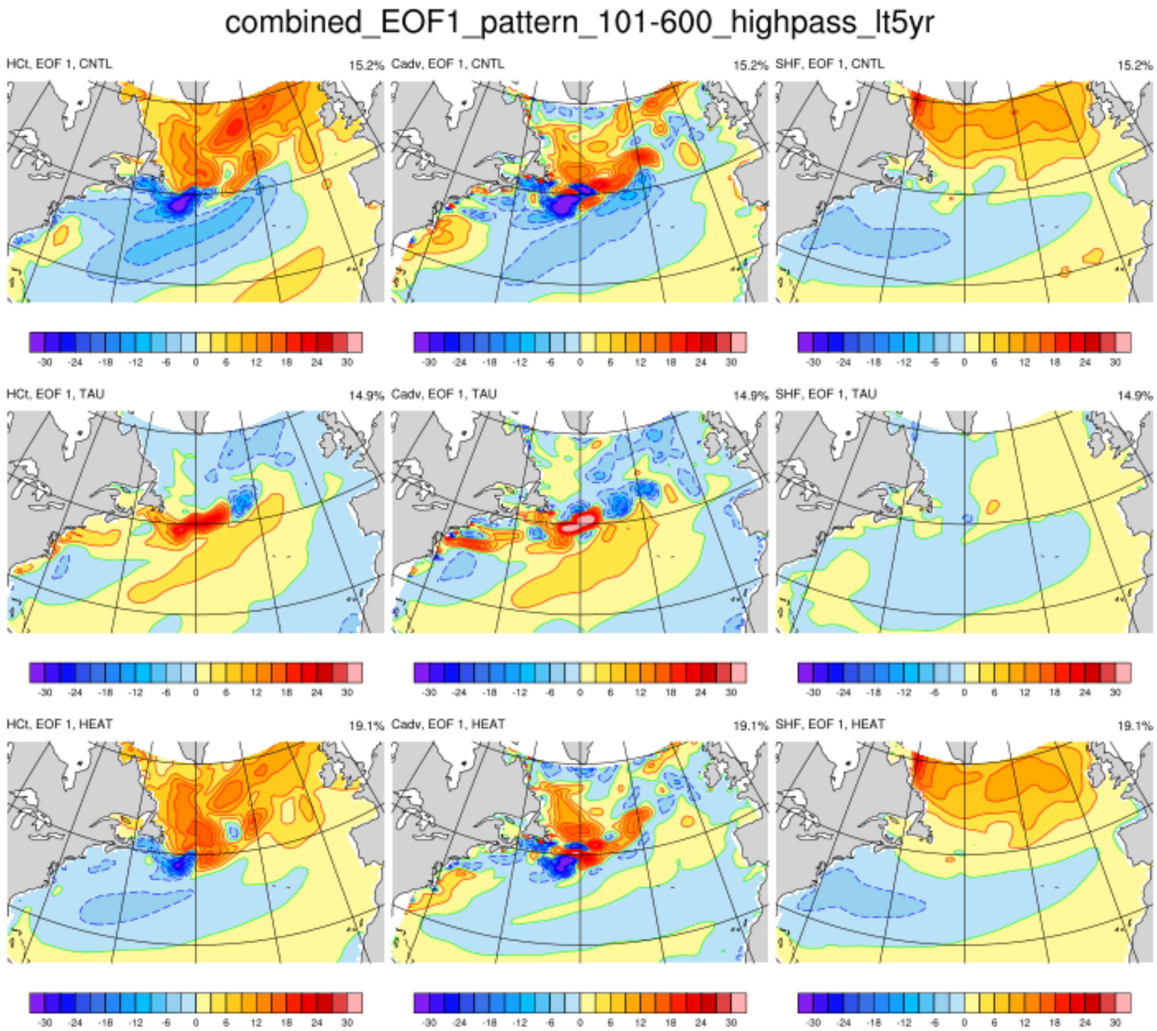

Figure 4.13: Same as Fig. 4.10, but no five-year running mean and five-year highpass is applied before taking EOF.

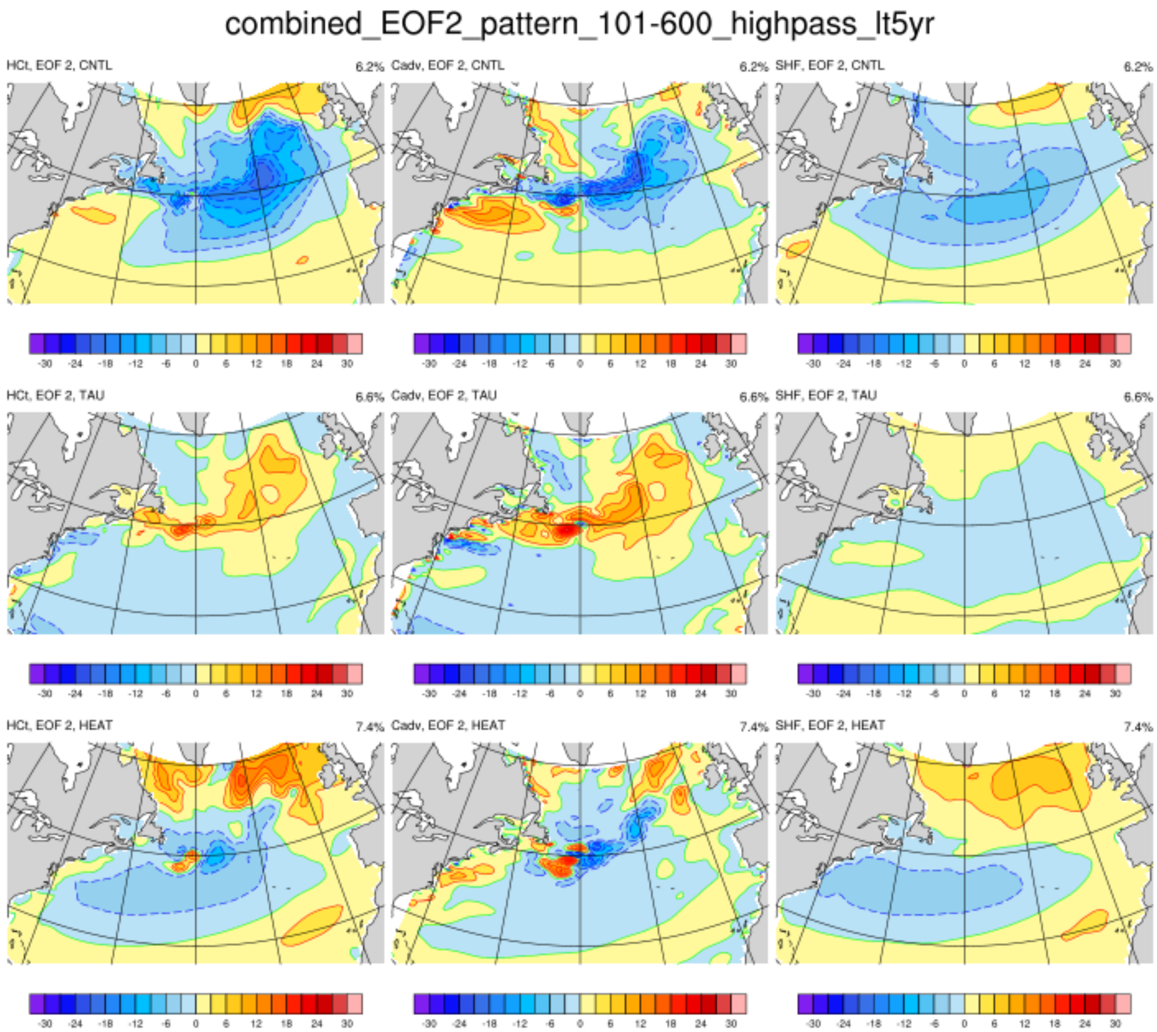

Figure 4.14: Same as Fig. 4.13, but for EOF2

Chapter 5: The impacts of surface momentum flux anomalies

The purpose of this chapter is to investigate how the surface wind stress, i.e. momentum flux, influences the Atlantic Ocean variation on multidecadal time scales. Therefore, in the TAU run, we turn off the interannual variability of the surface atmospheric state variables and keep the interannual variability of wind stress, thus we can isolate the variability of wind stress.

5.1 The variation of different variables in TAU run

In this section, we will introduce some basic features about how different variables changes in the TAU run. To begin with, let's examine the standard variance of surface wind stress in Fig. 5.1. As usual, five-year mean is performed. Therefore, the shown variance only accounts for the long-term fluctuation. Since some studies (YD14) indicate that wind stress drives the interannual variability of AMV, we also calculate the variance without a five-year running mean and find a similar variance pattern only with a larger amplitude (not shown). The maximum TAUX variance is around 0.016 Nm^{-2} and located near 60°N. The spacial pattern of the TAUX variance is predominantly zonal. Although TAUY has a similar spacial pattern and maximum variance location, the value is much smaller than TAUX. In the previous section, we have introduced the climatology of the wind stress (Fig. 3.2d), a westward wind stress in the subtropical region and eastward wind stress in the mid-latitude and subpolar area. However, in Fig. 5.1 we find that the wind stress in the subpolar region has a much larger variance than the wind stress in the south for both TAUX and TAUY. Another feature is that the variance of TAUX is larger than TAUY. As the climatology of TAUX is larger than TAUY, the same percentage perturbation will lead to a larger variance for TAUX than for TAUY. Also note that the maximum wind stress variance region does not overlap the maximum HC variance in the TAU run (Fig. 3.15d). The wind stress varies mainly in the northern part of the ocean over 50°N, whereas the HC variance is located along GS region around 45°N. How does this wind stress variance pattern impact the HC? We will discuss this issue in the following sections.

Since our goal in this study is to compare with YD14, here let's compare the wind stress variance with them. The data used by YD14 is 6 hourly phase II of the Coordinated Ocean-Ice Reference Experiments (CORE2) historic atmospheric data set over year 1948-2007. This data set is based primarily on the National Centers for Environmental Prediction-National Center for Atmospheric Research (NCEP-NCAR) reanalysis but has adjustments. More details about this data set can be found in YD14. As it is a 6 hourly data, the annual mean is applied and then 5 year running mean is taken. Wind stress is calculated based on $\tau = C_D \rho_{air} U^2$, where τ is the wind stress, C_D is dimensionless drag coefficient with the value of 0.0013, ρ_{air} is sea surface air density, which equals to 1.22 kgm^{-3}, U is the CORE2 wind speed at 10 m above the sea surface with the unit ms^{-1}. This gives τ the unit of Nm^{-2}. The CORE2 wind stress variance is shown in Fig. 5.2. The variance of TAUX has two centers, one is in the subpolar gyre region and the other one is located in the subtropical region. The maximum variance is about 0.006 Nm^{-2}. Compared with TAUX, the variance for TAUY is small over the entire basin, except in the southeast region. If we compare our wind stress (Fig. 5.1) with the wind stress used by YD14 (Fig. 5.2), we can find many differences. First, the TAUX variance in our model has only one maximum center in the north. Second, the maximum of our TAUX variance is 0.016 Nm^{-2}, which is larger than the CORE2 data. Third, the maximum TAUY is located in the subpolar gyre region in our model instead of in the southeast as shown in Fig. 5.2b.

Next, let's investigate the variation of HC, wind stress, AMOC, and ocean current with the respect to the AMOC index in the TAU case. To find out the subpolar gyre anomalies, the barotropic stream function (BSF) is also examined. Fig. 5.3 shows the results of the HC and surface wind stress regressed on AMOC index. At lag=-28, i.e. 28 years before AMOC's maximum peak, the HC anomaly is very small, but we can still see a negative pattern in transition zone (TZ) and a positive anomaly in the east of TZ and subpolar gyre region. At lag=-28,-21 and -14, the wind stress is relatively weak as well. At the same time, AMOC and top 500m mean current is also very weak, as shown in Figs. 5.5 and 5.6, respectively. In Fig. 5.6, negative BSF anomalies (blue color) are correlated with counter-clockwise current anomalies, and positive BSF anomalies are correlated with clockwise current anomalies. The region is zoomed in for more details. As time goes by, the shape of HC does not change that much but gets strengthened until lag=0 (Fig. 5.3e). In the mean while, the AMOC, BSF, ocean current and wind stress are getting strengthened synchronously (panels a-e of Figs. 5.5, 5.6, 5.3). When the AMOC gets to its maximum at lag=0 (Fig. 5.5e), the wind stress anomaly gets its maximum, a clockwise (anti-cyclonic) wind stress anomaly over the subpolar gyre region and the strongest westward signal along the GS (Fig. 5.3e), or in the vorticity field, a very strong negative curl over the subpolar gyre and positive vorticity over the subtropical gyre (Fig. 5.4e). This negative wind stress curl anomaly is in line with the positive HC anomaly underneath it, which should be the result of the Ekman pumping.

However, the anti-cyclonic wind stress is not in agreement with the cyclonic current anomaly or the negative BSF anomaly (Fig. 5.6e) underneath. It seems that at lag 0 the current anomaly is not correlated with the wind stress anomaly directly. The reason is the anti-cyclonic wind curl (Figs. 5.3e and 5.4e) generates downwelling underneath it as a result of the Ekman pumping. To verify the downwelling, the top 500 meter mean vertical velocity (W500) is calculated and regressed on the AMOC index at lag 0, shown in Fig. 5.7. We can find that over most of the subpolar gyre region and transition zone (TZ), it is downwelling. The negative W500 pattern overlaps negative wind curl pattern (Fig. 5.4e) very well. If we take the meridional mean of W500 between 50-60°N (Fig. 5.8), we find that the downwelling is mainly between longitude 320-340°, which is on the east boundary of the subpolar gyre. This downwelling in the east squeezes subpolar gyre to the west (Fig. 5.6e), thus strengths the Labrador current along the eastern coast of Canada. This strengthened Labrador current carries more cold water southward and generates the negative HC anomaly in the TZ. After lag=0, the AMOC decreases from its maximum value (Fig. 5.5e-i, from

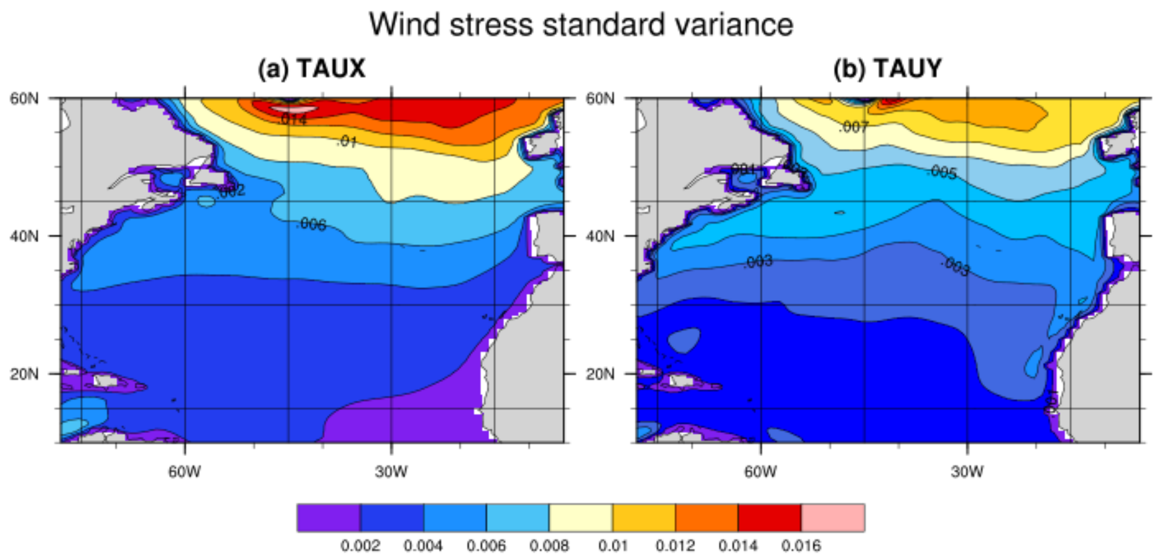

Figure 5.1: CESM pre-industrial run wind stress standard variance for (a) TAUX and (b) TAUY over model year 101-600. Unit is N/m^2. 5-yr running mean is applied.

lag=0 to 28) and accordingly, the zonal HC gradient is getting small, which means that the northward current is weakened. We can also find the northward current near GS extension region becomes weaker after lag 0 from Fig. 5.6.

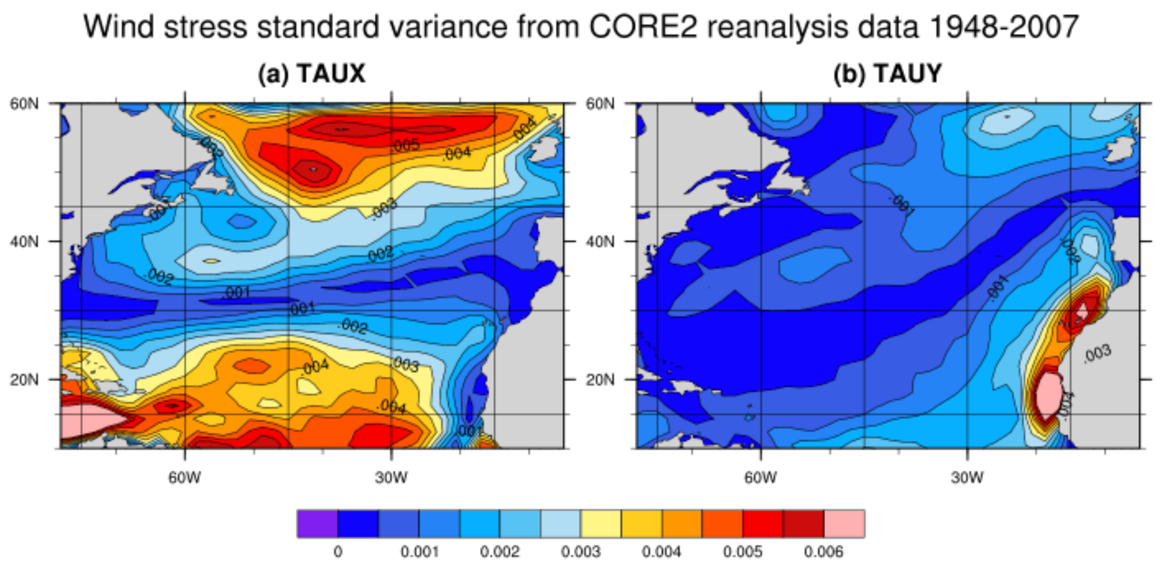

Figure 5.2: CORE2 wind stress standard variance for (a) TAUX and (b) TAUY over year 1948-2007. Unit is N/m^2. Five-year running mean is applied.

5.2 The heat budget analysis for TAU case

In the TAU run, since SHF only plays a role as restoring force and diffusion term always damps the temperature anomaly, in the heat budget equation the only term that is important for generating the HC variation is the advection term. Therefore, for the heat budget analysis in the TAU experiment, we only focus on the advection term here.

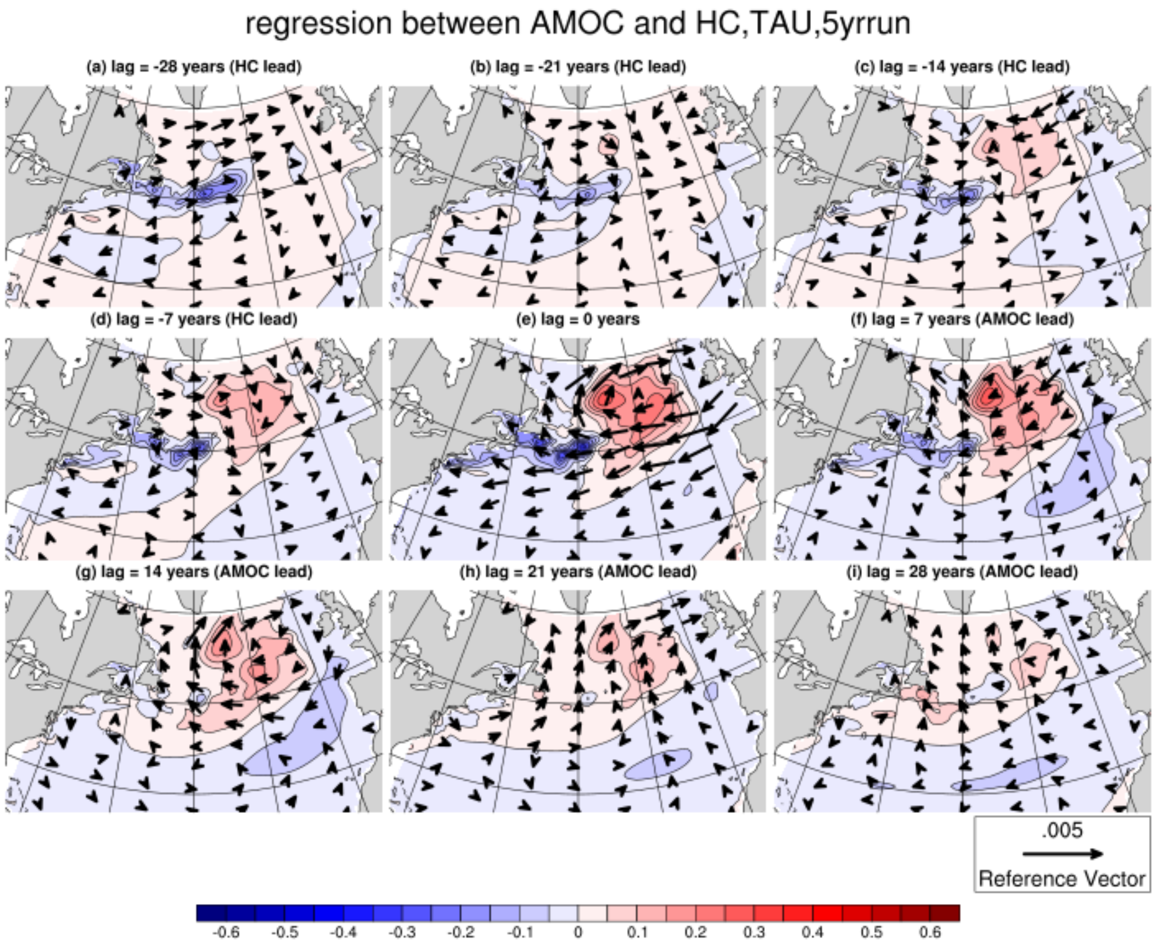

Figure 5.3: Lead-lag regression of HC (°C) and wind stress (N/m^2) on AMOC index.

5.2.1 The impact of advection on HC

Since the importance of advection in the TAU run as we mentioned above, let's investigate the advection term first. Fig. 5.9 shows the C_{adv} term in the heat budget equation 4.3, regressed on AMOC index. In the TZ (shown in Fig. 3.1), there is always a negative HC advection there. From lag -28 to -21, this negative advection seems to weaken. Then the magnitude increases from lag -21 to 0 and decreases from lag 0 to 28. In the subpolar

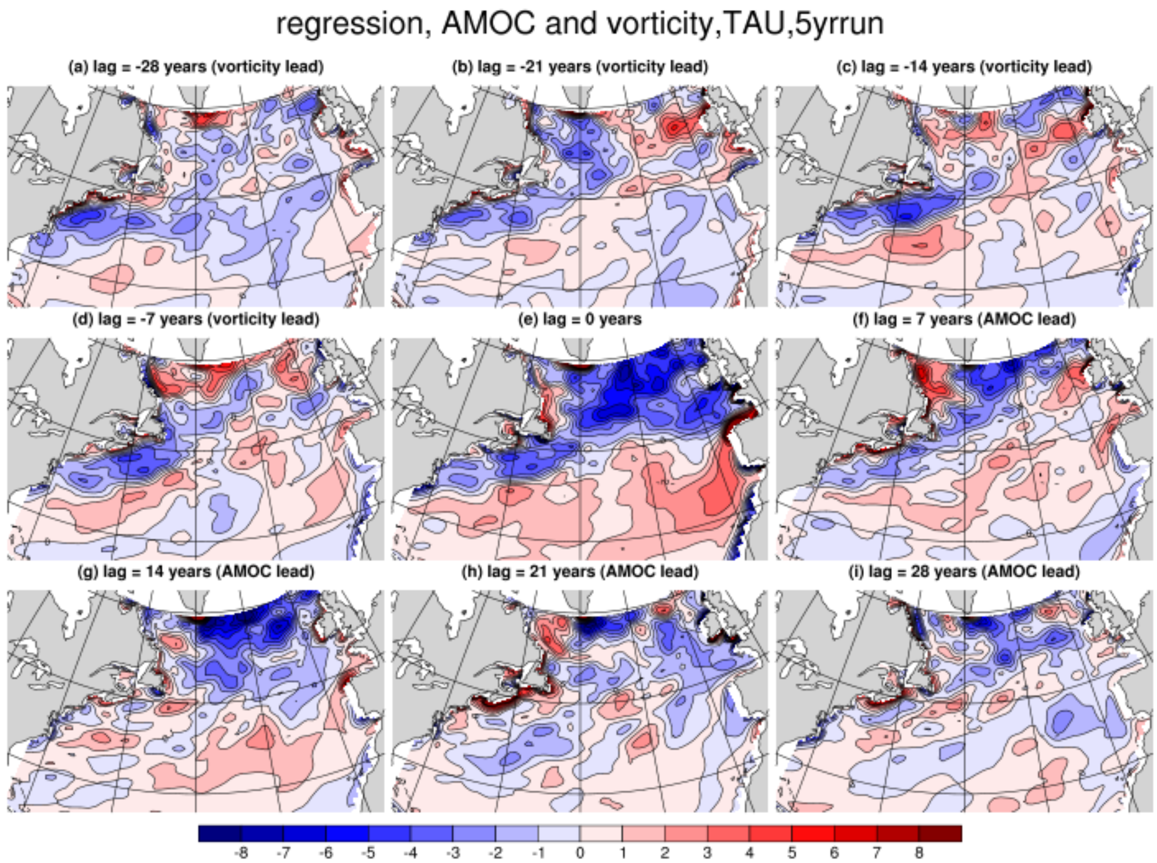

Figure 5.4: Lead-lag regression of wind stress curl on the AMOC index. Unit is 10^{-9} Nm^{-3}.

region, the effect of the advection is relatively weak at -28 and -21. A few years later it is strengthened, and after lag 0 it gets weakened. During the increasing period, C_{adv} dominants the sign of HC tendency (Fig. 5.10) although SHF (Fig. 5.11) damps the HC anomaly caused by advection. After lag 0, HC anomalies get the maximum, which leads to SHF strong enough to dominant the HC tendency. For example, at lag=0, the sign of HC tendency is determined by SHF in the TZ. Because of this positive HC tendency at lag=0 in

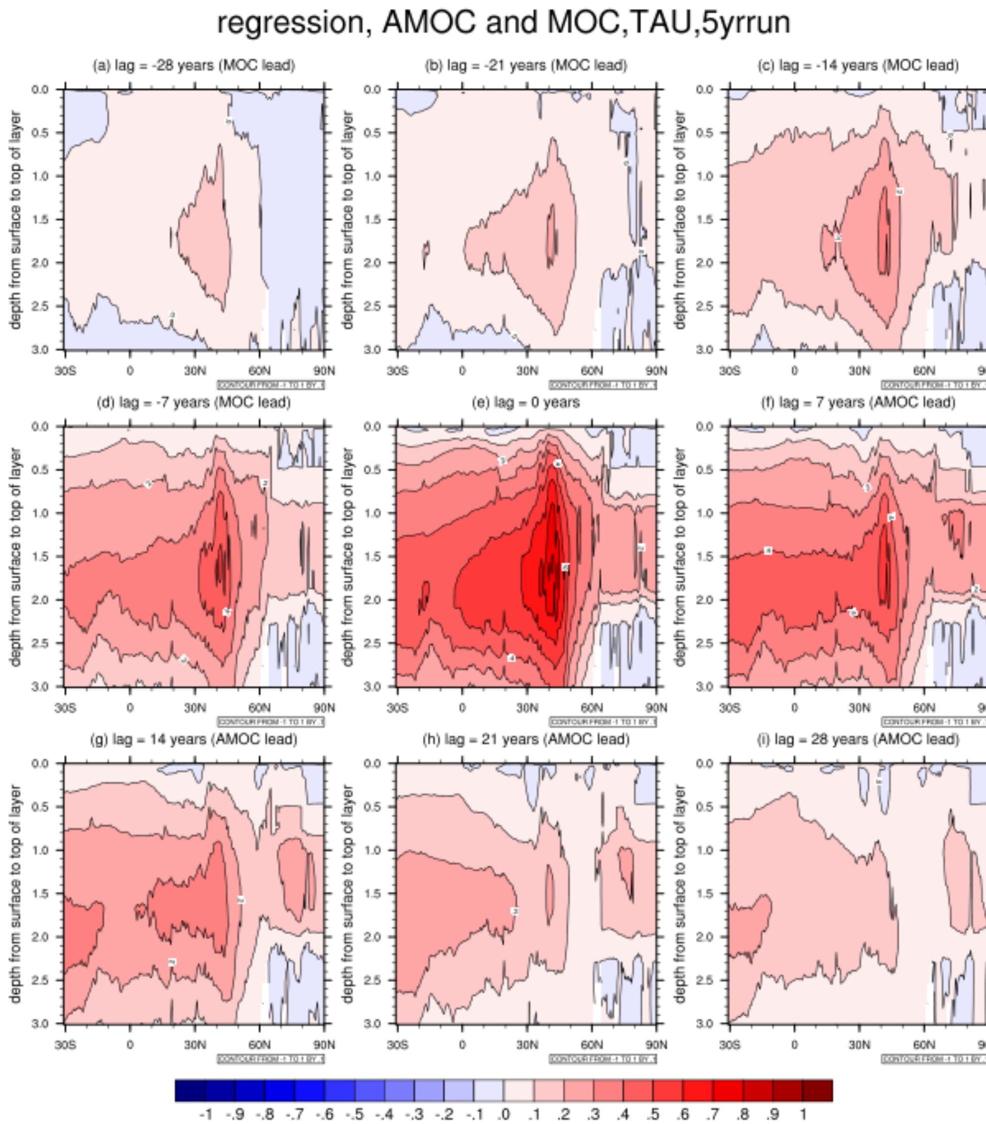

Figure 5.5: Lead-lag regression of AMOC stream function on AMOC index in the TAU run. Unit is Sv.

TZ, in the next panel at lag 7, the negative HC anomalies in TZ are weakened. Therefore, from Fig. 5.9 to Fig. 5.11, we can find that C_{adv} plays an important role for the HC anomalies build-up. SHF always damps the HC anomalies. It is too weak to dominant the HC tendency during the HC anomalies increasing period, but it becomes more important to the HC tendency after HC anomalies get the maximum peak.

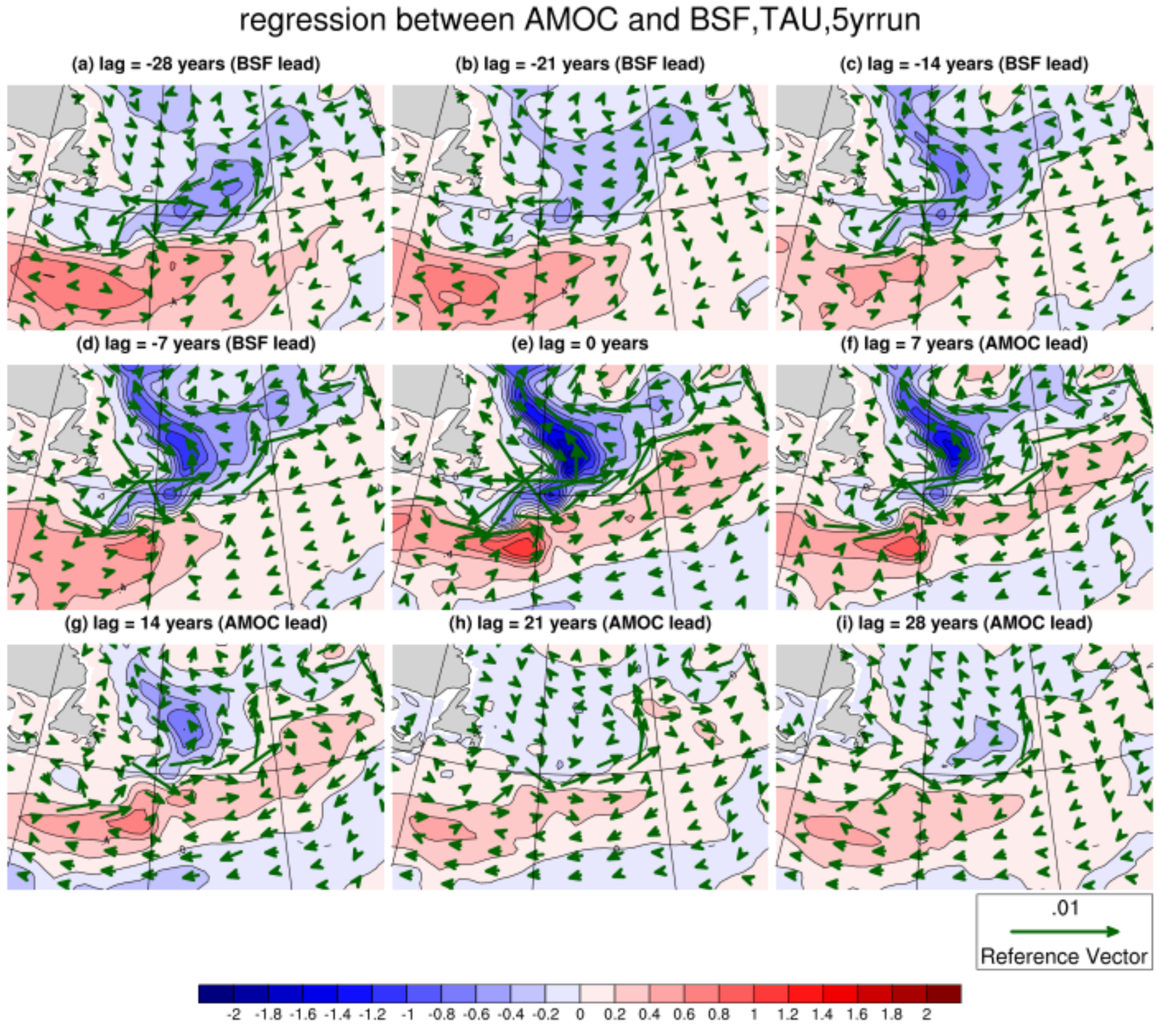

Figure 5.6: Lead-lag regression of the BSF (Sv) and ocean current (m/s) on the AMOC index for the TAU run.

Both the velocity fluctuation and the temperature fluctuation can impact the advection variation. To find out which is the dominant factor, the advection term is further decomposed into four terms

$$C_{adv}(\vec{u}, T) = C_{adv}(\overline{\vec{u}}, \overline{T}) + C_{adv}(\overline{\vec{u}}, T') + C_{adv}(\vec{u}', \overline{T}) + C_{adv}(\vec{u}', T') \tag{5.1}$$

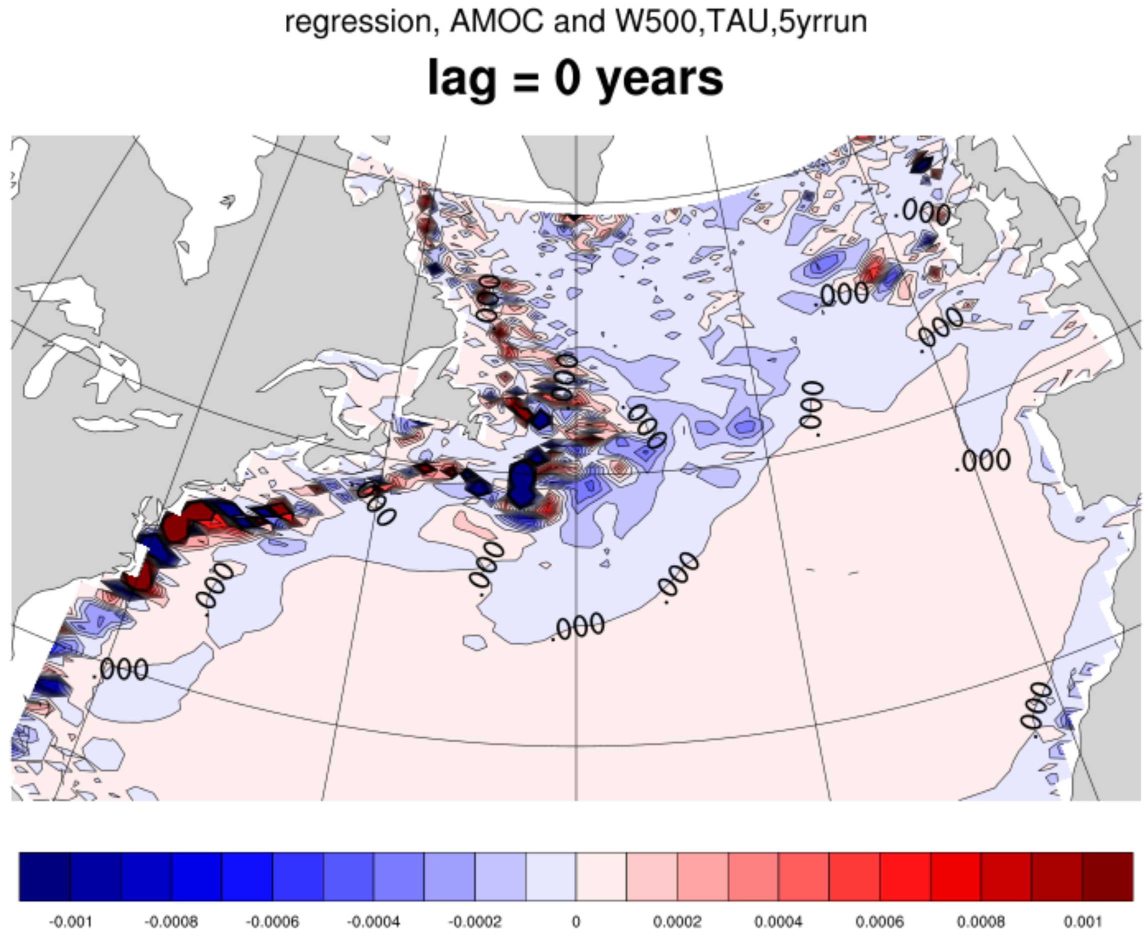

Figure 5.7: Regression of the top 500 mean vertical velocity on the AMOC index at lag 0 in the TAU run. Unit is m/s.

where $\overline{\vec{u}}$ is the mean velocity, $\overline{T}$ is the mean temperature, $\vec{u}'$ is the perturbation of the velocity and T' is the perturbation of the temperature. As $C_{adv}(\overline{\vec{u}}, \overline{T})$ is a constant and $C_{adv}(\vec{u}', T')$ is too small compared with other terms, the advection fluctuation can be written as

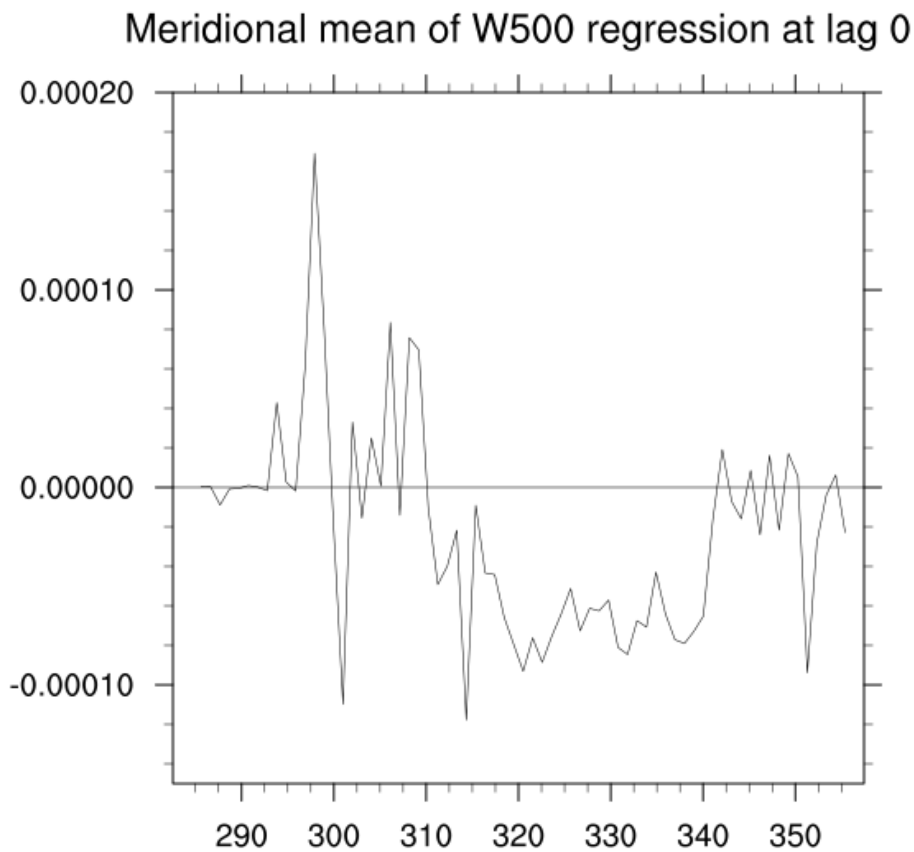

Figure 5.8: The meridional mean between 50-60°N of the top 500m average vertical velocity regressed on the AMOC index at lag 0 in the TAU run. X axis is longitude and Y axis is vertical velocity with unit m/s.

$$C'_{adv}(\vec{u}, T) \approx C_{adv}(\overline{\vec{u}}, T') + C_{adv}(\vec{u}', \overline{T}) \tag{5.2}$$

where $C_{adv}(\overline{\vec{u}}, T')$ represents the impact of the temperature fluctuation on the advection, and $C_{adv}(\vec{u}', \overline{T})$ represents the advection generated by the velocity fluctuation. We regress these two terms on the AMOC index and plot in Figs. 5.12 and 5.13, respectively. In Fig. 5.12, panel a-e have similar pattern only with different magnitude. The maximum is along the 45°N latitude, a positive anomaly on the west and a negative anomaly on the east. At lag 0 (panel e), the northeast region also has a large positive advection anomaly generated by the temperature perturbation. From lag 7 to 28 (Fig. 5.12f-i), the pattern along GS has changed. There is a positive anomaly right in the middle (45°N 45°W), and negative anomalies next to it. As for term $C_{adv}(\vec{u}', \overline{T})$ (Fig. 5.13), the pattern is opposite to $C_{adv}(\overline{\vec{u}}, T')$. Comparing $C_{adv}(\vec{u}, T)$, $C_{adv}(\overline{\vec{u}}, T')$ and $C_{adv}(\vec{u}', \overline{T})$ (Figs. 5.9, 5.12 and 5.13), we conclude that the advection generated by the velocity perturbation is more similar to the total advection along the GS extension region, and the other term, $C_{adv}(\overline{\vec{u}}, T')$, determines the total advection in the northeastern region (around 50°N 20°W).

The physical process why $C_{adv}(\overline{\vec{u}}, T')$ and $C_{adv}(\vec{u}', \overline{T})$ are opposite is explained in Fig. 5.14. Along the GS extension region, the temperature gradient is to the north. In this figure, horizontal lines represent temperature climatology ($\overline{T}$), warm in the south (red) and cold in the north (blue). The velocity climatology ($\overline{\vec{u}}$, shown as black arrows) is parallel to the isotherm. If there is a positive temperature anomaly in the middle (red circle), the climatological velocity ($\overline{\vec{u}}$) generates negative/positive advection on the left/right of the circle. Therefore, $C_{adv}(\overline{\vec{u}}, T')$ drives a negative advection anomaly on the left and positive anomaly on the right. Due to the geostrophic balance, this temperature anomaly is related with anticyclonic velocity anomaly ($\vec{u}'$, shown as blue curved arrows). The velocity anomaly on the left/right brings warm/cold water from south/north to north/south, generating a positive/negative advection anomaly. Therefore, $C_{adv}(\vec{u}', \overline{T})$ generates positive advection on the left and negative advection on the right. That is why $C_{adv}(\overline{\vec{u}}, T')$ and $C_{adv}(\vec{u}', \overline{T})$ are opposite.

Combining Figs. 5.3, 5.4, 5.6, 5.7, 5.8 and 5.13, now we can explain the role of the surface wind forcing. When an anti-cyclonic wind stress appears in the subpolar gyre region (Fig. 5.3e), it is related to a negative wind stress curl (Fig. 5.4e). This negative wind stress curl not only generates positive HC anomalies underneath it (Fig. 5.3e), but also leads to downwelling through Ekman pumping (Fig. 5.7). Because this downwelling is primarily in the mid-east region (Fig. 5.8), the subpolar gyre is squeezed to the west (Fig. 5.6e), as a result of which the Labrador current and the northeastward current anomaly around latitude 45°N are strengthened. The strengthened currents lead to $C_{adv}(\vec{u}', \overline{T})$ pattern we see in Fig. 5.13), then determine the total advection and impact the HC.

5.2.2 The impact of Ekman current on HC advection

The current in C_{adv} can be decomposed into two parts, the Ekman current ($\vec{u}_{ek}$) generated by wind stress and the geostrophic current component. Accordingly, C_{adv} can also be decomposed into two parts, the advection component generated by the Ekman current and the component generated by geostrophic current, i.e.

$$C_{adv}(\vec{u}, T) = C_{ek}(\vec{u}_{ek}, T) + C_{geo}(\vec{u}_{geo}, T) \tag{5.3}$$

In order to find out the impact of wind stress on C_{adv}, it would be necessary to check the influence of C_{ek}, as $\vec{u}_{ek}$ generated directly by wind stress. C_{geo} can also be correlated with wind stress, as wind stress curl can impact the isopycnal through Ekman pumping and thus impact the geostrophic current. We will check C_{geo} in the next section. The relationship between $\vec{u}_{ek}$ and wind stress is given by the following equation:

$$\vec{u}_{ek} = \frac{\vec{\tau} \times \hat{z}}{\rho_0 f D_{ek}} \tag{5.4}$$

where $\vec{\tau}$ is wind stress vector, ρ_0 is the water density, f is the Coriolis parameter, and D_{ek} is Ekman layer depth, which is fixed at 100 meters in this study. $\vec{u}_{ek}$ is uniformly distributed from the surface to D_{ek} and zero below D_{ek}. Then substitute $\vec{u}_{ek}$ for $\vec{u}$ in C_{adv} and we get C_{ek}. More details about C_{ek} and C_{geo} can be found in Buckley et al. (2014).

The regression between C_{ek} and AMOC index is shown in Fig. 5.15. C_{ek} has the same

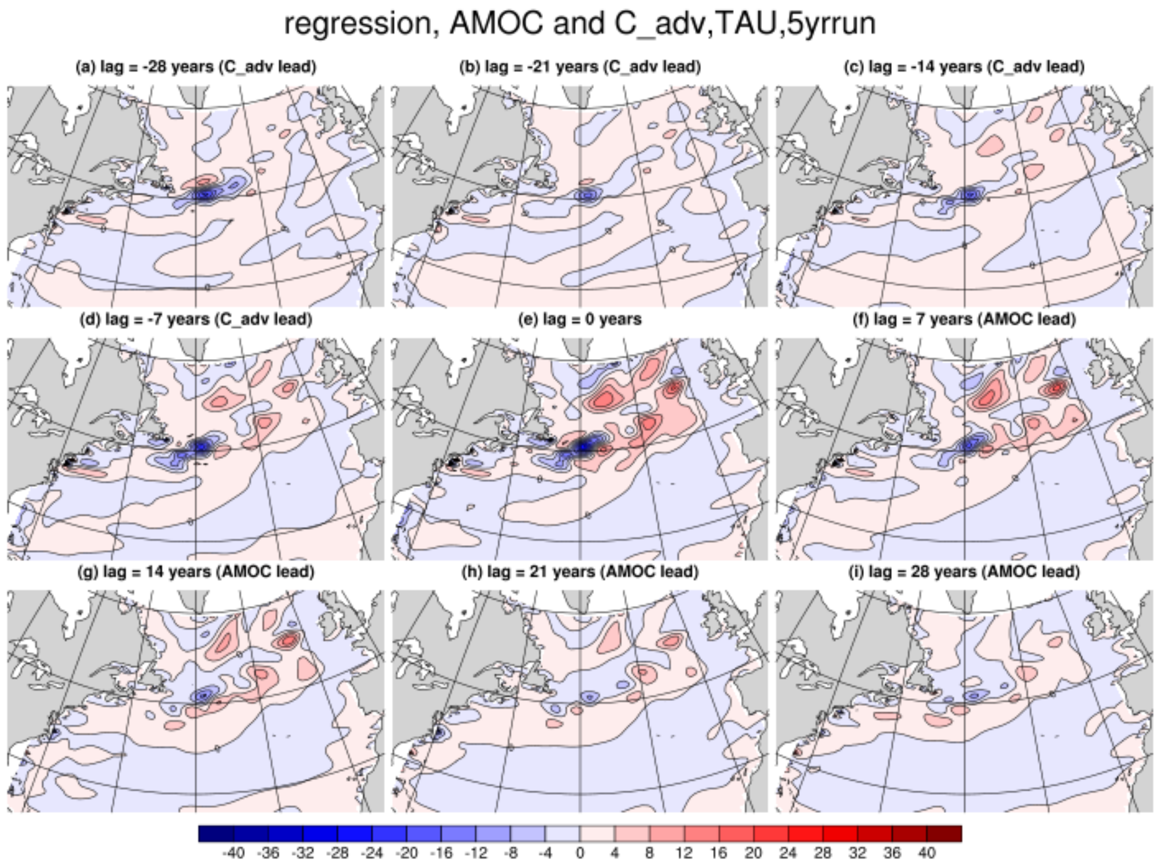

Figure 5.9: Lead-lag regression of C_{adv} on AMOC index for TAU. The nine-point local smoothing has been done for 4 times. Unit is W/m^2.

sign as the C_{adv} in a small region (the small blue spot, around 45°N 40°W) in the TZ and in the eastern part of the GS extension. The similarity between C_{ek} and C_{adv} demonstrates that Ekman current does make some contribution on the total HC advection in TAU run, although the magnitude of C_{ek} is smaller than that of C_{adv}.

To further investigate the C_{ek} term, we decompose it into the following four terms

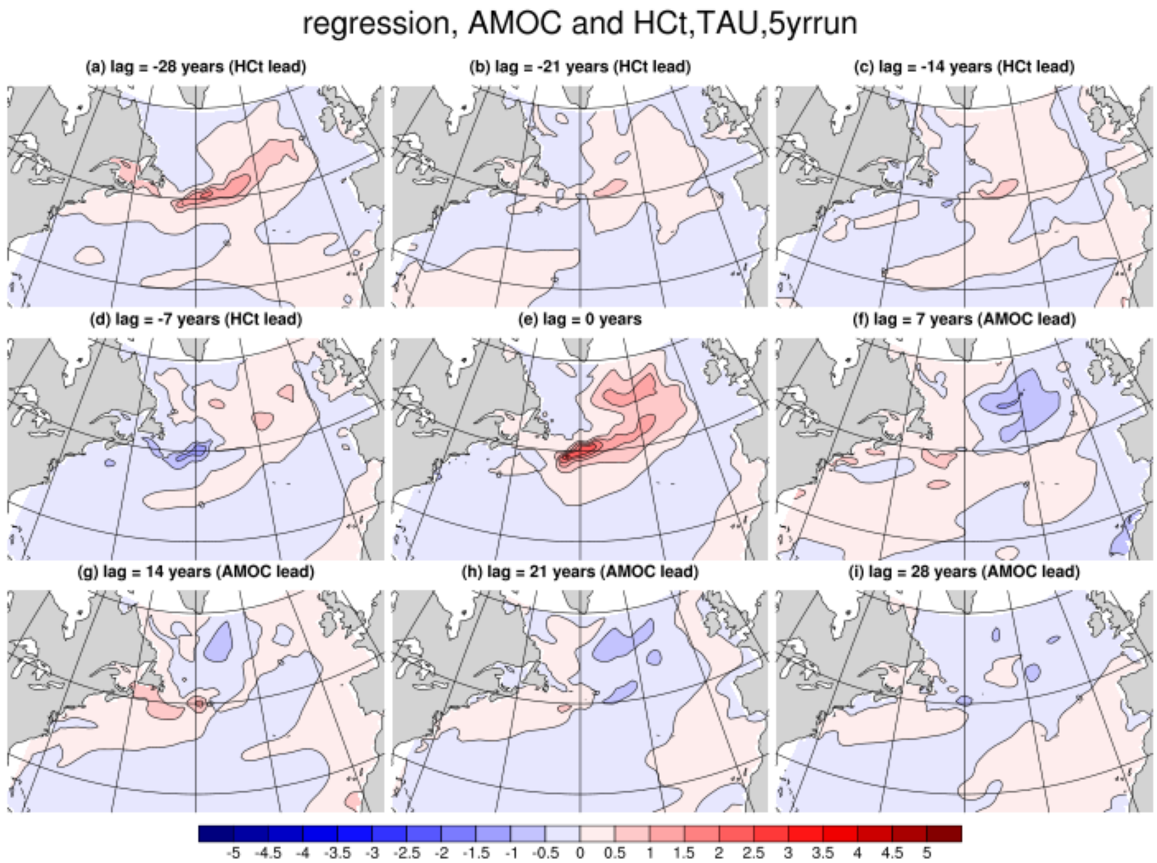

Figure 5.10: Lead-lag regression of HC tendency on AMOC index for TAU. Unit is W/m^2.

$$C_{ek}(\vec{u}_{ek}, T) = C_{ek}(\overline{\vec{u}}_{ek}, \overline{T}) + C_{ek}(\overline{\vec{u}}_{ek}, T') + C_{ek}(\vec{u}'_{ek}, \overline{T}) + C_{ek}(\vec{u}'_{ek}, T') \tag{5.5}$$

where $\overline{\vec{u}}_{ek}$ is the mean Ekman velocity generated by the mean wind stress, $\overline{T}$ is the mean temperature, $\vec{u}'_{ek}$ is perturbation of the Ekman velocity and T' is the perturbation of the temperature. As $C_{ek}(\vec{u}'_{ek}, T')$ is too small compared with other terms and $C_{ek}(\overline{\vec{u}}_{ek}, \overline{T})$

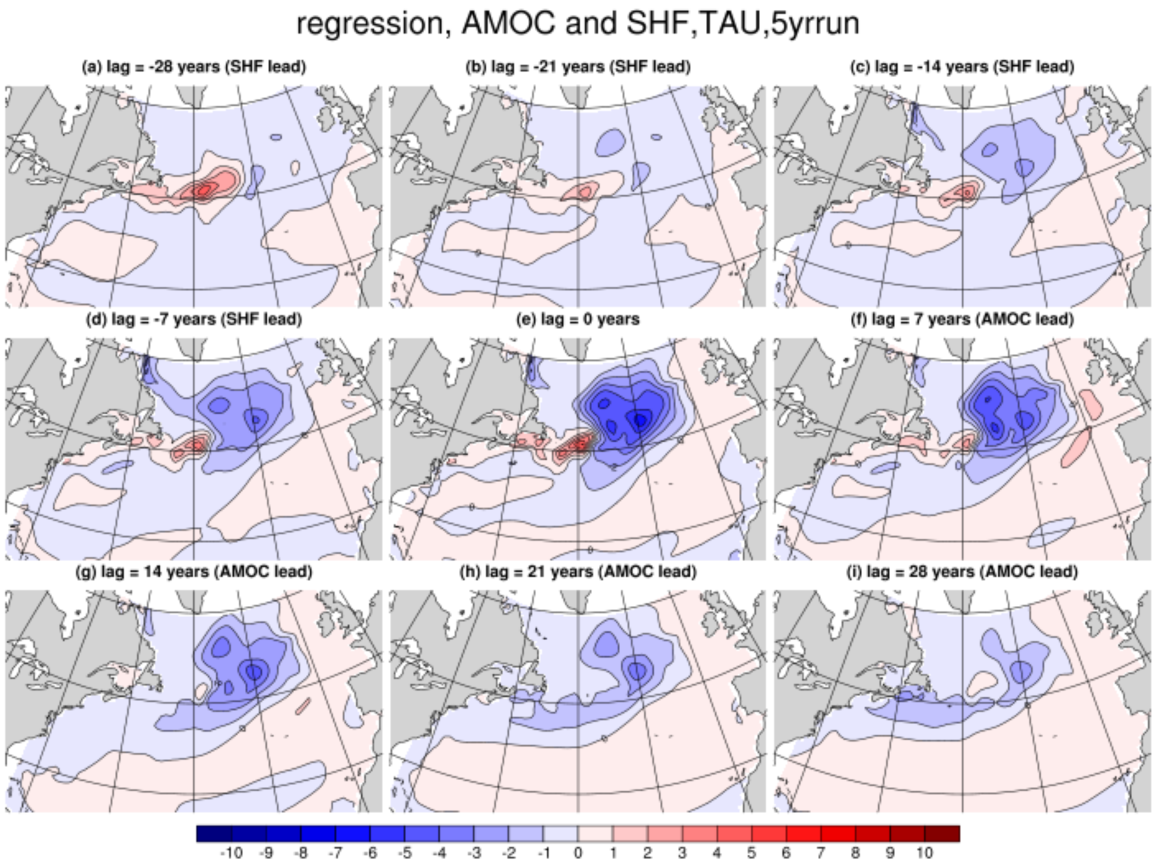

Figure 5.11: Lead-lag regression of SHF on the AMOC index in the TAU run. Unit is W/m^2.

only determines the mean state and doesn't change, the variation of C_{ek} is determined by the variation of velocity field advecting the mean temperature field and the perturbed temperature field advected by the mean velocity field, i.e.

$$C'_{ek} = C_{ek}(\overline{\vec{u}}_{ek}, T') + C_{ek}(\vec{u}'_{ek}, \overline{T}) \tag{5.6}$$

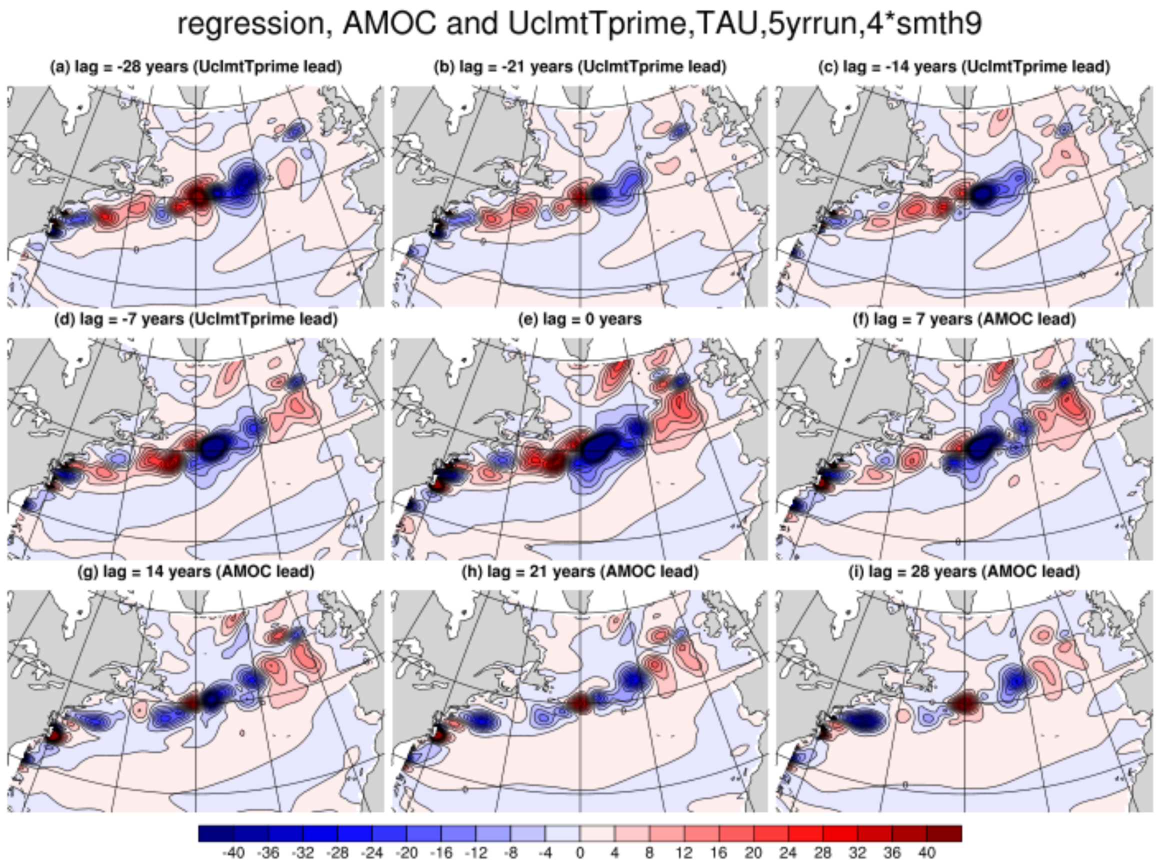

Figure 5.12: Lead-lag regression of $C_{adv}(\overline{\vec{u}}, T')$ on the AMOC index in the TAU run. The nine-point local smoothing has been done for 4 times. Unit is W/m^2.

We regress $C_{ek}(\overline{\vec{u}}_{ek}, T')$ and $C_{ek}(\vec{u}'_{ek}, \overline{T})$ on AMOC index and the results are shown in Figs. 5.16 and 5.17, respectively.

Comparing Figs. 5.15, 5.16 and 5.17, we can find that on one hand the temperature perturbation only counts for the Ekman advection in the TZ, as shown in Fig. 5.16. This may be due to the high HC variance and the wind stress climatology is not small in this

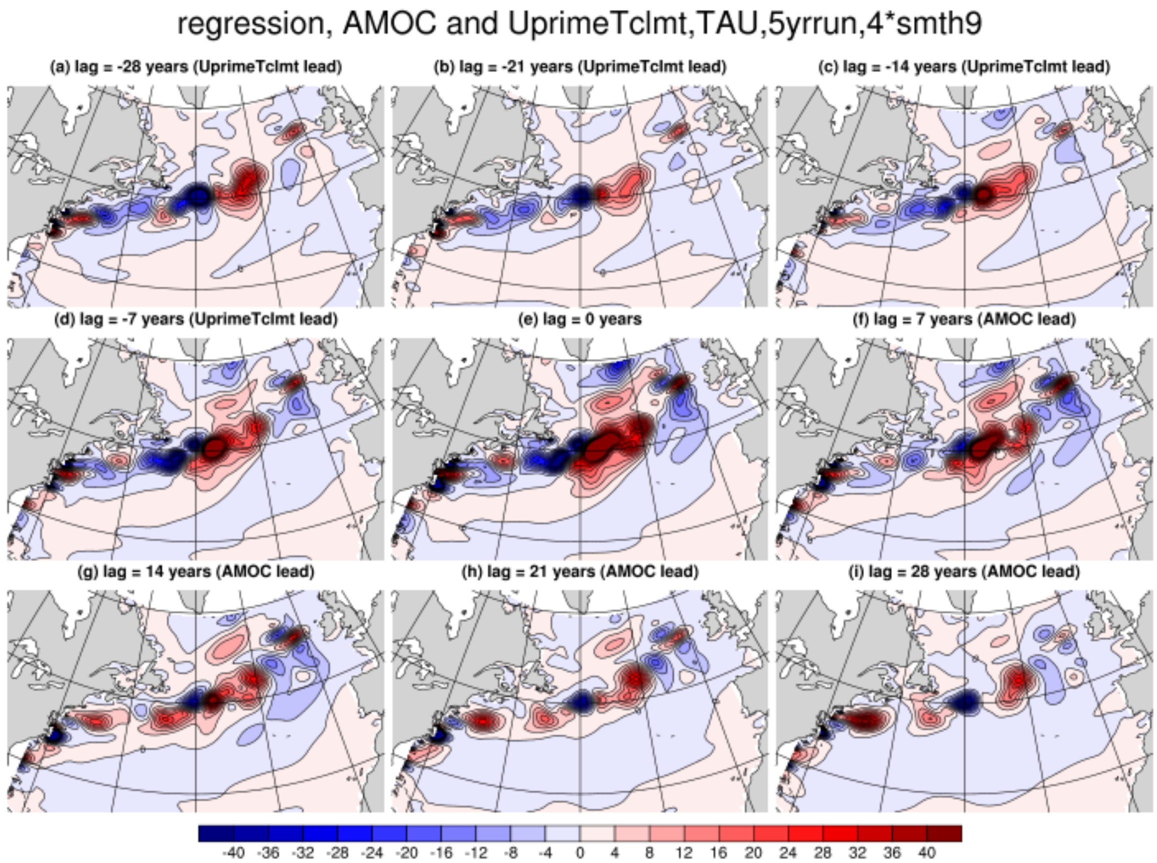

Figure 5.13: Lead-lag regression of $C_{adv}(\vec{u}', \overline{T})$ on the AMOC index in the TAU run. The nine-point local smoothing has been done for 4 times. Unit is W/m^2.

region. On the other hand, the Ekman current anomaly or the wind stress anomaly generates Ekman HC advection along GS and its extension region, as shown in Fig. 5.17. In the first few time snaps (lag -28, -21, -14 and -7), the wind stress anomalies only generate Ekman advection anomalies in the western boundary. At lag 0, this advection anomaly expands all the way to the northeast of the ocean. Soon it gets weakened and turns to negative phase.

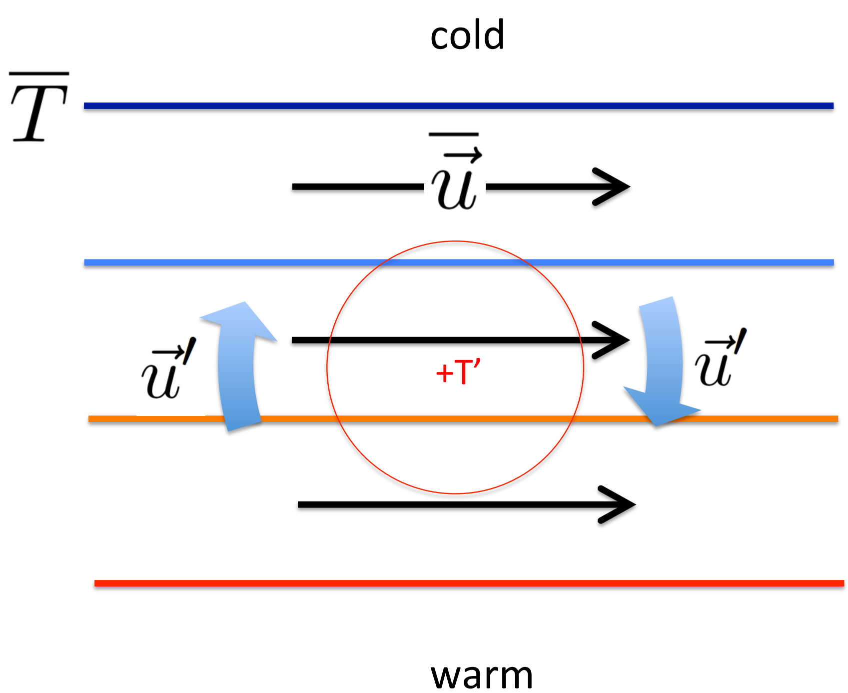

Figure 5.14: Schematic of why $C_{adv}(\vec{\overline{u}}, T')$ and $C_{adv}(\vec{u}', \overline{T})$ are opposite to each other. Horizontal lines represent temperature climatology ($\overline{T}$), warm in the south (red) and cold in the north (blue). Black arrows represent velocity climatology ($\vec{\overline{u}}$). Red circle in the center is a positive temperature anomaly (T'). Two curved blue arrows are velocity anomalies ($\vec{u}'$)

If we combine Figs. 5.16 and 5.17, we can find that the sum of $C_{ek}(\vec{\overline{u}}_{ek}, T')$ and $C_{ek}(\vec{u}'_{ek}, \overline{T})$ can represent most parts of the C_{ek} anomalies.

5.2.3 The impact of geostrophic current on HC advection

We have examined the C_{ek} term in the previous section. In this section, we examine the second term in Eq. 5.3, the HC advection generated by the geostrophic current, i.e. C_{geo}. First, we need to calculate the geostrophic current, which is given by

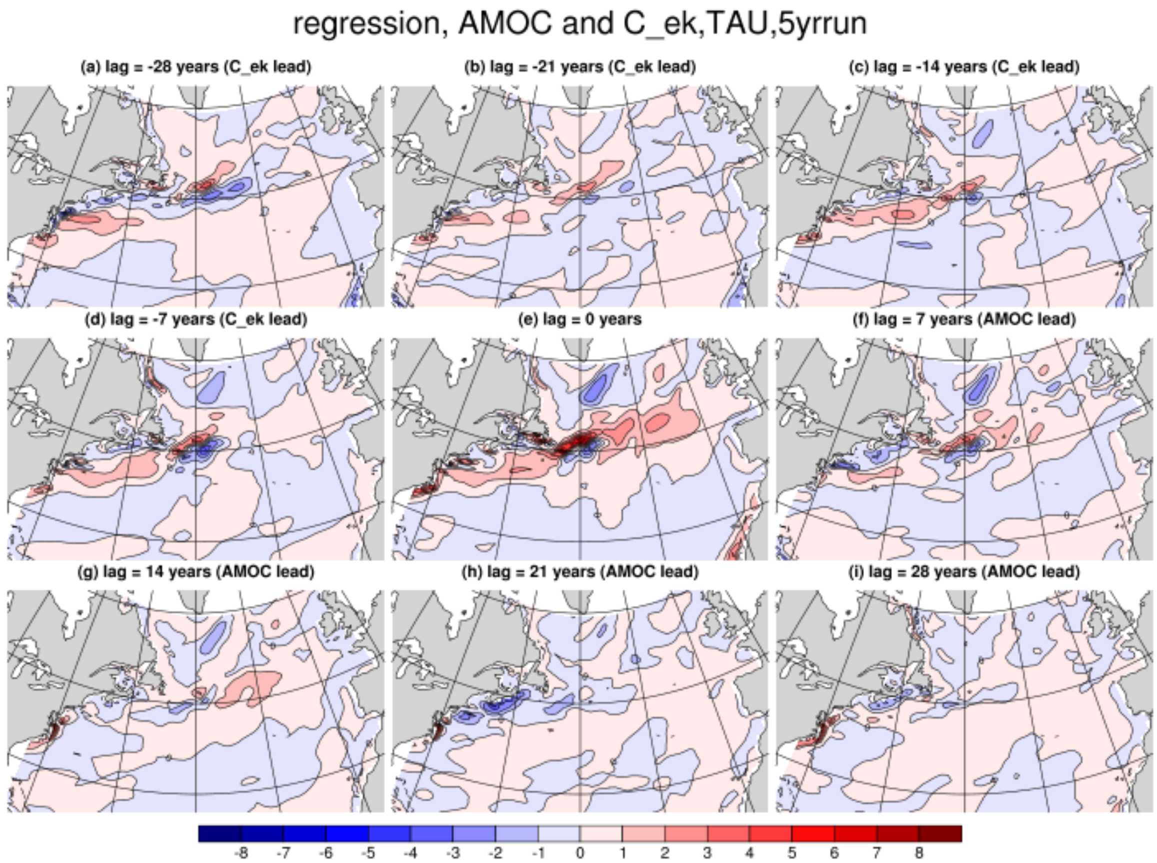

Figure 5.15: Lead-lag regression of C_{ek} (W/m^2) on AMOC index.

$$\vec{u}_{geo} = \frac{1}{\rho_0 f}\hat{z} \times \nabla p \tag{5.7}$$

where $\vec{u}_{geo}$ is the geostrophic current, ρ_0 and f are the same as in Eq. 5.4, and p is the pressure, which is calculated by $p = \rho g h$, where h is the sum of layer depth and sea surface height. If we compare the geostrophic current and the total current we can find that at

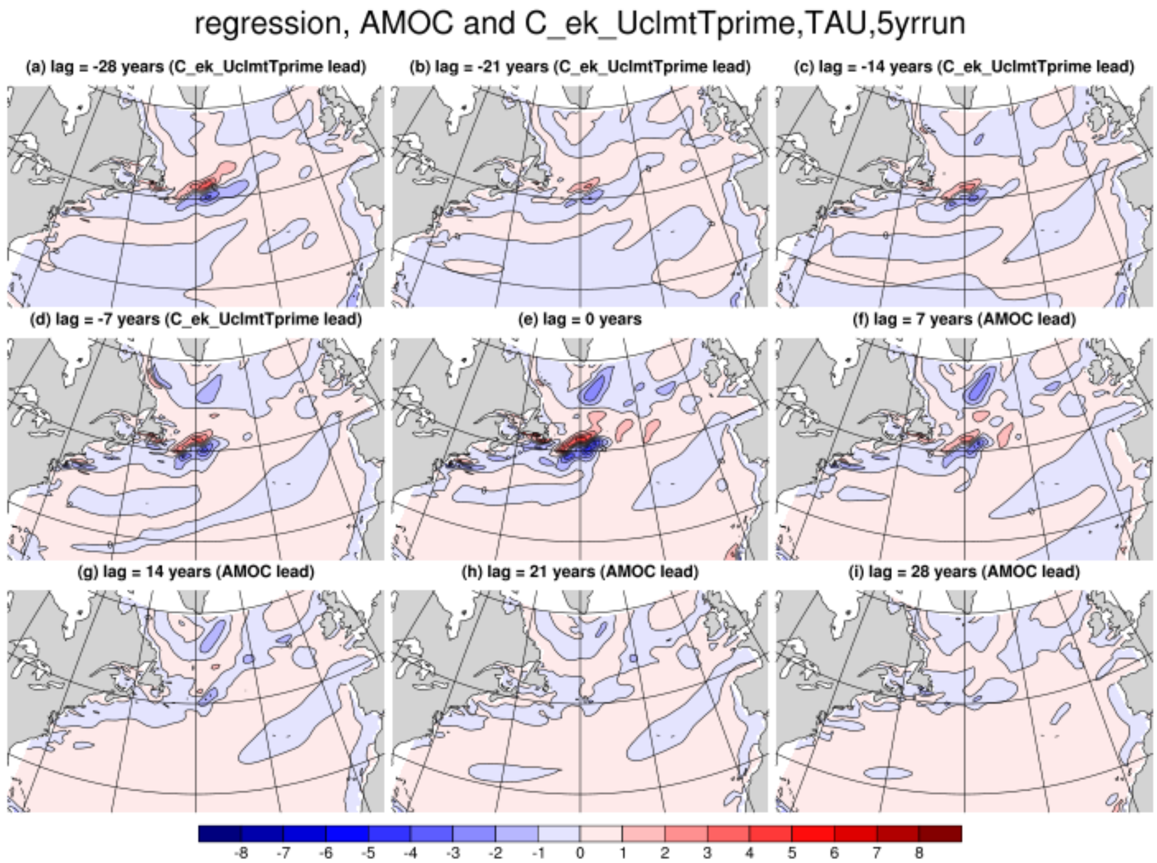

Figure 5.16: Lead-lag regression of $C_{ek}(\vec{\overline{u}}_{ek}, T')$ (W/m^2) on AMOC index.

the surface there is a bias between them in most of the regions in the basin (Fig. 5.18a). This indicates that at the surface the total current is influenced by both the Ekman current and the geostrophic current. In the deep ocean at depth=105 m, the total current and the geostrophic current are very close (Fig. 5.18b), as in the deep ocean the impact of the surface wind stress is very small.

Once we have $\vec{u}_{geo}$, then we can calculate C_{geo}, which is shown in Fig. 5.19. The first

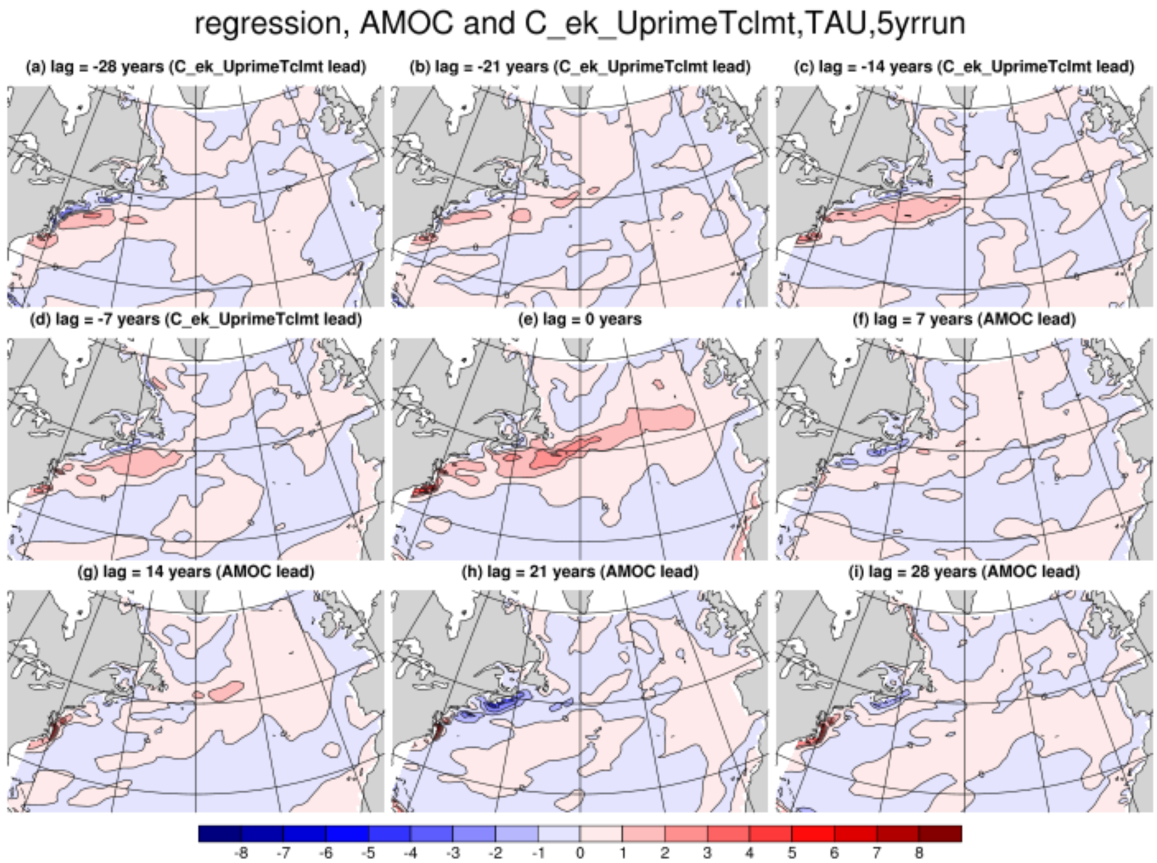

Figure 5.17: Lead-lag regression of $C_{ek}(\vec{u}'_{ek}, \overline{T})$ (W/m^2) on AMOC index.

thing we can notice is that the pattern of C_{geo} is very similar to C_{adv}, negative HC tendency in TZ and positive in the subpolar gyre. Second, the magnitude of C_{geo} is the same as C_{adv}. Therefore, C_{geo} is the dominant term for C_{adv} other than C_{ek}. In other words, $\vec{u}_{geo}$ plays a more important role in generating HC advection than $\vec{u}_{ek}$.

The next question is which term determines the C_{geo} anomalies, the perturbation of geostrophic current or the perturbation of temperature. To further investigate this question, similar to C_{ek}, we decompose C_{geo} into the following four terms

$$C_{geo}(\vec{u}_{geo}, T) = C_{geo}(\overline{\vec{u}}_{geo}, \overline{T}) + C_{geo}(\overline{\vec{u}}_{geo}, T') + C_{geo}(\vec{u}'_{geo}, \overline{T}) + C_{geo}(\vec{u}'_{geo}, T') \tag{5.8}$$

The meaning of each term in the above equation is very similar to Eq. 5.5. Similar to C_{ek}, the anomaly of C_{geo} is equal to

$$C'_{geo} = C_{geo}(\overline{\vec{u}}_{geo}, T') + C_{geo}(\vec{u}'_{geo}, \overline{T}) \tag{5.9}$$

where $C_{geo}(\overline{\vec{u}}_{geo}, T')$ represents the component of geostrophic advection generated by the fluctuation of temperature field, and $C_{geo}(\vec{u}'_{geo}, \overline{T})$ represents the component of C_{geo} generated by the perturbation of $\vec{u}_{geo}$. By comparing $C_{geo}(\overline{\vec{u}}_{geo}, T')$ and $C_{geo}(\vec{u}'_{geo}, \overline{T})$, we can find which field, the geostrophic current or the temperature, is more important to the variability of C_{geo}. The results of these two terms are shown in Figs. 5.20 and 5.21, respectively.

We can find that $C_{geo}(\overline{\vec{u}}_{geo}, T')$ term generates a positive HC tendency in TZ and a negative HC tendency on the east of TZ along the GS extension (Fig. 5.20e). This term determines the total geostrophic advection in the northern part. On the other hand, $C_{geo}(\vec{u}'_{geo}, \overline{T})$ leads to an opposite HC tendency to balance $C_{geo}(\overline{\vec{u}}_{geo}, T')$ term, and it dominates the total geostrophic HC transportation (Fig. 5.19) along the GS (Fig. 5.21e). Therefore, we conclude that the perturbed $\vec{u}_{geo}$ superimposed on the climatological temperature field determines the C_{geo} term in the GS extension region, a negative tendency in TZ and positive in the east. This pattern of $C_{geo}(\vec{u}'_{geo}, \overline{T})$ can be explained by Figs. 5.6 and 3.2d. Fig. 5.6 shows the vertical average of the perturbed total velocity ($\vec{u}'$) over the top 500 meters, which is very close to $\vec{u}'_{geo}$. We can see that the strengthened Labrador Current goes southward along the left side of the negative BSF anomaly. If this current is composed on the mean temperature field (Fig. 3.2d), it will bring cold temperature from the north and generate

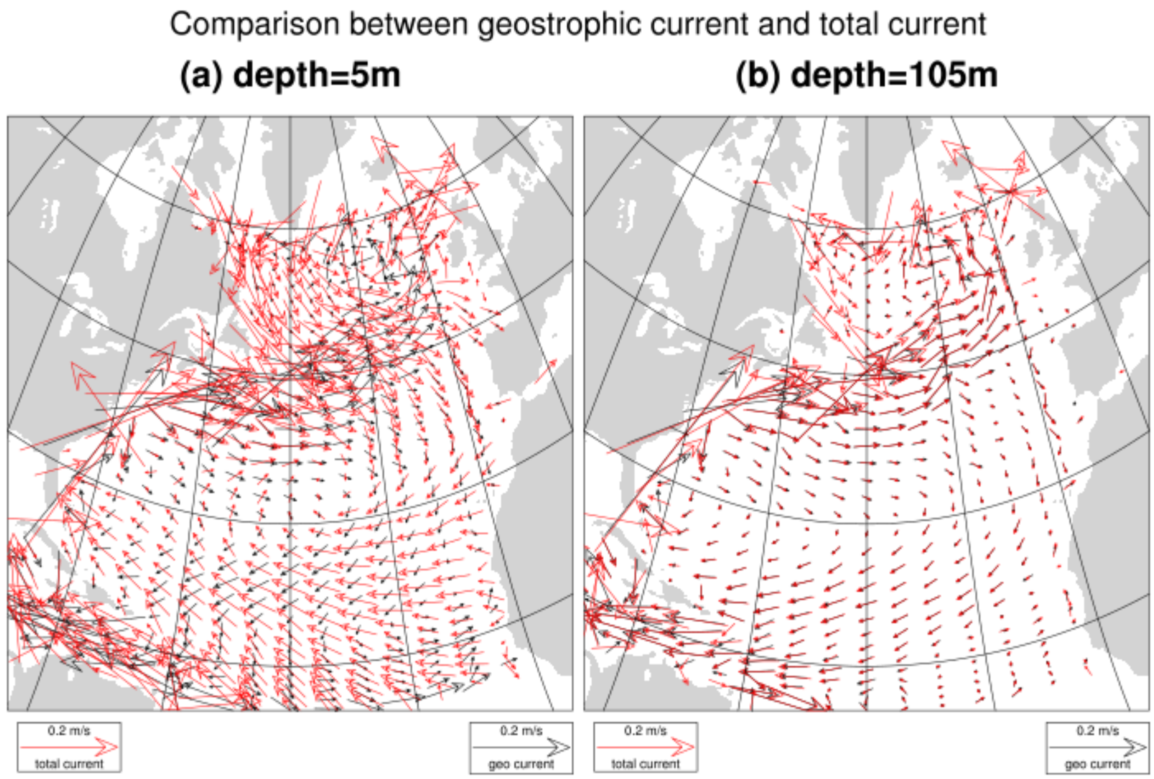

Figure 5.18: The comparison between the monthly mean geostrophic current and the monthly mean total current at depth (a) 5 meters and (b) 105 meters in Year 101 November.

negative temperature anomaly when it crosses GS in TZ. Another current goes northward on the right side of the negative BSF anomaly. This current brings warm water from the subtropical region to the subpolar gyre region and generates positive temperature anomaly. That is why we see the HC tendency pattern generated by $C_{geo}(\vec{u}'_{geo}, \overline{T})$ term, negative HC advection in TZ and positive HC advection in the east of TZ.

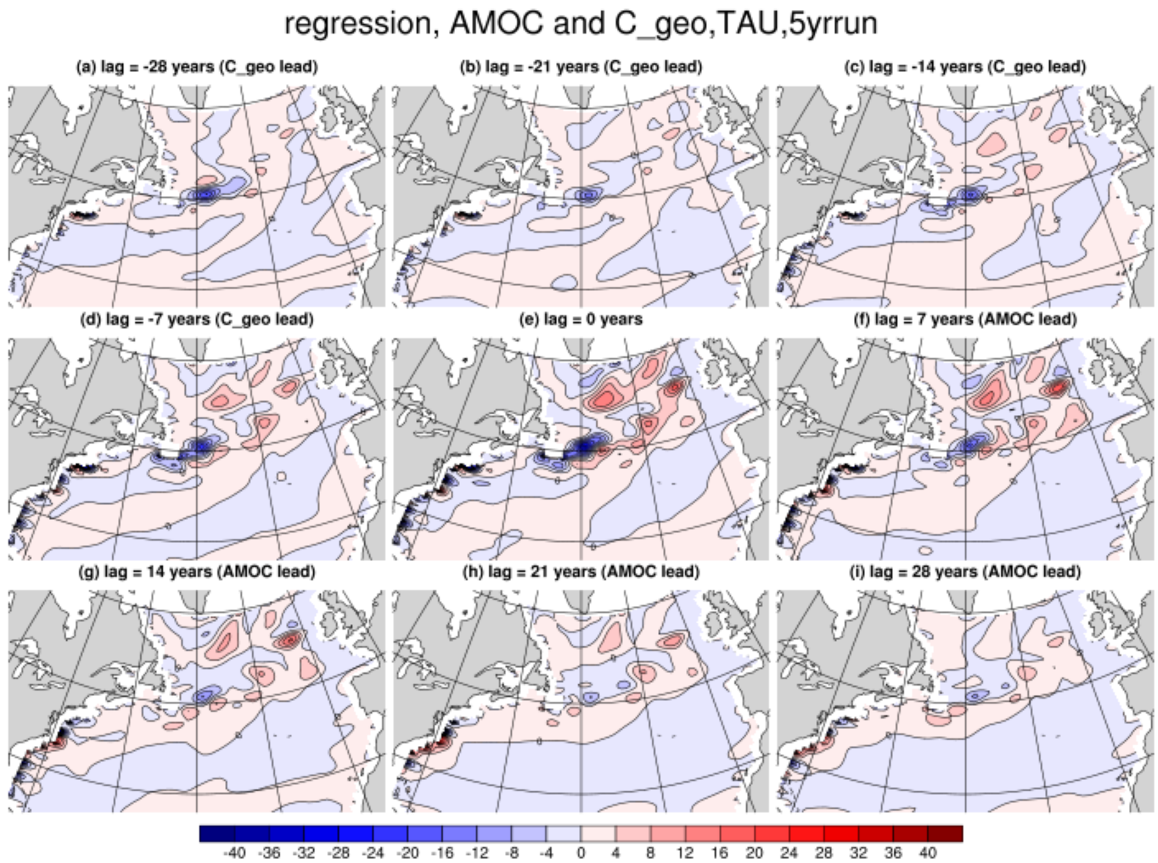

Figure 5.19: Lead-lag regression of C_{geo} (W/m^2) on AMOC index.

5.3 Summary

In this chapter, we turn off the interannual variability of the surface heat flux and isolate the impact of the wind stress on the AMV to investigate whether surface momentum flux (SMF) drives the multidecadal variability in the Atlantic Ocean. If it does, what are the physical processes associated with this process? Does SMF affect AMV directly by the

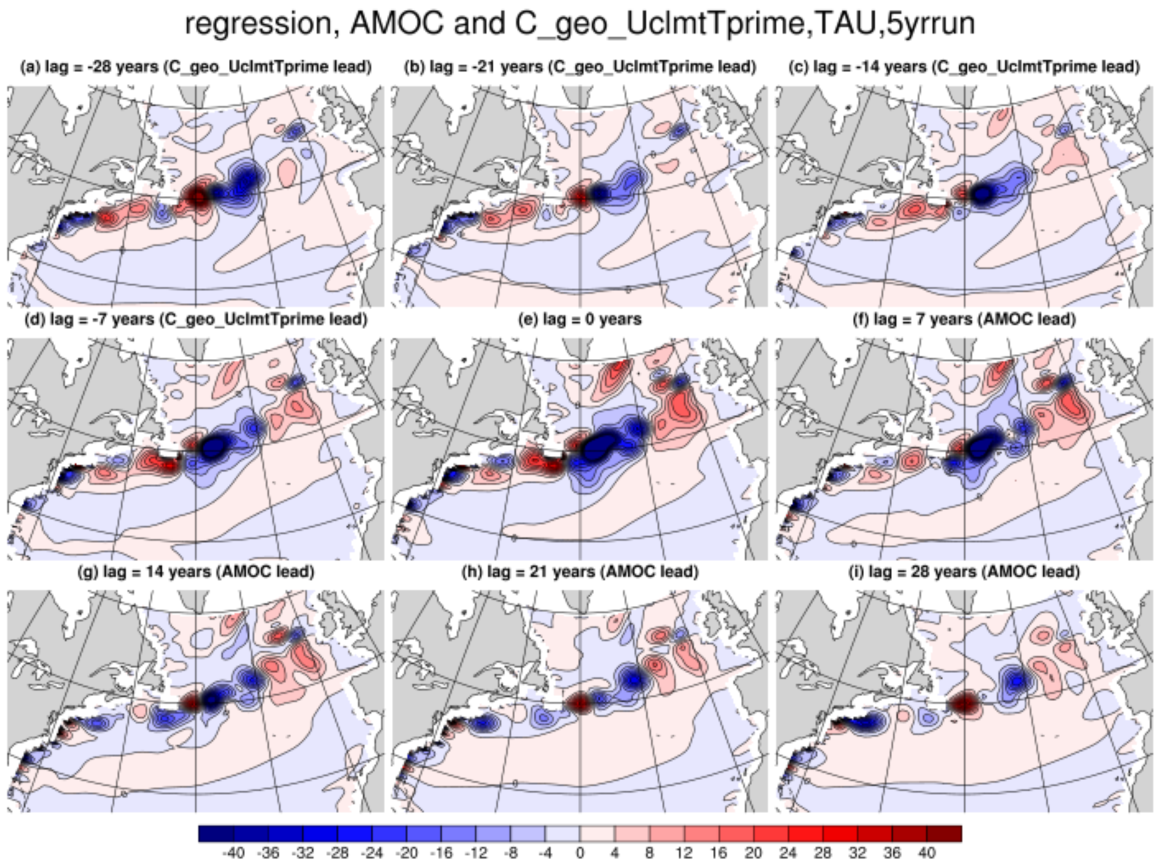

Figure 5.20: Same as Fig. 5.19, but for $C_{geo}(\overline{\vec{u}}_{geo}, T')$.

Ekman current or indirectly by other processes.

To investigate how wind stress impacts the ocean, we need to know how wind stress varies. The wind stress variance shows the maximum patterns for both TAUX and TAUY are located in the subpolar gyre region. The amplitude of TAUX variance is larger than TAUY. We also find that our model wind stress pattern is different from the CORE2 (Coordinated ocean-ice reference experiments, phase 2) wind stress pattern, for both locations

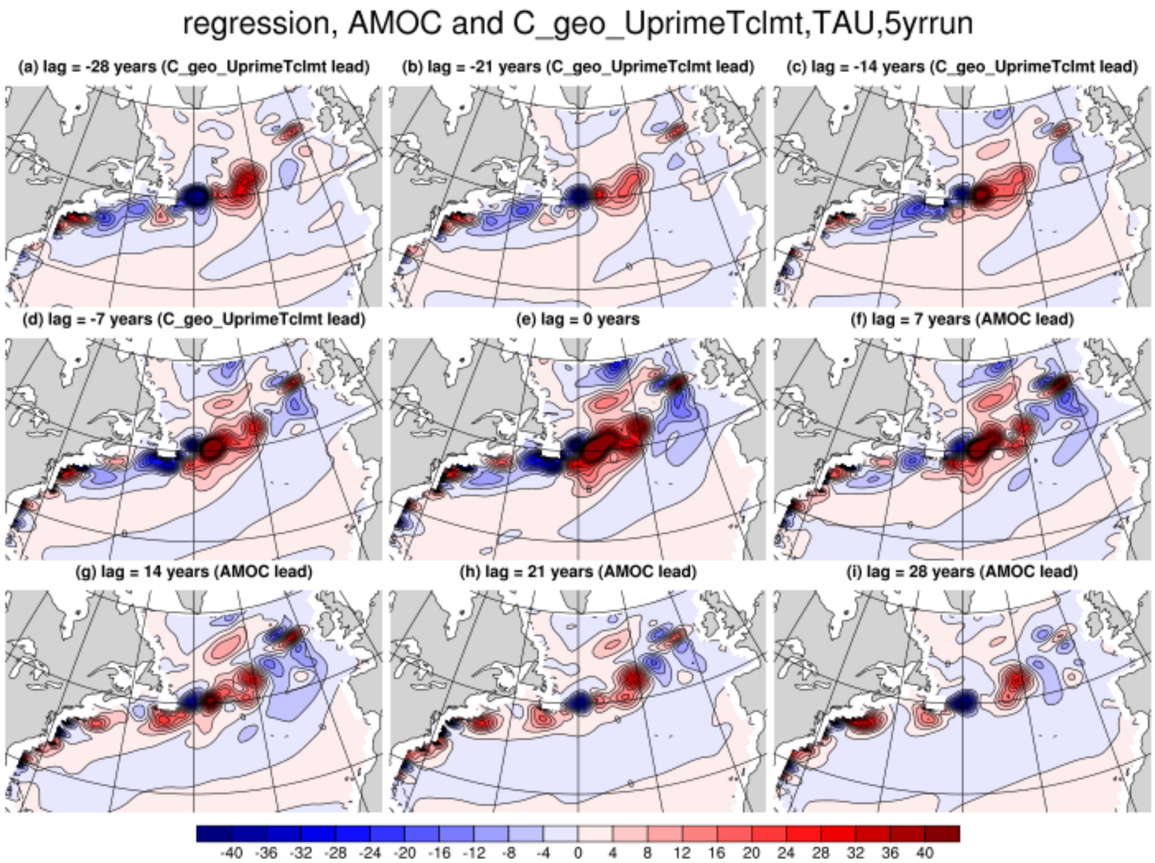

Figure 5.21: Same as Fig. 5.19, but for $C_{geo}(\vec{u}'_{geo}, \overline{T})$.

and amplitude. Our TAUX variance is located only in the subpolar gyre region, whereas the CORE2 TAUX variance is in both the subpolar and subtropical region. Our TAUY varies mainly in the subpolar gyre area, while the CORE2 TAUY variance is in the southeast region. Our TAUX has the maximum variance about 0.016, larger than the maximum variance of TAUX in CORE2 (0.006).

In the TAU run, advection is the only term that important for generating the HC anomalies, as SHF only damps the heat. The advection regression pattern shows that at lag 0 there is negative advection in the transition zone (TZ) and positive advection in the GS extension region and the subpolar gyre area. This total advection variation pattern in the GS extension region is dominated by the velocity fluctuation superimposed on the climatological temperature fields, while the total advection variation in the subpolar gyre region is determined by the mean flow transporting the temperature anomalies.

One possible physical process through which the surface wind stress affects the advection is investigated. An anti-cyclonic wind stress, or a negative wind stress curl, appears in the subpolar gyre region, not only generating positive HC anomalies underneath it, but also leading to downwelling through Ekman pumping. This downwelling is primarily located in the mid-east region and squeezes the subpolar gyre to the west, as a result of which the Labrador current and the northeastward current anomaly around latitude 45°N are strengthened. The strengthened currents lead to $C_{adv}(\vec{u}', \overline{T})$ pattern, then determine the total advection and impact the HC. However, this process needs further investigation.

At last, the total advection is decomposed into the geostrophic advection and the Ekman advection. We find that the total advection is dominated by the geostrophic advection, but not the Ekman advection, although Ekman advection does make some contributions on the total advection, but negligible. This demonstrates that the SMF impacts the AMV indirectly by generating the geostrophic current. The geostrophic advection and the Ekman advection are further decomposed into two parts, the velocity fluctuation superimposed on the climatological temperature field and the temperature fluctuation superimposed on the climatological velocity field, respectively. We find that the velocity fluctuation and the temperature fluctuation generate opposite advection and the effect of them is opposite for both geostrophic and Ekman advection. The geostrophic advection caused by the perturbed $\vec{u}_{geo}$ superimposed on the climatological temperature field ($C_{geo}(\vec{u}'_{geo}, \overline{T})$) determines the C_{geo} term in the GS extension region, and $C_{geo}(\overline{\vec{u}}_{geo}, T')$ determines the total geostrophic advection in the norther Atlantic Ocean. $C_{ek}(\vec{u}'_{ek}, \overline{T})$ dominates most of the C_{ek} fluctuations.

Chapter 6: Summary

The Atlantic multidecadal variability (AMV) has major impacts on the regional and global climate and understanding its mechanisms can help us understand and predict the long-term climate variability. In this study, we focus on the oceanic processes in response to surface forcings to generate the multidecadal variability of both the upper and deep oceans, as well as their connections. The upper ocean heat content (HC) and Atlantic meridional overturning circulation (AMOC) are chosen as two basic variables to represent the upper and deep ocean circulations, respectively. The purposes of this study are the following: (1) we reexamine the relative roles of surface heat flux (SHF) and surface momentum flux (SMF) on causing AMOC multidecadal variability as proposed in previous studies based on multi-century simulations using a state-of-the-art modeling system and under interannually changing surface forcing fields exclusively due to natural climate variability; (2) we identify the different features of the upper ocean HC anomalies on multidecadal time scales, generated by the anomalous SHF and SMF forcings; (3) we examine whether their HC differences contribute to their AMOC differences, and the impact of the upper ocean dynamics and the mean state of the North Atlantic Ocean in producing the characteristic patterns of the upper ocean HC anomalies that connect with the fluctuations of the AMOC on multidecadal time scales.

To achieve these goals, we conduct and analyze a series of simulations using an ocean general circulation model (OGCM) forced by prescribed 600-year monthly atmospheric state variables from a multi-century preindustrial simulation of the Community Earth System Model Version 1.1.1 (CESM1.1.1) pre-industrial run (i.e., the CPLD simulation). The OGCM approach allows us to conduct sensitivity experiments, which decompose the oceanic response into the components associated with the SHF and SMF components after demonstrating that the OGCM under full surface forcing (i.e., CNTL simulation) can reproduce the major multidecadal variability of both AMOC and HC in the CPLD simulation, i.e., the oceanic processes associated with the multidecadal variability can be treated as a question of the oceanic responses to the interannually changing surface forcing fields. Once we confirm that uncoupled model simulation (CNTL) can reproduce the coupled model simulation (CPLD), we isolate the impacts of SHF and SMF in different sensitivity experiments. In the HEAT run, we turn off the interannually changing SMF by prescribing the monthly climatology surface momentum flux. In the TAU run, we turn off the interannually changing SHF by prescribing the monthly climatology surface heat flux. The comparison between different sensitivity experiments (CNTL, HEAT and TAU) can decompose oceanic responses to different forcings and give us more insight on the ocean dynamics. Each experiment has 600 model years and the same initial conditions. Our main conclusions are summarized as follows.

To begin with, we want to know the fully coupled model simulation can reproduce the observation so that the conclusion drawn from the experiments are applicable to explain the real world. We confirm that the fully coupled CESM pre-industrial run (CPLD) can simulate the observed climatological SST qualitatively, though with some bias. The observational SST is overestimated by the CPLD run along the western coast and underestimated in the GS extension region and the subtropical region, which might due to this is a non-eddy-resolving model.

We also demonstrate that the uncoupled model (CNTL) can reproduce the ocean climatology and multidecadal variability in the fully coupled model (CPLD). The comparison of the climatology and variability of AMOC, SST, HC, barotropic stream function (BSF), SHF among different experiments shows that those variables in CNTL run are very close to the CPLD run qualitatively. We also find that replacing some of the surface forcing fields from real-time monthly values with their monthly climatological values generate further mean state differences with CNTL. Between HEAT and TAU runs the former is more similar to CNTL in a great degree. Although the climatological patterns of those variables in TAU show larger quantitative bias to CNTL, these fields are still similar to each other qualitatively.

Similar to the previous studies, we find that most of the HC and AMOC multidecadal variability in CNTL is driven by SHF. However, different from DG00 and YD14, we find that SMF can also drive part of the multidecadal variability in the Atlantic Ocean, although it is less significant than SHF. The correlation coefficient of AMOC index between CNTL and CPLD is 0.73, between CNTL and HEAT is 0.82, and between CNTL and TAU is 0.27 (higher than the 5% significant level).

For the AMV index, mean SST between 10°N to 60°N in Atlantic Ocean, the variation and amplitude in CPLD, CNTL and HEAT are very similar, whereas the amplitude of AMV in TAU is very small, as a result of prescribed monthly climatology atmospheric state variables in TAU run. The HC index (mean HC between 10°N to 60°N in Atlantic Ocean) variation among different experiments are similar to the AMV index. However, HC index has a smaller amplitude and is smoother than AMV index, except for TAU. In TAU, HC index has the same amplitude as AMV, sometimes even larger, because the SST in TAU is strongly impacted by the prescribed monthly climatological SHF so the variance of SST in TAU is small while HC is more affected by the ocean dynamics.

Our results further show that SHF and SMF generate very different spatial distributions of the HC variability, which may provide further insight into the differences between their influences on the AMOC fluctuations. Although SMF is not as significant as SHF in driving AMOC variations, it can generate significant regional HC multidecadal variability in GS extension region. The point-to-point HC correlation between CNTL and TAU is higher in GS region than in other regions. On the other hand, SHF plays an essential role in driving HC variation in the northern North Atlantic Ocean, such as the subpolar gyre. In fact, the HC variance in HEAT is very similar to that in CNTL almost everywhere else. The HC anomalies in the HEAT and TAU runs are not significant correlated, which may indicate that the impacts of SMF and SHF on multidecadal variability in Atlantic are independent of each other. The HC spatial variance shows that the maximum variance is located in the GS region for all the experiments. However, HC variance in the subpolar gyre region is also large for CPLD, CNTL and HEAT, but smaller for TAU. The comparison of HC variance further demonstrates that SHF plays a key role in the HC variance, whereas the impact of SMF is more significant for the HC variance in the GS region than in the northeast area.

The EOF analysis demonstrates that most of the HC variance in the North Atlantic basin can be accounted for by the two leading modes, one is characterized by an action center in the GS region (EOF1) and the other is centered in the northeastern part of the North Atlantic on the track of the North Atlantic Current (EOF2). The sum of EOF1 and EOF2 explains more than half of the total HC variance. The variances of the first two EOF modes are highly correlated with the local mean HC variance. The correlation coefficients between PC1 and HCgulf index (mean HC in the GS extension region), and PC2 and HCnorth index (mean HC over the northeast Atlantic Ocean) are high for all the runs. This further demonstrates that the physical meaning of EOF1 and EOF2 is the regional HC variance. EOF1 and EOF2 also present different phases along the HC anomalies propagation trajectory, as PC1 leads PC2 for four years. The PC1 (as well as PC2) correlation between HEAT and TAU is not significant, which indicates that SHF and SMF may have independent impacts on HC variability.

The previous conclusion that SMF can drive HC variance on multidecadal scale in the GS region is further demonstrated by the comparison of local HC indices. The HCgulf index in TAU has a similar amplitude as CNTL and HEAT. HCnorth in TAU also shows multidecadal variability, but the amplitude is weaker than HEAT and CNTL. The correlations of HCgulf and HCnorth between CNTL and TAU are also significant (0.56). Both the HCnorth and HCgulf in HEAT are significantly correlated with that in CNTL, which also proves that SHF has major impacts on local HC variability.

The lead-lag correlations between HC field and AMOC index show that when the HC shows a dipole pattern in the North Atlantic, i.e., negative anomalies in the Gulf Stream (GS) extension region and positive anomalies in the northeast of the basin, the upper branch of AMOC also gets strengthened, which is in agreement with the thermal wind theory. The Gulf Stream part of HC dipole pattern overlaps EOF1 mode (or HCgulf) and the northeast Atlantic part of the HC dipole pattern overlaps the EOF2 mode (or HCnorth). As a result, the HC variations in these two regions are connected with the fluctuations of AMOC. SHF can generate strong HC variance in both regions, so the AMOC in SHF is also stronger. SMF can only generate strong HC variance in the Gulf Stream region. In TAU, the HC variance in the northeast of the basin is weaker, shown by weaker EOF2 and weaker HCnorth amplitude. As a result, the AMOC in TAU is also weaker.

The heat budget analysis of HC gives us more insight on the physical processes of how the characteristic patterns of HC anomalies are generated. We find that, although the SHF and SMF play the ultimately important role in generating the HC anomalies in the North Atlantic basin, the ocean dynamics plays a major role in redistributing and enhancing the HC anomalies in the two action centers described above. We find that when ocean is driven by SHF (HEAT run) the advection term determines the tendency in the GS region and the northeastern North Atlantic. On multidecadal time scales, after the HC anomalies get strengthened in the northeastern North Atlantic through advection, the local SHF starts to damp these existing HC anomalies.

The combined first EOFs of H_t, C_{adv} and Q_{net} show strong tendency in the North Atlantic and weak and opposite tendency in the GS extension region. These two regions overlap the strong HC variance region. The advection dominates the tendency and generate HC anomalies in these two regions (one in the GS extension and one in the north). Part of the HC in the GS extension region generated by the strong advection is weakened by the local SHF in the same region. For the combined EOF2, the pattern is very similar to EOF1 but offset to the northeastern North Atlantic. The relative roles of advection and heat flux is also similar to EOF1. In the subpolar gyre region the damping effect of SHF in HEAT is similar to CNTL but weaker than TAU. This explains why in the CNTL and HEAT runs HC variance is also larger in the sub-polar region, as the weak damping effect in that region allows the accumulation of HC. One should also note that the relative roles played by the advection and local SHF for the HC tendency in these regions depends on the time scale of the variability. Note that for short-term variability with periods less than 5 years, local SHF is a driving element same as the advection.

We have further analyzed the different physical processes that generate the heat advection. In general, the advection fluctuation is mainly determined by the perturbation of the ocean current field superimposed on the climatological temperature field in the GS extension region, and by the fluctuation of the temperature anomalies in the northeastern Atlantic. The total advection is dominated by the geostrophic advection, but not the Ekman advection, although Ekman advection does make some contributions to the total advection. In particular, SMF anomalies in the TAU run seem to drive the HC variability by generating geostrophic current, instead of directly through the anomalous Ekman current. By further decomposing, we find that the geostrophic advection fluctuation is driven by the geostrophic current fluctuation.

In this study, there are still some unsolved questions. For example, we already know that ocean dynamics plays a key role in the HC strengthening process in the GS extension region and the northeastern Atlantic Ocean. The question is how the surface forcings generate the advection in those regions on multidecadal time scales? Where is the key region where SHF anomalies play a major role in generating the HC anomalies? Where is the critical region of SMF in generating the HC anomalies? How does parameterization in the bulk formula affect the surface fluxes? We will try to answer these questions in the further studies.

Bibliography

Biastoch, A., C. W. Böning, J. Getzlaff, J.-M. Molines, and G. Madec, 2008: Causes of interannual–decadal variability in the meridional overturning circulation of the midlatitude North Atlantic Ocean. *Journal of Climate*, **21 (24)**, 6599–6615.

Bryden, H., A. Mujahid, S. Cunningham, and T. Kanzow, 2009: Adjustment of the basin-scale circulation at 26 degrees N to variations in Gulf Stream, deep western boundary current and Ekman transports as observed by the rapid array. *Ocean Science*, **5 (4)**, 421–433.

Buckley, M. W., D. Ferreira, J.-M. Campin, J. Marshall, and R. Tulloch, 2012: On the relationship between decadal buoyancy anomalies and variability of the Atlantic meridional overturning circulation. *Journal of Climate*, **25 (23)**, 8009–8030.

Buckley, M. W., and J. Marshall, 2016: Observations, inferences, and mechanisms of the Atlantic Meridional Overturning Circulation: A review. *Reviews of Geophysics*, **54 (1)**, 5–63.

Buckley, M. W., R. M. Ponte, G. Forget, and P. Heimbach, 2014: Low-frequency SST and upper-ocean heat content variability in the North Atlantic. *Journal of Climate*, **27 (13)**, 4996–5018.

Buckley, M. W., R. M. Ponte, G. Forget, and P. Heimbach, 2015: Determining the origins of advective heat transport convergence variability in the North Atlantic. *Journal of Climate*, **28 (10)**, 3943–3956.

Chen, F., and M. Ghil, 1995: Interdecadal variability of the thermohaline circulation and high-latitude surface fluxes. *Journal of Physical Oceanography*, **25 (11)**, 2547–2568.

Chen, H., E. K. Schneider, and Z. Wu, 2016: Mechanisms of internally generated decadal-to-multidecadal variability of SST in the Atlantic Ocean in a coupled GCM. *Climate Dynamics*, **46 (5-6)**, 1517–1546.

Danabasoglu, G., S. C. Bates, B. P. Briegleb, S. R. Jayne, M. Jochum, W. G. Large, S. Peacock, and S. G. Yeager, 2012: The CCSM4 ocean component. *Journal of Climate*, **25 (5)**, 1361–1389.

Danabasoglu, G., R. Ferrari, and J. C. McWilliams, 2008: Sensitivity of an ocean general circulation model to a parameterization of near-surface eddy fluxes. *Journal of Climate*, **21 (6)**, 1192–1208.

Danabasoglu, G., W. G. Large, and B. P. Briegleb, 2010: Climate impacts of parameterized Nordic Sea overflows. *Journal of Geophysical Research: Oceans*, **115 (C11)**.

Delworth, T., S. Manabe, and R. Stouffer, 1993: Interdecadal variations of the thermohaline circulation in a coupled ocean-atmosphere model. *Journal of Climate*, **6 (11)**, 1993–2011.

Delworth, T. L., and R. J. Greatbatch, 2000: Multidecadal thermohaline circulation variability driven by atmospheric surface flux forcing. *Journal of Climate*, **13 (9)**, 1481–1495.

Delworth, T. L., and M. E. Mann, 2000: Observed and simulated multidecadal variability in the Northern Hemisphere. *Climate Dynamics*, **16 (9)**, 661–676.

Deshayes, J., R. Curry, and R. Msadek, 2014: CMIP5 model intercomparison of freshwater budget and circulation in the North Atlantic. *Journal of Climate*, **27 (9)**, 3298–3317.

Dima, M., and G. Lohmann, 2007: A hemispheric mechanism for the Atlantic multidecadal oscillation. *Journal of Climate*, **20 (11)**, 2706–2719.

Dong, B.-W., and R. Sutton, 2001: The dominant mechanisms of variability in Atlantic ocean heat transport in a coupled ocean-atmosphere GCM. *Geophysical Research Letters*, **28 (12)**, 2445–2448.

Dong, S., S. L. Hautala, and K. A. Kelly, 2007: Interannual variations in upper-ocean heat content and heat transport convergence in the western North Atlantic. *Journal of Physical Oceanography*, **37 (11)**, 2682–2697.

Dong, S., and K. A. Kelly, 2004: Heat budget in the Gulf Stream region: The importance of heat storage and advection. *Journal of Physical Oceanography*, **34 (5)**, 1214–1231.

Drews, A., and R. J. Greatbatch, 2016: Atlantic multidecadal variability in a model with an improved North Atlantic Current. *Geophysical Research Letters*, **43 (15)**, 8199–8206.

Feng, S., and Q. Hu, 2008: How the North Atlantic Multidecadal Oscillation may have influenced the Indian summer monsoon during the past two millennia. *Geophysical Research Letters*, **35 (1)**.

Frankcombe, L., and H. Dijkstra, 2009: Coherent multidecadal variability in North Atlantic sea level. *Geophysical Research Letters*, **36 (15)**.

Frankcombe, L. M., A. Von Der Heydt, and H. A. Dijkstra, 2010: North Atlantic multidecadal climate variability: an investigation of dominant time scales and processes. *Journal of climate*, **23 (13)**, 3626–3638.

Frankignoul, C., P. Müller, and E. Zorita, 1997: A simple model of the decadal response of the ocean to stochastic wind forcing. *Journal of Physical Oceanography*, **27 (8)**, 1533–1546.

Gent, P. R., and J. C. Mcwilliams, 1990: Isopycnal mixing in ocean circulation models. *Journal of Physical Oceanography*, **20 (1)**, 150–155.

Gent, P. R., and Coauthors, 2011: The community climate system model version 4. *Journal of Climate*, **24 (19)**, 4973–4991.

Ghil, M., and R. Vautard, 1991: Interdecadal oscillations and the warming trend in global temperature time series. *Nature*, **350 (6316)**, 324–327.

Greatbatch, R. J., and S. Zhang, 1995: An interdecadal oscillation in an idealized ocean basin forced by constant heat flux. *Journal of Climate*, **8 (1)**, 81–91.

Griffies, S. M., and E. Tziperman, 1995: A linear thermohaline oscillator driven by stochastic atmospheric forcing. *Journal of Climate*, **8 (10)**, 2440–2453.

Grist, J. P., and Coauthors, 2010: The roles of surface heat flux and ocean heat transport convergence in determining Atlantic Ocean temperature variability. *Ocean Dynamics*, **60 (4)**, 771–790.

Hibler, W. D., and S. J. Johnsen, 1979: The 20-yr cycle in Greenland ice core records. *Nature*, **280 (5722)**, 481–483.

Holland, M. M., D. A. Bailey, B. P. Briegleb, B. Light, and E. Hunke, 2012: Improved sea ice shortwave radiation physics in CCSM4: The impact of melt ponds and aerosols on Arctic sea ice. *Journal of Climate*, **25 (5)**, 1413–1430.

Hunke, E., W. Lipscomb, A. Turner, N. Jeffery, and S. Elliott, 2008: CICE: the Los Alamos sea ice model, documentation and software, version 4.0. Los Alamos National Laboratory Tech. Rep. Tech. rep., LA-CC-06-012.

Kim, W. M., S. Yeager, P. Chang, and G. Danabasoglu, 2018: Low-frequency North Atlantic climate variability in the community earth system model large ensemble. *Journal of Climate*, **31 (2)**, 787–813.

Kirtman, B. P., E. K. Schneider, D. M. Straus, D. Min, and R. Burgman, 2011: How weather impacts the forced climate response. *Climate Dynamics*, **37 (11-12)**, 2389–2416.

Kirtman, B. P., and J. Shukla, 2002: Interactive coupled ensemble: A new coupling strategy for CGCMs. *Geophysical Research Letters*, **29 (10)**.

Kirtman, B. P., D. M. Straus, D. Min, E. K. Schneider, and L. Siqueira, 2009: Toward linking weather and climate in the interactive ensemble NCAR climate model. *Geophysical Research Letters*, **36 (13)**.

Klinger, B. A., and C. Cruz, 2009: Decadal response of global circulation to Southern Ocean zonal wind stress perturbation. *Journal of Physical Oceanography*, **39 (8)**, 1888–1904.

Knight, J. R., R. J. Allan, C. K. Folland, M. Vellinga, and M. E. Mann, 2005: A signature of persistent natural thermohaline circulation cycles in observed climate. *Geophysical Research Letters*, **32 (20)**.

Knight, J. R., C. K. Folland, and A. A. Scaife, 2006: Climate impacts of the Atlantic multidecadal oscillation. *Geophysical Research Letters*, **33 (17)**.

Kuhlbrodt, T., A. Griesel, M. Montoya, A. Levermann, M. Hofmann, and S. Rahmstorf, 2007: On the driving processes of the Atlantic meridional overturning circulation. *Reviews of Geophysics*, **45 (2)**.

Kushnir, Y., 1994: Interdecadal variations in North Atlantic sea surface temperature and associated atmospheric conditions. *Journal of Climate*, **7 (1)**, 141–157.

Kwon, Y.-O., and C. Frankignoul, 2012: Stochastically-driven multidecadal variability of the Atlantic meridional overturning circulation in CCSM3. *Climate Dynamics*, **38 (5-6)**, 859–876.

Large, W., and S. Pond, 1981: Open ocean momentum flux measurements in moderate to strong winds. *Journal of Physical Oceanography*, **11 (3)**, 324–336.

Large, W., and S. Pond, 1982: Sensible and latent heat flux measurements over the ocean. *Journal of Physical Oceanography*, **12 (5)**, 464–482.

Large, W. G., J. C. McWilliams, and S. C. Doney, 1994: Oceanic vertical mixing: A review and a model with a nonlocal boundary layer parameterization. *Reviews of Geophysics*, **32 (4)**, 363–403.

Lee, S.-K., W. Park, E. Van Sebille, M. O. Baringer, C. Wang, D. B. Enfield, S. G. Yeager, and B. P. Kirtman, 2011: What caused the significant increase in Atlantic Ocean heat content since the mid-20th century? *Geophysical Research Letters*, **38 (17)**.

Leonard, B. P., 1979: A stable and accurate convective modelling procedure based on quadratic upstream interpolation. *Computer Methods in Applied Mechanics and Engineering*, **19 (1)**, 59–98.

Liu, Z., 2012: Dynamics of interdecadal climate variability: A historical perspective. *Journal of Climate*, **25 (6)**, 1963–1995.

Marshall, J., and Coauthors, 2001: North Atlantic climate variability: phenomena, impacts and mechanisms. *International Journal of Climatology*, **21 (15)**, 1863–1898.

Roemmich, D., and C. Wunsch, 1984: Apparent changes in the climatic state of the deep North Atlantic Ocean. *Nature*, **307 (5950)**, 447–450.

Saenko, O. A., and A. J. Weaver, 2004: What drives heat transport in the Atlantic: Sensitivity to mechanical energy supply and buoyancy forcing in the Southern Ocean. *Geophysical Research Letters*, **31 (20)**.

Sato, O. T., and T. Rossby, 2000: Seasonal and low-frequency variability of the meridional heat flux at 36N in the North Atlantic. *Journal of Physical Oceanography*, **30 (3)**, 606–621.

Schneider, E. K., and M. Fan, 2007: Weather noise forcing of surface climate variability. *Journal of the Atmospheric Sciences*, **64 (9)**, 3265–3280.

Smeed, D., G. McCarthy, D. Rayner, B. Moat, W. Johns, M. Baringer, and C. Meinen, 2016: Atlantic meridional overturning circulation observed by the RAPID-MOCHA-WBTS (RAPID-Meridional Overturning Circulation and Heatflux Array-Western Boundary Time Series) array at 26N from 2004 to 2015.

Smeed, D., and Coauthors, 2018: The North Atlantic Ocean is in a state of reduced overturning. *Geophysical Research Letters*, **45 (3)**, 1527–1533.

Smith, D. M., R. Eade, N. J. Dunstone, D. Fereday, J. M. Murphy, H. Pohlmann, and A. A. Scaife, 2010a: Skilful multi-year predictions of Atlantic hurricane frequency. *Nature geoscience*, **3 (12)**, 846.

Smith, R., and Coauthors, 2010b: The Parallel Ocean Program (POP) reference manual: Ocean component of the community climate system model (CCSM) and Community Earth System Model (CESM). *Rep. LAUR-10-01853*, **141**, 1–140.

Sutton, R. T., and D. L. Hodson, 2005: Atlantic Ocean forcing of North American and European summer climate. *Science*, **309 (5731)**, 115–118.

Te Raa, L. A., and H. A. Dijkstra, 2002: Instability of the thermohaline ocean circulation on interdecadal timescales. *Journal of Physical Oceanography*, **32 (1)**, 138–160.

Te Raa, L. A., and H. A. Dijkstra, 2003: Sensitivity of North Atlantic multidecadal variability to freshwater flux forcing. *Journal of Climate*, **16 (15)**, 2586–2601.

Thornalley, D. J., and Coauthors, 2018: Anomalously weak Labrador Sea convection and atlantic overturning during the past 150 years. *Nature*, **556 (7700)**, 227.

Timmermann, A., and H. Goosse, 2004: Is the wind stress forcing essential for the meridional overturning circulation? *Geophysical Research Letters*, **31 (4)**.

Toggweiler, J., and B. Samuels, 1995: Effect of Drake Passage on the global thermohaline circulation. *Deep Sea Research Part I: Oceanographic Research Papers*, **42 (4)**, 477–500.

Trenary, L., and T. DelSole, 2016: Does the Atlantic multidecadal oscillation get its predictability from the atlantic meridional overturning circulation? *Journal of Climate*, **29 (14)**, 5267–5280.

Trenberth, K. E., and D. J. Shea, 2006: Atlantic hurricanes and natural variability in 2005. *Geophysical Research Letters*, **33 (12)**.

Tulloch, R., and J. Marshall, 2012: Exploring mechanisms of variability and predictability of Atlantic meridional overturning circulation in two coupled climate models. *Journal of Climate*, **25 (12)**, 4067–4080.

Tziperman, E., 2000: Proximity of the present-day thermohaline circulation to an instability threshold. *Journal of Physical Oceanography*, **30 (1)**, 90–104.

Wang, C., and L. Zhang, 2013: Multidecadal ocean temperature and salinity variability in the tropical North Atlantic: Linking with the AMO, AMOC, and subtropical cell. *Journal of Climate*, **26 (16)**, 6137–6162.

Weaver, A. J., J. Marotzke, P. F. Cummins, and E. Sarachik, 1993: Stability and variability of the thermohaline circulation. *Journal of Physical Oceanography*, **23 (1)**, 39–60.

Weaver, A. J., and E. Sarachik, 1991a: Evidence for decadal variability in an ocean general circulation model: An advective mechanism. *Atmosphere-Ocean*, **29 (2)**, 197–231.

Weaver, A. J., and E. Sarachik, 1991b: The role of mixed boundary conditions in numerical models of the ocean's climate. *Journal of Physical Oceanography*, **21 (9)**, 1470–1493.

Xu, X., E. P. Chassignet, W. E. Johns, W. J. Schmitz, and E. J. Metzger, 2014: Intraseasonal to interannual variability of the Atlantic meridional overturning circulation from eddy-resolving simulations and observations. *Journal of Geophysical Research: Oceans*, **119 (8)**, 5140–5159.

Yeager, S., and G. Danabasoglu, 2014: The origins of late-twentieth-century variations in the large-scale North Atlantic circulation. *Journal of Climate*, **27 (9)**, 3222–3247.

Zhai, X., and L. Sheldon, 2012: On the North Atlantic ocean heat content change between 1955–70 and 1980–95. *Journal of Climate*, **25 (10)**, 3619–3628.

Zhang, J., and R. Zhang, 2015: On the evolution of Atlantic meridional overturning circulation fingerprint and implications for decadal predictability in the North Atlantic. *Geophysical Research Letters*, **42 (13)**, 5419–5426.

Zhang, R., and T. L. Delworth, 2006: Impact of Atlantic multidecadal oscillations on India/Sahel rainfall and Atlantic hurricanes. *Geophysical Research Letters*, **33 (17)**.

Zhang, R., R. Sutton, G. Danabasoglu, T. L. Delworth, W. M. Kim, J. Robson, and S. G. Yeager, 2016: Comment on "The Atlantic Multidecadal Oscillation without a role for ocean circulation". *Science*, **352 (6293)**, 1527–1527.

Curriculum Vitae

Liang Yu was born in Liaoning, China. He graduated from Nanjing University in 2010 with a Bachelor of Science majoring in Atmospheric Science. He received his Master degree in 2013 from Institute Oceanology, Chinese Academy of Sciences. In fall of 2013, he came to George Mason University to pursue a Ph.D. degree in Climate Dynamics with guidance of Prof. Bohua Huang.